

**SIGNAL PROCESSING FOR
ULTRA-WIDEBAND WIRELESS
COMMUNICATIONS**

Ph.D. Thesis

by

SANJEEV SHARMA



**DISCIPLINE OF ELECTRICAL ENGINEERING
INDIAN INSTITUTE OF TECHNOLOGY
INDORE
JULY, 2018**

**SIGNAL PROCESSING FOR
ULTRA-WIDEBAND WIRELESS
COMMUNICATIONS**

A THESIS

*Submitted in partial fulfillment of the
requirements for the award of the degree*

of

DOCTOR OF PHILOSOPHY

by

SANJEEV SHARMA



**DISCIPLINE OF ELECTRICAL ENGINEERING
INDIAN INSTITUTE OF TECHNOLOGY
INDORE
JULY, 2018**



INDIAN INSTITUTE OF TECHNOLOGY INDORE

CANDIDATE'S DECLARATION

I hereby certify that the work which is being presented in the thesis entitled “**SIGNAL PROCESSING FOR ULTRA-WIDEBAND WIRELESS COMMUNICATIONS**” in the partial fulfillment of the requirements for the award of the degree of DOCTOR OF PHILOSOPHY and submitted in the DISCIPLINE OF ELECTRICAL ENGINEERING, Indian Institute of Technology Indore, is an authentic record of my own work carried out during the time period from June 2015 to July 2018 under the supervision of Dr. Vimal Bhatia, Professor, Indian Institute of Technology Indore, India and Dr. Anubha Gupta, Associate Professor, Indraprastha Institute of Information Technology Delhi, India.

The matter presented in this thesis has not been submitted by me for the award of any other degree of this or any other institute.

Signature of the student with date
(SANJEEV SHARMA)

This is to certify that the above statement made by the candidate is correct to the best of my knowledge.

Signature of Thesis Supervisor-1 with date
(Dr. VIMAL BHATIA)

Signature of Thesis Supervisor-2 with date
(Dr. ANUBHA GUPTA)

Sanjeev Sharma has successfully given his Ph.D. Oral Examination held on

Signature of Chairperson (OEB)
Date:

Signature of External Examiner
Date:

Signature of Thesis Supervisor-1
Date:

Signature of Thesis Supervisor-2
Date:

Convener, DPGC
Date:

Signature of PSPC Member-1
Date:

Signature of PSPC Member-2
Date:

Signature of Head of Discipline
Date:

ACKNOWLEDGEMENTS

First and foremost, I express my heartfelt and profound gratitude to my Ph.D. supervisors Dr. Vimal Bhatia and Dr. Anubha Gupta for their invaluable guidance, encouragement, direction throughout my thesis work and specially for their calm nature. It is my great honor and pleasure to work under the esteemed guidance of kind and responsible supervisors Dr. Vimal Bhatia and Dr. Anubha Gupta. I am thankful for all the freedom they gave me to explore various research topics and always available for discussion despite their busy schedule. I would also like to thank my PG Student's Progress Committee (PSPC) committee members Dr. Abhinav Kranti and Dr. Gourinath Banda for their fruitful discussions and suggestions towards my research.

I am truly thankful to all the faculty and staff of Indian Institute of Technology Indore for their invaluable cooperation throughout my thesis work. I would also like to thank all the members in Signal and Software group (SaSg) for their encouragement and support that helped me to face the hard phase of my life and never letting me feel lonely along this long journey. Specifically, I would like to extend my appreciation to my friends Mohit Sharma, Kuntal Deka, Dharmendra Dixit, Abhijeet Bishnu, Praveen Kumar Singya, Nagendra Kumar, Rangeet Mitra and my colleagues who helped me in several ways during my thesis work.

I would thank Visvesvaraya PhD scheme of Ministry of Electronics and Information Technology, Government of India and IIT Indore for providing financial assistance. I would also take this opportunity to thank Visvesvaraya PhD scheme for funding my conference travels. These conferences helped me meet new people and experts who have helped shape my PhD thesis.

Finally, I would like to thank my family for their love and encouragement.

SANJEEV SHARMA

Dedicated to my family

ABSTRACT

Unlicensed ultra-wideband (UWB) technology has received significant research interest for communication, localization and mapping due to its large bandwidth, low power and low complexity. Therefore, UWB technology can be considered for short range based applications for next generation wireless networks especially in internet of things and wireless sensor networks. One of the main challenges it faces is the interference from impulsive noise and narrowband communications, since it has low power and huge bandwidth. Further, the Nyquist sampling rate of the UWB signals is very high, which results in costly and complex system design for practical applications.

In this thesis, the impact of impulsive noise in UWB wireless communication channels and a novel robust UWB receiver design is investigated that utilizes the received UWB signal cluster sparsity characteristics to mitigate impulsive noise. Further, multiple UWB signal clusters (due to hundreds of multipath) work as a diversity scheme in the proposed receiver design to reduce UWB signal blanking in the presence of impulsive noise.

Then the effect of narrowband interferences (NBIs) on the UWB system is considered, since wideband width UWB signals overlap with high power narrowband wireless communication devices. The sparsity-based NBI mitigation method is proposed that exploits distinct characteristics of UWB signals and NBI. The proposed NBI mitigation method does not require a non-linear operator such as a limiter or a blanker. Improved performance of the proposed UWB receiver has been validated UWB signal transmission in multipath fading channels.

A sub-Nyquist rate UWB receiver is designed by exploiting the sparsity of UWB signals to reduce the sampling rate and power consumption of a UWB system. A deterministic (partial) UWB waveform-matched measurement matrix is proposed. The proposed measurement matrix has circulant structure and is sparse in nature. The proposed matrix is easy to implement in hardware and is operationally time efficient as needed in a practical system. Further, bit error rate performance of the corresponding UWB system and the operational time complexity with the proposed measurement matrix are analyzed and compared to the existing measurement matrices for a sub-Nyquist rate receiver design.

Next, UWB system for wireless sensor network (WSN) using massive antenna arrays (MAAa) at fusion center (FC) for distributed detection is proposed and analyzed. The coherent and energy based fusion rules are analyzed for the proposed WSN over multiple access channels. The trade-off between performance and implementation complexity of the coherent and energy based fusion is studied. Further, it is shown that MAAs at FC and various level of channel knowledge can enhance the performance of energy-based detector in UWB sensor network with simple system implementation and signal processing requirement. Performance of the proposed UWB sensor network with reference to probability of detection, false alarm, and error are analyzed over standard IEEE 802.15.4a multipath channels and results are validated using simulations. The impact of various design parameters such as the number of sensors, receiver antennas, sensor quality, and integration interval on the

system performance is also analyzed.

Lastly, the impact of various system parameters on the performance metrics such as bit error rate, time of arrival is highlighted and demonstrated. Semi-analytical results are compared with Monte' Carlo simulations to verify the correctness of derived expressions for UWB systems.

The robust transmitter and receiver designs proposed in the thesis have been compared with the existing designs are proved to be better than the existing designs, techniques, and algorithms, both analytically and empirically.

Contents

ABSTRACT	i
LIST OF FIGURES	vii
LIST OF TABLES	x
LIST OF ABBREVIATIONS	xi
Notations and Symbols	xiii
1 Introduction	1
1.1 Overview	1
1.2 UWB technology	2
1.3 UWB signal propagation characteristics	3
1.4 UWB standardization	6
1.5 UWB applications	7
1.5.1 UWB in communication	7
1.5.2 UWB in ranging	8
1.5.3 UWB in medicine	8
1.6 Performance measures	9
1.7 UWB pulses	11
1.7.1 UWB pulse using POCS algorithm	12
1.8 Sparse signals	19
1.9 Motivation	20
1.10 Thesis outline and contributions	22
1.11 Organization of the thesis	23
2 Impulse Noise Mitigation in IR-UWB Communication using Signal Cluster Sparsity	25
2.1 Introduction	26
2.2 IN and its modeling	26
2.2.1 Bernoulli Gaussian IN	27
2.2.2 α -stable IN	27
2.3 System model	28
2.4 Proposed receiver design	29
2.4.1 Cluster detection algorithm	29
2.4.2 False alarm and miss-detection probabilities	31
2.4.3 BER performance	32
2.4.4 UWB signal and IN samples overlap	33

2.5	Simulation results and discussion	35
2.6	Summary	39
3	Sparsity-Based Narrowband Interference Mitigation in Ultra Wide-Band Communication for 5G and Beyond	41
3.1	Introduction	42
3.2	System model	44
3.3	Proposed NBI mitigation method using sparsity	47
3.4	Simulation and discussion	53
3.5	Summary	60
4	A New Sparse Signal-Matched Measurement Matrix for Compressive Sensing in UWB Communication	61
4.1	Introduction	62
4.2	UWB system model and receiver design in CS domain	66
4.2.1	UWB system model	66
4.2.2	Signal acquisition block	67
4.2.3	Sub-Nyquist rate CS domain UWB receiver design	69
4.3	Proposed measurement matrix	73
4.3.1	DCT matrix	77
4.3.2	Hadamard matrix	77
4.3.3	Gaussian matrix	78
4.4	Simulation results and discussion	78
4.4.1	Coherence and signal reconstruction error	79
4.4.2	BER performance of sub-Nyquist CS UWB receiver in multi-path channel	81
4.4.3	BER performance of signal domain based CS UWB receiver in frame repetition environment	82
4.5	Summary	89
5	IR-UWB Sensor Network using Massive MIMO Decision Fusion	91
5.1	Introduction	92
5.2	UWB-based WSN system model and general assumptions	95
5.2.1	Event-sensor link:sensing	96
5.2.2	Sensor-FC link:reporting	98
5.3	Decision fusion	100
5.3.1	Coherent detection	100
5.3.2	Non-coherent energy detector	105
5.4	ED performance enhancement using various side system information .	110
5.4.1	Amplitude envelope of CIR	110
5.4.2	Noise hardening	112
5.4.3	Sensor nodes' power optimization	113
5.5	Numerical results and discussion	114
5.5.1	Coherent detection at FC	115
5.5.2	Energy based detection	116
5.6	Summary	123

6 Conclusion and Future Work	125
6.1 Summary of contribution	125
6.2 Future work	126
REFERENCES	129
LIST OF PUBLICATIONS	143

List of Figures

1.1	UWB emission limits (in dBm) restricted by the FCC.	3
1.2	A pictorial view of the UWB channel model.	5
1.3	A graphical representation of UWB applications.	9
1.4	Flow chart of POCS algorithm for UWB pulse design.	18
1.5	PSD of Norman pulse $p_n(t)$, sixth derivative Gaussian pulse $g_6(t)$, Lee pulse $p_l(t)$ and POCS-based pulse $x(t)$ with FCC spectral mask.	19
1.6	An example of a sparse signal.	20
2.1	The received signal \mathbf{r} (at the top), blanking output signal \mathbf{y} and signal $\hat{\mathbf{s}}$ (at the bottom) after the proposed CDA.	37
2.2	Average BER vs. SNR performance of TH-BPSK system in the presence of IN at SIR = -30 dB in multipath IEEE 802.15.4a channel CM1 (left) and CM9 (right) channels.	38
2.3	Average BER vs. SINR performance at $p = 0.01$, INR = 19 dB (left), and UWB signal blanking loss vs number of signal clusters (right) in \mathbf{s} at $p = 0.05$ (solid lines) and $p = 0.01$ (dashed lines).	39
3.1	Proposed receiver structure for NBI mitigation in UWB communication system.	48
3.2	Error signal \mathbf{e}	52
3.3	Gaussian PDF and histogram of error signal.	52
3.4	Average BER performance of TH-BPSK UWB signal in the presence of NBI using the proposed and the conventional correlator based receiver in AWGN channel. Solid (-) and dashed (--) lines represent the conventional correlator and the proposed receiver performance, respectively, and "BPSK" (thick line) represents the BER performance with TH-BPSK UWB signal transmission without any NBI.	55
3.5	Average BER performance with TH-BPSK UWB signal transmission in the presence of NBI using the proposed and the conventional correlator based receiver in CM1 channel model. Solid (-) and dashed (--) lines represent the conventional correlator and the proposed receiver performance respectively, and "BPSK" (thick line) represents the BER performance with TH-BPSK UWB signal transmission without any NBI.	56
3.6	Average BER performance with TH-BPSK UWB signal transmission in the presence of NBI using the proposed and the conventional correlator based receiver in CM4 channel model. Solid (-) and dashed (--) lines represent conventional correlator and the proposed receiver performance, respectively. The "BPSK" (thick line) represents BER performance with TH-BPSK UWB signal transmission without any NBI.	57

3.7	BER performance with TH-BPSK UWB signal transmission in the presence of NBI using the proposed receiver in CM1 channel model. BER curves are generated by varying number of tone signals in NBI as mentioned in (3.6) at SIR = 0 dB.	58
3.8	BER vs SIR performance with TH-BPSK UWB signal transmission using the proposed receiver in CM1 channel model. BER curves are generated at SNR = 0, 10, and 20 dB. The “BPSK” (solid thick line) represents system performance without any NBI at SNR = 10 dB.	58
3.9	Average BER vs. SNR performance with TH-BPSK UWB signal transmission using the proposed receiver in the presence of non-tone bandpass NBI in CM1 channel model. Solid (—) and dashed (---) lines represent the conventional correlator and the proposed receiver performance, respectively. The “BPSK” (thick line) represents BER performance with TH-BPSK UWB signal transmission without any NBI.	59
4.1	Signal acquisition block diagram.	68
4.2	BER plot using the proposed ($\Phi_{Proposed}$) and random Gaussian ($\Phi_{Gaussian}$) measurement matrices at 30 percent CS ratio (CSR) for both simulation and theory. Theoretical results have been generated using (4.16).	73
4.3	Sparsity plot of the proposed measurement matrix $\Phi_{Proposed}$ for $M = 599$ and $N = 1499$	76
4.4	Coherence curves between the measurement matrix Φ and the sparsity matrix Ψ as a function of $\frac{M}{N}$ ratio.	80
4.5	Normalized mean squared error vs M/N ratio.	81
4.6	Average BER performance of TH-BSPK signal in CM1 and CM4 channel models at CSR = 80.	83
4.7	Average BER performance of TH-BSPK signal at 60 percent compressive sensing ratio in CM1 and CM4 channel models.	84
4.8	Average BER performance of TH-BSPK signal at 30 percent compressive sensing ratio in CM1 and CM4 channel models.	85
4.9	BER performance of TH-BSPK signal including the OMP signal recovery algorithm at CSR = 30 and CSR = 60 using the proposed and random Gaussian measurement matrices in CM1 channel model.	86
4.10	Average BER performance of TH-BSPK UWB signal in CS domain at CSR = 60 using the proposed and random Gaussian measurement matrices in CM1 channel model for $N_f = 1, 2$	86
4.11	Average BER performance vs SNR.	87
4.12	Average BER performance of the TH-BPSK UWB system in CM1 channel using the proposed measurement matrix with different values of P	88
5.1	The proposed UWB WSN with large antenna arrays at fusion center.	96
5.2	Amplitude envelope of UWB multipath channel.	112
5.3	Average detection error probability \mathcal{P}_E performance using the CD at FC in IEEE 802.15.4a multipath CM1 (“top”) and CM4 (“bottom”) channels for various number of sensor nodes in the network.	116
5.4	Average \mathcal{P}_E performance using the CD-based fusion in IEEE 802.15.4a multipath CM1 channel for various number of sensor nodes and antennas at FC.	117
5.5	Average detection error probability \mathcal{P}_E of event detection at FC using ED-based fusion in CM1 channel for the various number of sensor nodes K	117

5.6	Impact of N on the conditional PDF $f(\mathcal{E} d = 0)$ at fixed value of $K = 2$. The dashed and solid lines represent the PDF of first and second halves signal energy \mathcal{E}_0 and \mathcal{E}_1 in a frame respectively.	118
5.7	Average error probability \mathcal{P}_E performance using the various number of links (KN) in the sensor network.	119
5.8	Average false alarm \mathcal{P}_F and detection \mathcal{P}_D probabilities using various number of sensors (K) with $\Upsilon_{ED} = 0$ in the WSN system.	119
5.9	Average detection error probability using signal energy optimization at $K = 2$ and $N = 2$. The “Con” and “Opt” denote the conventional ED and the proposed energy optimization in (5.50) respectively.	120
5.10	Global detection probability \mathcal{P}_D performance at $\Upsilon_{ED} = 0$ and SNR =0, 5, 10, 15 dB, and it is also compared with observation bound (“Bound”). The observation bound is obtained using $K = 10$ and $\kappa = 2$	121
5.11	Impact of integration interval T_{int} on the \mathcal{P}_E	122
5.12	Effect of noise hardening on \mathcal{P}_E performance using the various K and the single antenna.	122
5.13	Impact of power optimization on \mathcal{P}_E performance using the various sensors and the single antenna in the WSN system. The solid and dashed lines denote the equal and optimized power respectively of the sensor nodes.	122

List of Tables

1.1	UWB channel model parameters	5
3.1	Literature review on NBI mitigation methods for UWB systems . . .	43
3.2	Value of parameters for TH-BPSK signal transmission	54
3.3	Computational complexity of NBI mitigation	60
4.1	Computational complexity of the proposed and Gaussian matrices . .	88

List of Abbreviations

5G fifth generation.

ADC analog-to-digital converter.

AWGN additive white Gaussian noise.

BC broadcast channel.

BER bit error rate.

BP basis pursuit.

BPSK binary phase-shift keying.

CIR channel impulse response.

CSI channel state information.

D2D device-to-device.

FC fusion center.

FCC Federal Communications Commission.

FD frequency domain.

GPS global positioning system.

i.i.d. independent and identically distributed.

IN impulse noise.

IoT internet of things.

IR-UWB impulse radio ultra-wideband.

ISI inter-symbol-interference.

LANs local area networks.

LOS line-of-sight.

M2M machine-to-machine.

- MAAs** massive antenna arrays.
- MAC** multiple access channel.
- MCA** morphological component analysis.
- MIMO** multiple-input multiple-output.
- mmWave** millimeter wave.
- MP** matching pursuit.
- MRC** maximal ratio combining.
- MUI** multiuser interference.
- NBI** narrowband interference.
- NLOS** non-line-of-sight.
- NLP** nonlinear processing.
- OFDM** orthogonal frequency division multiplexing.
- PDF** probability density function.
- POCS** projections onto convex sets.
- PPM** pulse position modulation.
- PSD** power spectral density.
- RFID** radio frequency identification.
- SC** selection combining.
- SNR** signal-to-noise ratio.
- TD** time domain.
- THz** terahertz.
- UWB** ultra-wideband.
- V2V** vehicular-to-vehicular.
- WBAN** wireless body area networks.
- WSN** wireless sensor network.

Notations and Symbols

\mathbb{Z}	integer numbers
\mathbb{R}	real numbers
$w(t)$	UWB pulse
$s(t)$	transmitted signal
$r(t)$	received signal
$n(t)$	AWGN
$i(t)$	impulse noise
$i_{\text{nbi}}(t)$	narrowband interference
σ_s^2	signal variance
σ_n^2	AWGN variance
T_f	frame duration
T_c	chip duration
T_h	channel delay spread
$\mathbb{E}[\cdot]$	expectation
$\text{Var}\{\cdot\}$	statistical variance
$*$	convolution operator
$[\cdot]^T$	transpose of $[\cdot]$
$ \mathcal{A} $	cardinality of set \mathcal{A}
$\langle \cdot, \cdot \rangle$	inner product operator
$\text{Pr}[\mathcal{A}]$	probability of \mathcal{A}
$X \sim \mathcal{N}(\mu, \Omega)$	X is normal distributed with mean μ and variance Ω
$ \cdot $	absolute value
\approx	approximate value
$n!$	factorial of n
$(\mathbf{a})^*$	complex conjugate of \mathbf{a}
$\binom{n}{k}$	binomial coefficient of n choose k
$\ (\cdot)\ _2$	Euclidean norm of a signal (\cdot)
$\arg \max_i b_i$	index i corresponding to the largest b_i
$\arg \min_i b_i$	index i corresponding to the smallest b_i
\mathbf{I}_N	denotes the $N \times N$ identity matrix
$\mathbf{0}_{N \times L}$	denotes the $N \times L$ matrix with all entries zero
$\mathbf{1}_{N \times L}$	denotes the $N \times L$ matrix with all entries one
$\lceil x \rceil$	ceiling function and defined as $\min\{n \in \mathbb{Z} n \geq x\}$
$Q(x)$	Q-function and defined as $\frac{1}{\sqrt{2\pi}} \int_x^\infty \exp(-x^2/2) dx$

Chapter 1

Introduction

1.1 Overview

Wireless communication is one of the most vibrant and fast growing area in communication technology today. There is an emergence of newer technologies for various communication and computing applications ranging from 3G/4G/5G cellular communication, indoor and outdoor Wi-Fi, satellite television, imaging and localization, radio frequency identification (RFID) applications and many more.

The internet of things (IoT) is the next step in the evolution of the Internet due to big innovations in wireless technology and is one of the main focus of the next generation smart environments. It is expected that mobile data traffic will experience 8-10 fold growth by 2021 and the number of wireless mobile connected devices will reach around 50 billion by 2020 [1]. Main factors of this exponential growth and wider acceptance are the integration of several technologies and communications solutions such as wired and wireless sensor and actuator networks, next generation communication protocols, identification technologies, and artificial intelligence for smart objects. For IoT-based applications, ultra-wideband (UWB) technology offers attractive solutions to a broad class of problems in imaging, localization, identification, and communication due to its large bandwidth, low power consumption and device cost.

1.2 UWB technology

The UWB technology utilizes very large bandwidth for information exchange. The Federal Communications Commission (FCC) has defined the signal bandwidth of at least 500 MHz or a fractional bandwidth (FBW) exceeding 20% for UWB communication [2]. The FBW of a signal is defined as

$$\text{FBW} = \frac{2(F_H - F_L)}{F_H + F_L}, \quad (1.1)$$

where F_H and F_L are the 10 dB higher and lower frequencies of the transmitted UWB signal respectively. Therefore, bandwidth of the UWB signal is huge and very large as compared to the conventional narrowband communication signals [2–5]. The FCC authorized the unlicensed use of UWB in the frequency range from 3.1 GHz to 10.6 GHz that results in UWB signal overlapping with narrowband communication signals. The maximum power spectral density emission is limited by the FCC to -41.3 dBm/MHz for UWB transmitters. The FCC UWB emission mask is depicted in Figure 1.1. The very large signaling bandwidth and low power of UWB signals reveal several potential and attractive features, including the high-data-rate communications, very accurate ranging and localization, and the possibility of low-complexity devices. Due to these merits, UWB communications have wide interest as an enabling technique that provides low-power and low-complexity UWB transmissions especially to connect various devices in IoT applications in unlicensed spectrum.

Impulse radio (IR) and multi-band orthogonal frequency-division multiplexing (MB-OFDM) are two UWB transmission techniques. In IR technique very short pulses (of very large bandwidth) with relatively low energy are used for the transmission. On the other hand, MB-OFDM technique divides the UWB frequency spectrum to multiple orthogonal bands for communications. In this thesis, IR-UWB technique is used for communication due to its low complexity and precise localization and ranging capability [2, 3, 5–8]. Thus, henceforth IR-UWB communication

is referred as UWB communication in the thesis.

Further, the availability of unlicensed millimeter wave (mmWave) spectrum from 30 GHz to 300 GHz has brought renewed interest in UWB technology. Hence, more signal bandwidth and high allowable power are available at these frequencies specially around 60 GHz as compared to conventional 0 – 10 GHz frequency range [7, 9]. The FCC regulations for UWB communication in the unlicensed mmWave spectrum do not have stringent emission norms due to the higher oxygen absorption which limits the long-distance interference to the other devices. For example, FCC allows the devices to transmit power up to 10 W in the 57 – 64 GHz band [8]. Furthermore, moving to higher frequencies the small size of antennas also allow compact device implementations and multiple antennas.

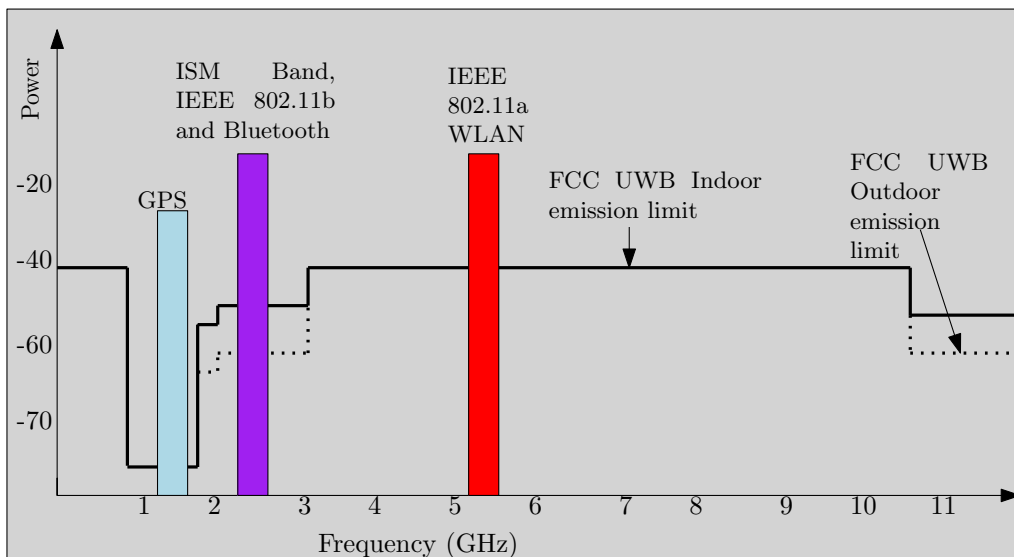


Figure 1.1: UWB emission limits (in dBm) restricted by the FCC.

1.3 UWB signal propagation characteristics

Performance of a communication systems to a large extend is determined by the channel conditions. Thus, accurate modeling of channel characteristics is essential for wireless communication systems. For channel modeling, the deterministic and the statistical methods are used in the literature [6]. In deterministic channel modeling, the ray-tracing techniques are used by considering obstacles' geometric

shape, type and its electro-magnetic (EM) properties in the propagation environment. However, deterministic channel modeling is not suitable when the operating environment changes. To model the changes in the operating environment statistical channel modeling is used. The statistical models are based on extensive measurements campaigns and they give the received envelope and the path arrival time distribution. Many popular IEEE UWB standards use this form of channel modeling.

Due to the large bandwidth of UWB signals, its channel propagation characteristics are different than a narrowband communication signal [6]. The techniques to model the physics of UWB signal propagation in a mathematical as well as numerically treatable way is studied in the literature for indoor, outdoor and intra-vehicle, tunnels and within mines communications [4–6, 10, 11]. The Saleh and Valenzuela channel (SV channel) model is one of the most widely used statistical channel models for indoor UWB signal propagation [6]. This model is adopted in IEEE 802.15.4a standard for providing a stochastic channel model for various UWB environments [6, 12] and we briefly summarize this channel model and its main parameters.

The SV channel consists of multiple clusters and multipath components (MPCs) within a cluster and the discrete channel impulse response (CIR) is expressed as [6, 8]

$$h(t) = \sum_{c=0}^{C-1} \sum_{m=0}^{M-1} \alpha_{c,m} \delta(t - T_c - \tau_{c,m}), \quad (1.2)$$

where C and M are the total number of clusters and MPCs within a cluster respectively and $\delta(\cdot)$ is the Kronecker delta function. $\alpha_{c,m}$ is the tap weight of the m^{th} component in the c^{th} cluster, T_c is the delay of the c^{th} cluster, and $\tau_{c,m}$ is the delay of the m^{th} MPC relative to the c^{th} cluster arrival time T_c . The CIR $h(t)$ has clusters and MPCs within a cluster that follow Poisson distribution with arrival rates Λ and λ respectively. The mean cluster energy decays exponentially with parameter Γ . The value of Γ , Λ and λ depend on the UWB signal propagation environments. The typical pictorial representation of CIR $h(t)$ is shown in Figure 1.2.

The path gains $\alpha_{c,m}$ may be restricted to real values, since IR-UWB transmission

operates in the baseband. Unlike narrowband communication channels, central limit theorem cannot be applied due to the high multipath resolution, and the path gains probability density function does not match the Gaussian distribution. Therefore, Rayleigh, Nakagami, or lognormal distributions are considered for the amplitude $\alpha_{c,m}$ [6, 13]. Exemplarily, the major parameters of UWB channel model for indoor residential transmission in line-of-sight (LOS) and non-line-of-sight (NLOS), and indoor office LOS and NLOS environments are summarized in Table 1.1 [6, 14].

Table 1.1: UWB channel model parameters

Parameters	Residential LOS (CM1)	Residential NLOS (CM2)	Office LOS (CM3)	Office NLOS (CM4)
Average number of clusters (C)	3	3.5	5.3	3.1
Cluster decay time (Γ)	22.61 ns	26.27 ns	14.6 ns	19.8 ns
Intra-cluster decay time (τ)	12.53 ns	17.50 ns	6.4 ns	11.2 ns
Cluster arrival rate (Λ)	0.047 ns^{-1}	0.12 ns^{-1}	0.016 ns^{-1}	0.19 ns^{-1}
Intra-cluster arrival rate (λ)	1.54 ns^{-1}	1.77 ns^{-1}	0.19 ns^{-1}	0.11 ns^{-1}

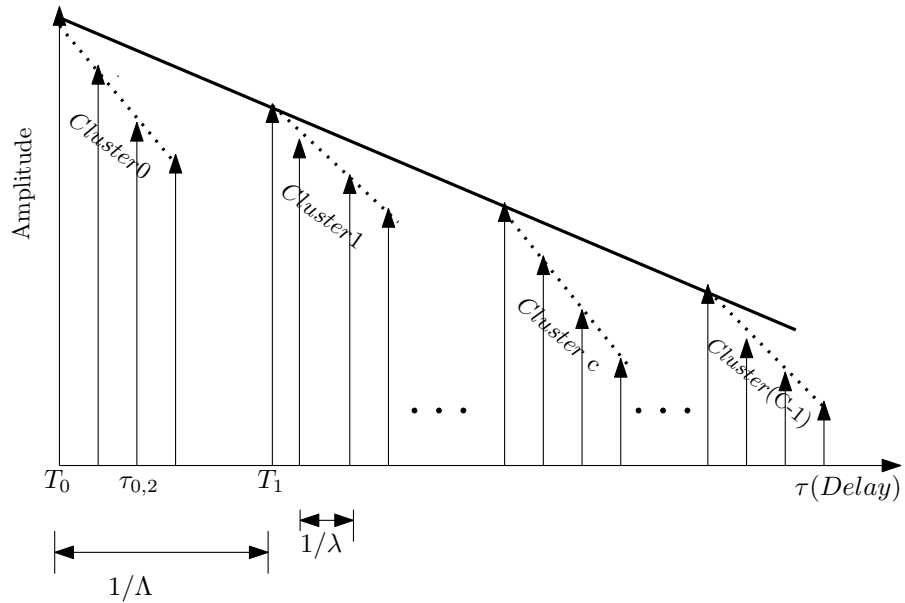


Figure 1.2: A pictorial view of the UWB channel model.

1.4 UWB standardization

For IR-UWB communication mainly two standards IEEE 802.15.3a and IEEE 802.15.4a are proposed for high and low data rate applications respectively [8].

IEEE 802.15.3a

The standard IEEE 802.15.3a was developed for high rate applications in wireless personal area networks (WPANs). The primary aim of this standards committee was to develop the channel model which can be used for UWB system evaluation using both IR-UWB and multiband-based UWB communications. The IEEE 802.15.3a supports data rates of 12Mb/s to 480Mb/s, and application of this standard is envisaged for cable-less media transfer, imaging, and multimedia streaming [12]. However, this standard was withdrawn in 2006.

IEEE 802.15.4a

This standard was initially proposed in 2006 for low data-rate WPANs applications [12], and after updation currently it is known as the IEEE 802.15.4-2015 [12]. The data rate is supported by IEEE 802.15.4 for UWB communication from 0.11 Mb/s to 27Mb/s, over different frequency bands (less than 10.6 GHz) and authorized by regulatory bodies in most of the main geographies worldwide for 10-100 meter communication range [15]. This standard also includes support for ranging and location capability. Various standard UWB channel models in operating environments like indoor LOS, office LOS industry LOS, indoor NLOS, etc are studied in IEEE 802.15.4a. The potential applications of IEEE 802.15.4a includes IoT and home automation applications. In this thesis, IEEE 802.15.4a standard is used to demonstrate and evaluate the various proposed methods and their benefits. Further, multiband UWB communication also exists in ECMA-368 standard for data rates up to 480 Mbps [12].

IEEE 802.15.6

This is the latest international standard for wireless body area networks (WBAN) to support various real-time health monitoring applications using low power and

extremely reliable wireless communication within the surrounding area of the human body. The IEEE 802.15.6 standard defines both the medium access control (MAC) and physical layer (PHY) specifications for WBAN. This standard uses different frequency bands such as UWB, narrowband (NB), and human body communication (HBC) with highly secure authentication and encryption. The UWB uses low power and provides very accurate localization with high data rate, thus is most suitable for WBAN [12, 16, 17].

1.5 UWB applications

UWB technology have many applications particularly in communication, radar and imaging, ranging and medicine due to its low power and large bandwidth.

1.5.1 UWB in communication

UWB supports both the low and high data rate applications for medium and short range communications. According to the Shannon-Hartley theorem, the reliable data rate capacity of the system can be increased either by increasing the channel bandwidth or signal-to-noise ratio (SNR), or both. Since UWB systems have enormous bandwidths, it is possible to achieve high data rate. However, the UWB emission is compliant with FCC mask that results in low power of UWB signals. This will limit the range of the wireless communication and thus, UWB is suitable for high-rate, low range applications such as wireless USB, multi-media streaming, machine-to-machine (M2M) and device-to-device (D2D) communications, etc. Further, UWB communication is immune to multipath and multiuser interference due to a very high time domain resolution of multipaths and low duty cycle of UWB signal. UWB also provides scalability in terms of data rate, communication range and power due to duty cycled UWB pulse transmission. This can enable several low rate applications of UWB communication in wireless sensor network (WSN) and IoT based applications.

1.5.2 UWB in ranging

The UWB signals enable ranging and positioning with sub-centimeter precision and penetrate effectively through various materials due to high time resolution and wide frequency range [2]. Therefore, it is used in radar imaging and localizations methods.

The global positioning system (GPS) has been widely considered for positioning and tracking technology. However, indoor environments still pose significant challenges for GPS systems. GPS positioning systems are severely degraded or may fail altogether in indoor environments where the satellite or cellular signals are interrupted, and in scenarios with deep shadowing effects due to complex physical characteristics of the environments, such as walls, windows, etc. Further, a typical GPS signal occupies a bandwidth of only 2 MHz, thereby resulting in overlapped MPCs. Thus, this makes localization accuracy of GPS relatively low. Therefore, UWB is a good candidate for indoor localization and can provide high level position accuracy required for indoor positioning. This has also enabled several applications in the area of inventory tracking, assisted living, sports and intelligent transportation systems. Further, UWB can also be used for monitoring of operating conditions in industrial facilities due to its extremely accurate ranging feature. For ranging, time-of-arrival (ToA), time difference of arrival (TDoA), received signal strength (RSS) based fingerprinting, angle of arrival (AoA) or hybrid methods are used for indoor environments [2].

1.5.3 UWB in medicine

UWB signal's noise-like behavior (due to extremely low emission power) makes UWB technology useful for biomedical applications. UWB signals are commonly used in accurate medical imaging and sensing [18] such as ear-nose-throat (ENT) and pneumology imaging. The UWB medical radar can be used for monitoring cardiac and respiratory motion, blood pressure and hyperthermia applications. UWB is also used in intensive care units to monitor coma patients, to detect when they come out

of the coma, so that much need medical attention can be provided when they wake up to avoid too many wires around the patient. The UWB signal's ability to provide accurate indoor localization can be used to monitor patients suffering from chronic disease for assisted living. UWB can also be used for non-intrusive disease diagnosis of ENT organs [8]. Further, UWB technology can be used in capsule endoscopy for wireless communication interface. Figure 1.3 shows the potential applications of UWB technology in various fields.

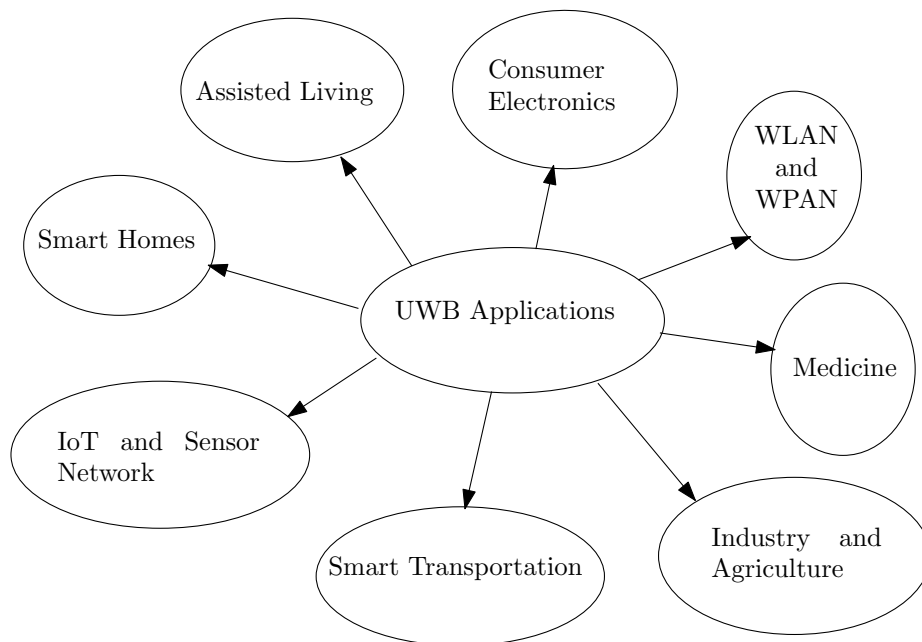


Figure 1.3: A graphical representation of UWB applications.

1.6 Performance measures

To compare the proposed algorithms (methods) with existing algorithms, following performance measures are used in this work:

SNR

SNR is the most basic performance measure in wireless communication system, which is used to quantify the noise in the desired signal. SNR is defined as the ratio of signal power P_{signal} to the noise power P_{noise} , and is defined as

$$\text{SNR} = \frac{P_{\text{signal}}}{P_{\text{noise}}} \quad (1.3)$$

The signal power P_{signal} ¹ depends on the transmitted signal power and the channel gain. The P_{noise} also denotes the variance of the zero mean noise and SNR often expressed in decibels (dB). In general, high SNR is desirable by reducing the P_{noise} for fixed P_{signal} in the communication systems.

SINR

The signal-to-interference-plus-noise ratio (SINR) is defined as the power of a certain desired signal divided by the sum of the interferers and background noise power. The SINR is defined as

$$\text{SINR} = \frac{P_{\text{signal}}}{P_{\text{interference}} + P_{\text{noise}}}, \quad (1.4)$$

where $P_{\text{interference}}$ is the interference power in the system. If the interference power is zero, SINR is equal to the SNR in a system. For better communication, $P_{\text{interference}}$ and P_{noise} should be as small as possible. In the UWB system, interference is introduced due to multiuser, narrowband communication or other sources.

Bit error rate (BER)

The bit error rate (BER) is another important measure to evaluate the wireless communication systems' performance. It is a measure of number of received bits in error. The BER may be affected by the operating channel noise, interference, distortion, improper bit synchronization, attenuation, multipath fading, etc. in the wireless communication system at the receiver side. For better communication, BER should be minimum at low signal power.

ToA

This is another important parameter used for signal based ranging applications. ToA is the travel time of a radio signal from a single transmitter to a remote single receiver. ToA finds the distance between the transmitter and the receiver. UWB ranging requires precise estimation of ToA of first path (FP) signal. However, estimation of ToA is challenging in the presence of interference, background noise and multipath in the UWB system at low SNR.

¹It also denotes the variance of zero mean signal

1.7 UWB pulses

For UWB communications, various pulse shapes are proposed in the literature such as Gaussian, Hermite and linear combination of Gaussian and Hermite pulses [19–23]. However, Gaussian and Hermite pulses do not satisfy the FCC spectral mask for UWB communication. Hence, to utilize them for information exchange in the UWB system, a suitable filtering based methods is described in [19]. For better system performance, ratio between the transmitted pulse power to the area of FCC spectral mask must be close to unity. In [19] it is shown that the area of power spectral density (PSD) of Gaussian or Hermite pulses is very small as compared to the area of FCC spectral mask. Therefore, these pulses do not fully utilize the UWB spectra for power constraint communications. If we increase the derivative order of the Gaussian pulse, then the spectra of pulse increases towards the higher frequency. Higher derivatives of Gaussian pulse have close resemblance to modulated Gaussian pulse, hence higher derivatives (especially greater than five) are more suitable to fit in the FCC spectral mask without any filtering. However, their spectral utilization is still poor for maximum transmitted signal power in the UWB communication.

For instance, we consider the Gaussian pulse $g(t)$, as given in [19, 24]

$$g(t) = A \exp(-2\pi (t/\tau)^2), \quad t \in \mathbb{R} \quad (1.5)$$

where τ is the time scaling parameter and A is the amplitude adjusting parameter. The n^{th} derivative of $g(t)$ is expressed as

$$g_n(t) = \frac{d^n}{dt} (g(t)). \quad (1.6)$$

For example, the second derivative Gaussian pulse is expressed as

$$w(t) = g_2(t) = A \left(1 - \frac{4\pi t^2}{\tau^2} \right) \exp(-2\pi(t/\tau)^2) \quad (1.7)$$

In [25], a UWB pulse was proposed and compared with the sixth derivative of Gaussian pulse. Pulse proposed in [25] has better performance compared to derivatives of Gaussian, Hermite and Prolate spheroidal pulses and pulse proposed in [26] in multiuser environment with FCC and noise constraints. The proposed Norman pulse, $p_n(t)$ in [25] can be written as

$$p_n(t) = \text{sinc}(2Bt) \cos(2\pi f_c t) \quad t \in \mathbb{R} \quad (1.8)$$

where $B = 3.75$ GHz and $f_c = 6.85$ GHz is the modulation frequency. The $\text{sinc}(\cdot)$ function is given as

$$\text{sinc}(t) = \begin{cases} \frac{\sin(\pi t)}{\pi t} & \text{if } t \neq 0 \\ 1 & \text{if } t = 0 \end{cases} \quad (1.9)$$

Further, UWB pulse generated using the projections onto convex sets (POCS) algorithm is described below.

1.7.1 UWB pulse using POCS algorithm

In this section, POCS algorithm is introduced, and required constraint sets for pulse design are formulated based on a-priori information about the UWB characteristics. The POCS algorithm defines a systematic numerical approach for finding a point in the intersection of closed and convex constraint sets [27]. Based on a-priori information few constraint sets, such as C_1, C_2, \dots, C_m are formulated in the Hilbert space $L^2(\mathbb{R})$. Each set is closed and convex, and their intersection $C_0 = \cap_{i=1}^m C_i$ is non-empty. The orthogonal projection onto the set C_i is given by the minimum distance between any arbitrary function in Hilbert space and set C_i . The projection onto set C_i is defined as

$$P_{C_i}x(t) = \min_{y(t) \in C_i} \|x(t) - y(t)\|, i = 1, 2, \dots, m \quad (1.10)$$

where $x(t)$ is any arbitrary function in Hilbert space $L^2(\mathbb{R})$. Sets are closed and convex in Hilbert space, hence unique projection onto each set exists [27]. The iterates $\{x_k(t)\}$ are generated by

$$x_{k+1}(t) = P_{C_m}P_{C_{m-1}}\dots P_{C_2}P_{C_1}x_k(t) \quad (1.11)$$

with an arbitrary starting point $x_0(t)$ in the Hilbert space $L^2(\mathbb{R})$, will converge weakly to a point of C_0 [27] and equation (1.11) is referred to as the POCS algorithm. For UWB pulse design, FCC mask and nature of UWB pulse provide a-priori information to formulate constraint sets. The POCS based approach is flexible and optimum for UWB pulse design because sets can be reformulated according to the new FCC mask.

In the POCS algorithm for UWB pulse design, four constraint sets are considered. The condition for closedness and convexity are also discussed along with the respective constraint set. The first constraint set, C_1 , is formulated based on the PSD of the UWB pulse. The autocorrelation function (ACF), $r_x(\lambda)$, of any arbitrary pulse $x(t) \in L^2(\mathbb{R})$ is defined as

$$r_x(\lambda) = \int_{-\infty}^{\infty} x(t)x(t-\lambda)dt, \quad \lambda \in \mathbb{R} \quad (1.12)$$

where λ is the time lag. The PSD, $S_x(\omega)$, of pulse $x(t)$ is the forward Fourier transform of $r_x(\lambda)$. The set C_1 is defined as

$$C_1 = \{r_x(\lambda) : S_x(\omega) \leq D(\omega)\} \quad (1.13)$$

where $D(\omega)$ is the FCC spectral mask. The set C_1 is closed and convex as given in [27], and projection of any arbitrary signal $x(t) \in L^2(\mathbb{R})$ onto the set C_1 is given as [27]:

$$\hat{S}_x(\omega) = \begin{cases} S_x(\omega), & |S_x(\omega)| \leq D(\omega) \\ D(\omega), & \text{otherwise} \end{cases} \quad (1.14)$$

The projection point $P_{C_1}r_x(\lambda)$ is the inverse Fourier transform of $\widehat{S}_x(\omega)$ and in the set C_1 . The time domain pulse which is in the set C_1 , is obtained by inverse Fourier transform of square root of $\widehat{S}_x(\omega)$.

The second constraint set, C_2 , is formulated to limit the time duration of the pulse. The mask $D(\omega)$ has sharp corners therefore pulse is not time limited. Hence, another set C_2 is formulated, which limits the time duration of the pulse in the interval $[0, T]$. Hence, duration of ACF of pulse is generally not zero in the interval $[-T, T]$. This duration limited set C_2 of the designed pulse is defined as:

$$C_2 = \{r_x(\lambda) \in L^2(\mathbb{R}) : r_x(\lambda) = 0, |\lambda| > T\} \quad (1.15)$$

Convexity and closedness of set C_2 : Consider the two functions $r_{x1}(\lambda)$ and $r_{x2}(\lambda)$ in the set C_2 . For convexity, one has to show that another function $r_{x3}(\lambda) = \mu r_{x1}(\lambda) + (1 - \mu)r_{x2}(\lambda)$, $\mu \in [0, 1]$ is in the set C_2 .

$$r_{x3}(\lambda) = 0 \quad \text{if } |\lambda| > T \quad (1.16)$$

equation (1.16) is obtained by putting both $r_{x1}(\lambda)$ and $r_{x2}(\lambda)$ as zero for $|\lambda| > T$. Thus, $r_{x3}(\lambda) \in C_2$. For proving closedness of the set C_2 , let $\{r_{xn}(\lambda)\}$ be a sequence of functions in the set C_2 and $r_{xn}(\lambda) \rightarrow r_x^*(\lambda)$ as $n \rightarrow \infty$.

$$\|r_{xn}(\lambda) - r_x^*(\lambda)\|^2 = \int_{-\infty}^{\infty} |r_{xn}(\lambda) - r_x^*(\lambda)|^2 d\lambda$$

$$\|r_{xn}(\lambda) - r_x^*(\lambda)\|^2 = \int_B |r_{xn}(\lambda) - r_x^*(\lambda)|^2 d\lambda + \int_{B^c} |r_{xn}(\lambda) - r_x^*(\lambda)|^2 d\lambda$$

$$\|r_{xn}(\lambda) - r_x^*(\lambda)\|^2 \geq \int_{B^c} |r_{xn}(\lambda) - r_x^*(\lambda)|^2 d\lambda$$

$$\|r_{xn}(\lambda) - r_x^*(\lambda)\|^2 \geq \int_{B^c} |r_x^*(\lambda)|^2 d\lambda, \quad \because r_{xn}(\lambda) = 0, \lambda \in B^c$$

as $n \rightarrow \infty$, $\|r_{xn}(\lambda) - r_x^*(\lambda)\|^2 \rightarrow 0$, therefore,

$$\int_{B^c} |r_x^*(\lambda)|^2 d\lambda \rightarrow 0 \quad (1.17)$$

and $r_x^*(\lambda) = 0, \lambda \in B^c$, where $B = |\lambda| \leq T$ and $B^c = |\lambda| > T$. Hence, the set C_2 is closed and convex.

The projection of any arbitrary signal $x(t)$ in Hilbert space $L^2(\mathbb{R})$ onto the set C_2 is given as [27]

$$P_{C_2} r_x(\lambda) = \begin{cases} r_x(\lambda), & |\lambda| \leq T \\ 0, & \text{otherwise} \end{cases} \quad (1.18)$$

where $r_x(\lambda)$ is the ACF of signal $x(t)$.

The third constraint set is imposed based on a-priori information of ACF. From the symmetric property of $r_x(\lambda)$, constraint set C_3 is defined as

$$C_3 = \{r_x(\lambda) \in L^2(\mathbb{R}) : S_x(\omega) \in \mathbb{R}_+, \forall \omega\} \quad (1.19)$$

where $S_x(\omega)$ is the Fourier transform of $r_x(\lambda)$ and \mathbb{R}_+ is the positive real line.

Convexity and closedness of set C_3 : Consider the two function $r_{x1}(\lambda)$ and $r_{x2}(\lambda)$ in the set C_3 . For convexity, one needs to prove that another function $r_{x3}(\lambda) = \mu r_{x1}(\lambda) + (1 - \mu)r_{x2}(\lambda), \mu \in [0, 1]$ is in the set C_3 . Using linearity property of Fourier transform

$$S_{x3}(\omega) = \mu S_{x1}(\omega) + (1 - \mu)S_{x2}(\omega)$$

$$S_{x3}(\omega) \in \mathbb{R}_+$$

For proving closedness, let $\{r_{xn}(\lambda)\}$ be a sequence of functions in the set C_3 and $r_{xn}(\lambda) \rightarrow r_x^*(\lambda)$ as $n \rightarrow \infty$.

$$S_{xn}(\omega) \in \mathbb{R}_+, \forall n$$

where $S_{xn}(\omega)$ is the Fourier transform of $r_{xn}(\lambda)$, as $n \rightarrow \infty$,

$$S_x^*(\omega) \in \mathbb{R}_+$$

Hence, set C_3 is closed and convex, and the projection of any arbitrary signal $x(t)$ in Hilbert space $L^2(\mathbb{R})$ onto the set, C_3 is defined as

$$P_{C_3}r_x(\lambda) = \mathcal{F}^{-1}\{Re\{\mathcal{F}\{r_x(\lambda)\}\}\} \quad (1.20)$$

where \mathcal{F} and \mathcal{F}^{-1} represent Fourier transform and inverse Fourier transform respectively. ACF has maximum value at zero lag and can also be included in the form of another constraint set in the pulse designing.

The fourth constraint set, C_4 , is based on the radiation property of transceiver antenna. The antenna cannot radiate the DC component of transmitted pulse [19]. Therefore, transmitted pulse in the UWB communication must have zero DC value. The constraint set C_4 is hence defined as:

$$C_4 = \{r_x(\lambda) : S_x(\omega = 0) = 0\} \quad (1.21)$$

where $S_x(\omega = 0)$ is the Fourier transform of function $r_x(\lambda)$ at frequency $\omega = 0$.

Convexity and closedness of set C_4 : Consider the two function $r_{x1}(\lambda)$ and $r_{x2}(\lambda)$ in the set C_4 . For convexity, one should prove that another function $r_{x3}(\lambda) = \mu r_{x1}(\lambda) + (1 - \mu)r_{x2}(\lambda)$, $\mu \in [0, 1]$ is in the set C_4 . Taking Fourier transform on both sides, $S_{x3}(\omega)$ (Fourier transform of $r_{x3}(\lambda)$) is represented as

$$S_{x3}(\omega) = \mu S_{x1}(\omega) + (1 - \mu)S_{x2}(\omega)$$

$$S_{x3}(\omega = 0) = 0$$

For proving closedness, let $\{r_{xn}(\lambda)\}$ be a sequence of functions in the set C_4 and

$r_{xn}(\lambda) \rightarrow r_x^*(\lambda)$ as $n \rightarrow \infty$.

$$S_{xn}(\omega = 0) = 0, \forall n$$

where $S_{xn}(\omega)$ is the Fourier transform of $r_{xn}(\lambda)$. As $n \rightarrow \infty$,

$$S_x^*(\omega = 0) = 0$$

Hence, the set C_4 is closed and convex in Hilbert space $L^2(\mathbb{R})$. The projection of any arbitrary signal $x(t)$ in Hilbert space $L^2(\mathbb{R})$ onto the set C_4 is defined as

$$\widehat{S}_x(\omega) = \begin{cases} S_x(\omega), & \text{if } x(t) \in C_4 \\ S_x(\omega) - S_x(\omega = 0), & \text{otherwise} \end{cases} \quad (1.22)$$

The projection point $P_{C_4}r_x(\lambda)$ is the inverse Fourier transform of $\widehat{S}_x(\omega)$ and is in the set C_4 .

Hence, the POCS algorithm utilizing the four constraint sets for designing a UWB pulse is defined as

$$x_{n+1}(t) = P_{C_4}P_{C_3}P_{C_2}P_{C_1}x_n(t), \quad n = 0, 1, 2, \dots \quad (1.23)$$

where $x_0(t)$ is the starting initial signal in the Hilbert space $L^2(\mathbb{R})$. All the constraint sets in (1.23) are closed and convex in space $L^2(\mathbb{R})$ as discussed above, therefore signal $x_n(t)$ in (1.23) converge weakly to a signal in the set $C_0 = C_1 \cap C_2 \cap C_3 \cap C_4 \in L^2(\mathbb{R})$.

The flow chart of POCS algorithm implementation is shown in Figure 1.4. The threshold value is predefined and $x_n(t)$ is obtained using (1.23) in Figure 1.4.

In Figure 1.5, the PSD of sixth derivative Gaussian pulse, $g_6(t)$, Norman pulse, $p_n(t)$ proposed by Norman et al in [25], Lee pulse, $p_l(t)$ proposed by Lee in [28] and the pulse designed using POCS algorithm, $x(t)$ along with the FCC spectral mask. The Lee pulse, $p_l(t)$ has a DC component and is spectrally inefficient as shown in Figure 1.5. It is also observed from Figure 1.5 that Norman pulse $p_n(t)$ [25] and

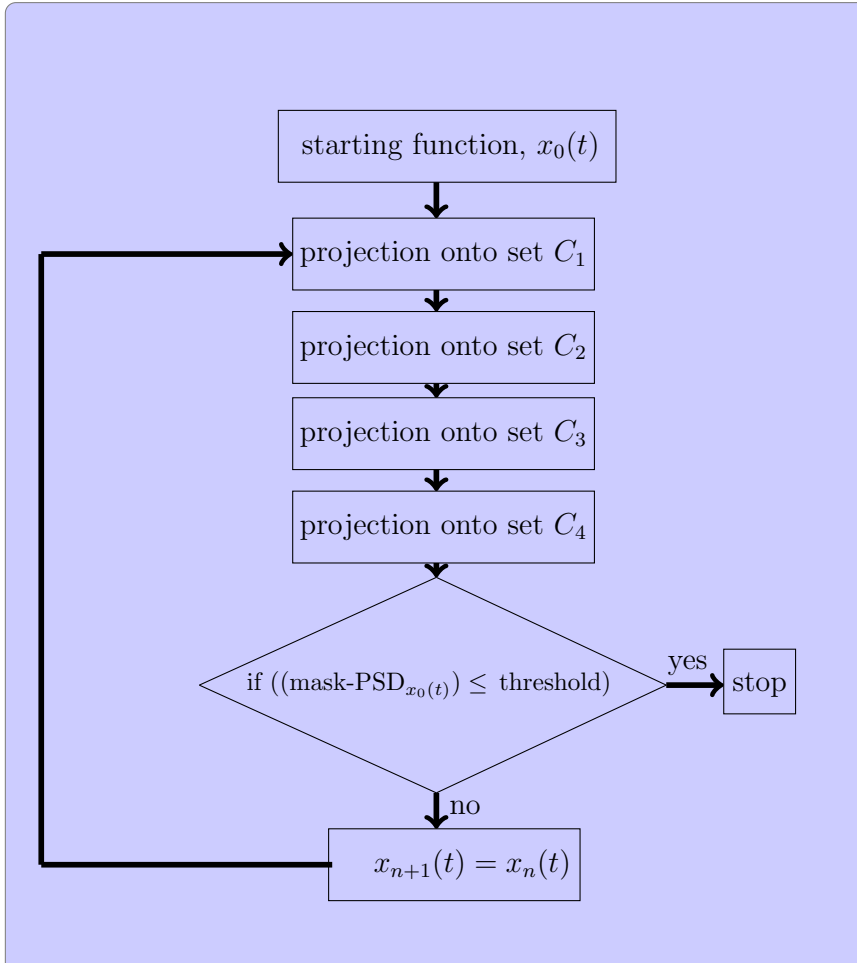


Figure 1.4: Flow chart of POCS algorithm for UWB pulse design.

the sixth derivative Gaussian pulse, $g_6(t)$ are spectrally compatible with the FCC mask, however spectral utilization of FCC mask is sub-optimal. The designed pulse using POCS algorithm, $x(t)$ fits the FCC mask as shown in Figure 1.5 while other pulses mostly cover the flat region from 3.1 GHz to 10.6 GHz band. Area under the PSD of $p_l(t)$ [28], $p_n(t)$ and $g_6(t)$ is smaller than area under the PSD of the POCS-based pulse, $x(t)$, as observed from the Figure 1.5, hence, the transmitted signal power is higher (compliant with FCC mask) for $x(t)$ under the FCC constraint. To generate the sixth derivative Gaussian pulse, $g_6(t)$, time scaling parameter, $\tau = 0.145$ nanoseconds is considered and absolute amplitude adjusting parameter, A is scaled suitably to limit the maximum value of PSD within FCC mask as shown in Figure 1.5. The Norman pulse, $p_n(t)$ in (1.8) is generated using $B = 3.75$ GHz, $f_c = 6.85$ GHz and is consistent with [25].

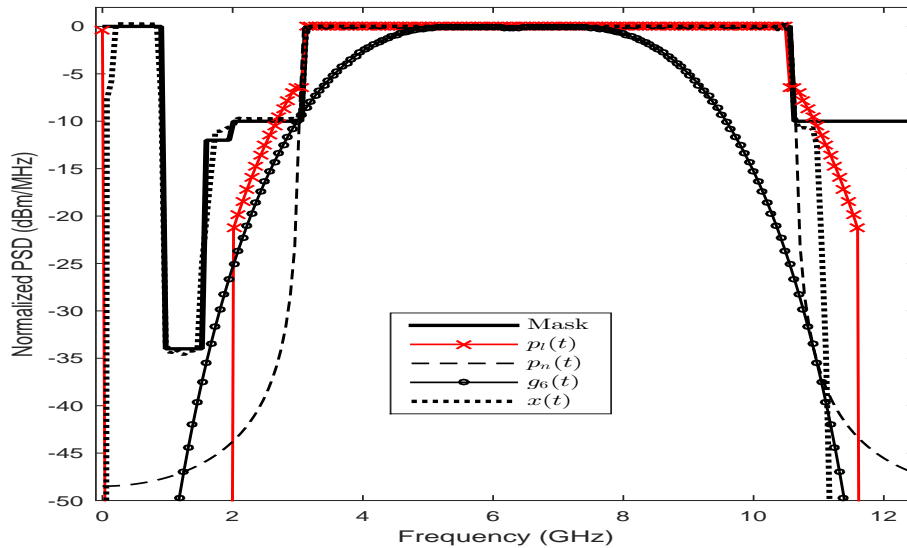


Figure 1.5: PSD of Norman pulse $p_n(t)$, sixth derivative Gaussian pulse $g_6(t)$, Lee pulse $p_l(t)$ and POCS-based pulse $x(t)$ with FCC spectral mask.

1.8 Sparse signals

A signal $x(t)$ can be represented in some basis ψ as

$$x(t) = \sum_i \alpha_i \psi_i(t), \quad (1.24)$$

where $\{\psi_i(t)\}$ s are the basis function such as sinusoids, wavelets and curvelets. $\{\alpha_i\}$ s are the expansion coefficients in $\psi_i(t)$ domain. Equation (1.24) is also represented as $x(t) = \Psi(t)\alpha$, where $\alpha = [\alpha_1, \alpha_2, \dots, \alpha_i]^T$ and $\Psi(t) = [\psi_1(t), \psi_2(t), \dots, \psi_i(t)]$. The magnitude of transform coefficients ($\{\alpha_i\}$ s) decay rapidly, hence, signal of interest $x(t)$ can be well-represented by a small number of transform coefficients in some appropriate basis. Thus, signal has only a small number of non-zero elements compared to the total number of elements, referred to as sparse signal.

Further, discrete signal $x = \{x_i\}_{i=1}^n$ is a signal of interest and its non-zero elements (sparsity of signal) is defined as

$$\|x\|_0 = \#\{i : x_i \neq 0, i = 1 \text{ to } n\}, \quad (1.25)$$

where $\#$ represents a number. Thus, a sparse signal has small value of $\|x\|_0$ as compared to total elements n . The $\|x\|_0$ is also referred to as ℓ_0 -norm. Sparse approximation of a signal has been extensively used in signal processing, wireless communication, image processing, machine learning, medical imaging, array processing, data mining and etc. For example, in compressive sensing for efficiently acquiring and reconstructing a signal, the sparsity of underlying signal is used to find the solution of an underdetermined linear system. An example of the sparse signal in the time domain is shown in Figure 1.6. Signal in Figure 1.6 has only few non-zero elements ($\approx 6.5\%$) as compared to the total number of elements ($n = 600$). In this thesis, the sparsity of the received UWB signals is exploited to enhance the UWB system performance or to reduce its implementation complexity.

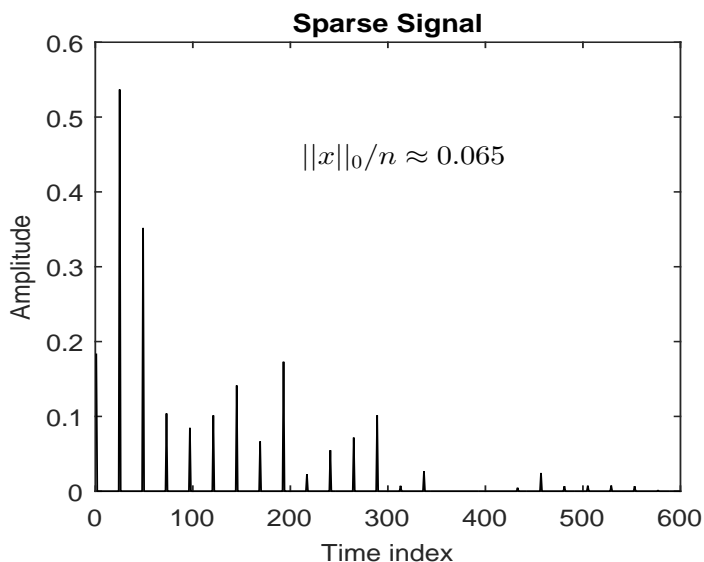


Figure 1.6: An example of a sparse signal.

1.9 Motivation

UWB communication is a proposing unlicensed technology for IoT based applications, and short range D2D and M2M communications due to its large bandwidth and low power characteristics. Hence, UWB communication schemes have been standardized for next-generation localization, identification, imaging and short range wireless communication systems such as IEEE 802.15.3a, IEEE 802.15.4a and IEEE

802.15.6. Further, increasing number of electronic devices with wireless networking capabilities need several licensed and unlicensed technologies for seamless connectivity. Of these, the low power and low cost UWB technology is a viable solution in picocell and femtocell networks. Moreover, UWB communication ensures robustness to severe multipath fading and multiuser communication scenario even in indoor environments. Products using IR-UWB are commercially available for real-time locating systems (RTLS) from industry pioneers, such as Time-Domain and DecaWave [29], which further push the UWB technology for precise and high update rate RTLS of assets and personnels.

Recent progress in semiconductor technology makes it possible to integrate UWB pulse generators in a cost efficient manner and thus enabling widespread use of UWB systems. However, acquisition and synchronization of UWB signals is still an open issue, since tracking the very short UWB pulses with sufficient precision is very hard. Hence, UWB transmitter design can be easier and use less power than the narrowband transmitters, however the simple receiver design may be very challenging due to the acquisition of very narrow and low power UWB pulses.

The rich multipath propagation usually exist in UWB application scenarios, hence; a large number of echos of each transmitted pulse is received. Thus, performing explicit CIR estimation at the transceivers in order to enable matched filter (i.e. implemented using a so-called rake receiver) based signal detection and estimation, results in very complex UWB system design. Alternatively, non-coherent (i.e energy detector) simpler methods without any need of CIR estimation detection schemes are studied [16]. However, noncoherent detection schemes lead to significant performance degradation as compared to the idealistic benchmark case of coherent detection methods. In order to achieve the sub-optimal performance² of UWB systems with simple receiver design many signal processing techniques have been suggested recently.

Therefore, achieving near-optimal BER performance at low SNR with low system

²The perfectly known CIR based coherent detection has optimal performance of the UWB system.

implementation complexity is of great interest today to make the deployment of UWB technology feasible in future generation wireless networks. The main goal of this thesis is to understand and show how a low-complexity UWB receiver can be designed such that it is able to cope with the challenging environment such as multiuser and narrowband interference, and non-Gaussian noise scenarios for fifth generation (5G) communication and beyond applications.

1.10 Thesis outline and contributions

The main aim of this thesis is to propose signal processing techniques to counter UWB systems impairments, and analyze their outcomes to enhance the coverage and quality of service in UWB wireless communication. The contribution of this thesis include;

1) To make the UWB systems more robust in the presence of non-Gaussian noise, UWB signal cluster sparsity characteristics are used to mitigate the non-Gaussian³ noise in the receiver.

2) The impact of narrowband interference (NBI) on UWB systems is studied. Algorithms using NBI and UWB signal sparsity are proposed to improve system's performance.

3) To avoid high sampling Nyquist rate analog-to-digital converter (ADC) in the UWB system design, a sub-Nyquist rate based UWB receiver design have been proposed and a sub-Nyquist rate UWB system's BER, and ToA performance are analyzed.

4) By considering the massive antenna arrays (MAAs) at the receiver or fu-

³In this thesis, impulse noise (IN) and non-Gaussian noise are used interchangeable without any ambiguity.

sion center, the noncoherent detection methods are analyzed for the UWB based communication and sensor networks.

1.11 Organization of the thesis

Rest of the thesis consists of five chapters. A brief description of each chapter is as follows:

Chapter 2. Impulse Noise Mitigation in IR-UWB Communication using Signal Cluster Sparsity : In this chapter, a novel robust IR-UWB receiver design is carried out that utilizes the received UWB signal cluster sparsity characteristics to mitigate IN. The IN samples are easily detected and removed in the proposed receiver. Further, multiple UWB signal clusters (due to multipath channel), in the proposed receiver design, reduce UWB signal blanking loss as compared to the single cluster (single path channel).

Chapter 3. Sparsity-Based Narrowband Interference Mitigation in Ultra Wide- Band Communication for 5G and Beyond : In this chapter, affect of NBI on the UWB system is analyzed and a sparsity-based NBI mitigation method is proposed that exploits distinct characteristics of UWB signals and NBI. The proposed NBI mitigation algorithm does not require a non-linear operator such as limiter or blanker. Improved performance of the proposed receiver has been validated UWB signal transmission in multipath fading channels.

Chapter 4. A New Sparse Signal-Matched Measurement Matrix for Compressive Sensing in UWB Communication : To reduce the sampling rate and power requirement, UWB systems are implemented using compressive sensing or sub-Nyquist rate by exploiting the sparsity of UWB signals. In this chapter, a deterministic (partial) UWB waveform-matched measurement matrix is proposed. The proposed measurement matrix has circulant structure and is sparse in nature. The

proposed matrix is easy to implement in hardware and is operationally time efficient as needed in a practical system. Further, BER performance of the corresponding UWB system and the operational time complexity with the proposed measurement matrix are analyzed as compared to the existing measurement matrices for a sub-Nyquist rate receiver design.

Chapter 5. IR-UWB Sensor Network using Massive MIMO Decision Fu-

sion: In this chapter, UWB system for WSN using MAAs at fusion center (FC) for distributed detection is proposed and analyzed. The coherent and energy based fusion rules are analyzed for the proposed WSN over multiple access channels. The trade-off between performance and implementation complexity of the coherent and energy based fusion is studied. Further, MAAs at FC and various level of channel knowledge can enhance the performance of energy-based detector in UWB sensor network with simple system implementation and signal processing requirement. Performance of the proposed UWB sensor network with reference to probability of detection, false alarm, and error are analyzed over standard IEEE 802.15.4a multipath channels and results are validated using simulations. The impact of various design parameters such as the number of sensors, receiver antennas, sensor quality, and integration interval on the system performance is also analyzed.

Chapter 6. Conclusion and Future Work : This chapter provides a summary of the contributions made in the thesis and some suggestions for future work.

Chapter 2

Impulse Noise Mitigation in IR-UWB Communication using Signal Cluster Sparsity

In this chapter, a novel robust IR-UWB receiver design is proposed that utilizes the received UWB signal cluster sparsity characteristics to mitigate impulse noise (IN). The IN samples are easily detected and removed in the proposed receiver. Further, multiple UWB signal clusters (due to multipath channel), in the proposed receiver design, reduce UWB signal blanking loss as compared to the single cluster (single path channel). The proposed receiver's BER performance is theoretically analyzed and compared with some popular existing non-linear receivers in the presence of IN over standardized IEEE 802.15.4a channel models. The proposed robust receiver design in this chapter is useful for wideband and pulse-based communications for upcoming 5G and beyond communication networks to provide reliability, large coverage, localization and high throughput in the presence of IN.

2.1 Introduction

IR-UWB wireless communication systems are, in practice, affected by the presence of additive Gaussian noise and impulsive interference¹[30–32]. Therefore, the performance of conventional UWB receivers (correlator or matched filter), designed for additive white Gaussian noise (AWGN) scenarios, deteriorates in harsh environment such as in industries and mines due to the impulsive nature of noise and interference [33, 34].

The severe detrimental impact of IN can be mitigated using simple non-linear signal processing techniques such as clipping and blanking [30]. However, these methods are suboptimal and sensitive to the choice of a threshold [30–32]. Some methods involve IN estimation followed by subtraction from the received signal using the null carriers or training data [35]. However, since the occurrence of IN samples is random, the estimation based IN mitigation methods may not be useful in a practical system. In [36], morphological component analysis based signal separation is proposed. However, computational complexity in [36] is high due to the large size of the signal vector (due to higher sampling frequency and frame duration). Further, since IN samples have high amplitude, their effect can not be mitigated by using simple averaging techniques as in [33]. Furthermore, IN mitigation in analog domain is also suggested in [37] for orthogonal frequency division multiplexing (OFDM)-based systems. A brief introduction of the IN is described below.

2.2 IN and its modeling

IN includes the Gaussian distributed background noise and sparse high amplitude pulses. Therefore, effective noise distribution is heavy-tailed distributed i.e. non-Gaussian. The sparse high amplitude pulses are integrated with the wireless receivers and degrade the system's performance. The IN distribution at the wireless receivers depends on the sources of the noise in the operating environment. For

¹In this thesis, impulsive interference is also referred as IN, and used interchangeably.

example, in the indoor home environment, IN is generated from microwave oven, food blenders, drill machine, hairdryer, transition of electrical switches, and many more.

The parameters of IN such as pulse width, pulse arrival rate and pulse amplitude can vary for operating scenarios. Thus, various mathematical models are proposed in the literature to characterize IN such as Bernoulli-Gaussian (BG) and α -stable.

2.2.1 Bernoulli Gaussian IN

The IN denoted by $i(t)$ can be represented as [38, 39]

$$i(t) = b(t)k(t), \quad (2.1)$$

where $b(t)$ is a binary random sequence represented as $(1 - \kappa)$, $\kappa \in [0, 1]$, and $k(t)$ is Gaussian noise with mean zero and variance σ_I^2 . The combined BG IN can be modeled as

$$i(t) = (1 - \kappa) \frac{1}{\sqrt{2\pi\sigma_I^2}} \exp\{-t^2/2\sigma_I^2\}, \quad (2.2)$$

where $\kappa \in [0, 1]$. If the value of κ is 1, the transmitted signal is not affected by IN distortion during transmission. The value of parameters κ and σ_I can be used to model the duration and amplitude of IN, respectively, in the system. The IN model in (2.1) is called the BG model.

2.2.2 α -stable IN

Another useful model for IN representation is α -stable distribution. Its characteristic function $\varphi(t)$ can be written as [40]

$$\varphi(t) = \exp\{j\lambda t - \gamma|t|^\alpha[1 + j\beta\text{sign}(t)w(t, \alpha)]\}, \quad (2.3)$$

where $sign(t)$ is a signum function and

$$w(t, \alpha) = \begin{cases} \tan(\alpha\pi/2), & \text{if } \alpha \neq 1 \\ \frac{2}{\pi} \log |t|, & \text{otherwise.} \end{cases} \quad (2.4)$$

Parameters α , λ , γ , and β are exponent, location, dispersion, and symmetry parameters, respectively, of the characteristic function $\varphi(t)$. More details on α -stable noise can be found in [40]. Without loss of generality, we consider Cauchy distribution of IN with $\alpha = 1$ and $\beta = 0$, and the probability density function (PDF) given by

$$f_c(t) = \frac{1}{\pi} \left(\frac{\gamma}{\gamma^2 + (t - \lambda)^2} \right). \quad (2.5)$$

The IN generates in an ambient environment of the operating device and affects the wireless system's performance. In this thesis, BG distributions for the modeling of IN is considered.

2.3 System model

The received signal \mathbf{r} is expressed as

$$\mathbf{r} = \mathbf{s} + \mathbf{i} + \mathbf{n} \in \mathbb{R}^N, \quad (2.6)$$

where \mathbf{s} is the time hopping binary phase shift keying (TH-BPSK) modulated desired multipath UWB signal. \mathbf{i} and \mathbf{n} are IN and Gaussian (background) noise, and their distribution are given by $\mathcal{N}(0, \sigma_I^2)$ and $\mathcal{N}(0, \sigma_n^2)$, respectively. The IN \mathbf{i} models impulse interference or outliers in the system and is sparse in nature [32]. Hence, total effective noise power in the system can be written as $\sigma^2 = \sigma_n^2 + p\sigma_I^2$, where p is the probability of IN samples that occur in a given time duration and is expressed as $p = |\Upsilon_{\mathbf{i}}|/N$, $|\Upsilon_{\mathbf{i}}| \ll N$, where $\Upsilon_{\mathbf{i}} = \{k | i_k \neq 0, k = 1, 2, \dots, N\}$. The SNR, signal-to-impulse ratio (SIR), impulse-to-background noise ratio (INR), and signal-

to-impulse plus background noise ratio (SINR) are defined as $\text{SNR} = \frac{\sigma_s^2}{\sigma_n^2}$, $\text{SIR} = \frac{\sigma_s^2}{\sigma_I^2}$, $\text{INR} = \frac{\sigma_I^2}{\sigma_n^2}$ and $\text{SINR} = \frac{\sigma_s^2}{(p\sigma_I^2 + \sigma_n^2)}$, respectively, where σ_s^2 is the signal power and is considered unity, and $\sigma_I^2 \gg \sigma_n^2$. The probability density function (PDF) of the combined Gaussian and impulse noises $\mathbf{q} = \mathbf{i} + \mathbf{n}$ in the received signal in (2.6) is expressed as

$$\mathbf{q} \sim \mathcal{N}(0, \sigma_n^2) + p\mathcal{N}(0, \sigma_I^2). \quad (2.7)$$

Further, in (2.6) inter-symbol-interference is assumed to be zero [41].

2.4 Proposed receiver design

In this section, we propose a novel signal cluster-detection based receiver design to mitigate IN in a UWB system. The received UWB signal forms clusters due to its propagation characteristics [6, 31, 41, 42] and hence, is called as cluster sparse signal. The proposed cluster detection algorithm (CDA) easily differentiates between UWB signal cluster and IN using temporal characteristics of UWB signal (cluster sparsity and symmetry [6, 31, 41, 42]), and random nature of IN.

2.4.1 Cluster detection algorithm

This subsection presents a new CDA for the proposed receiver design. It is known that the UWB signal cluster is symmetric around the maximum absolute peak value of the transmitted pulse [6]. This signal cluster symmetric property can be used to differentiate between signal clusters and IN samples. Since a UWB signal is observed to be symmetric irrespective of the type of transmitted pulse, the proposed method can be used for any UWB pulse.

Let \mathcal{H}_i and \mathcal{H}_s be the two hypothesis that label samples as IN samples and desired signal samples per frame, respectively, and are expressed as

$$\begin{aligned} \mathcal{H}_i : \mathbf{r} &= \mathbf{s} + \mathbf{i} + \mathbf{n} \in \mathbb{R}^N, \\ \mathcal{H}_s : \mathbf{r} &= \mathbf{s} + \mathbf{n} \in \mathbb{R}^N. \end{aligned} \quad (2.8)$$

Further, $Pr\{\mathcal{H}_i\} = p$ and $Pr\{\mathcal{H}_s\} = 1 - p$, $p \ll 1$. The maximum absolute peak value (P_{max}^1) and the corresponding time index (I_{max}^1) are calculated from the received signal \mathbf{r} and are expressed as

$$[P_{max}^1, I_{max}^1] = \max(|\mathbf{r}|). \quad (2.9)$$

The sample $P_{max}^1 = |\mathbf{r}(I_{max}^1)|$ belongs to either \mathcal{H}_i or \mathcal{H}_s . The classification of sample $\mathbf{r}(I_{max}^1)$ is done as

$$|\mathbf{r}(I_{max}^1)| - |\mathbf{r}(I_{max}^1 + 1)| \underset{\mathcal{H}_s}{\overset{\mathcal{H}_i}{\gtrless}} \mu, \quad (2.10)$$

where μ is a constant that depends on the transmitted UWB pulse. If a sample $\mathbf{r}(I_{max}^1) \in \mathcal{H}_s$, it is concluded that no IN is present in the signal \mathbf{r} , and the peak value $P_{max}^1 = |\mathbf{r}(I_{max}^1)| \in \mathcal{H}_s$ represents center of the first signal cluster detected at this position. In this case, the signal \mathbf{r} is fed to the conventional receiver for demodulation. However, if $\mathbf{r}(I_{max}^1) \notin \mathcal{H}_s$, i.e., if $\mathbf{r}(I_{max}^1) \in \mathcal{H}_i$, then sample $\mathbf{r}(I_{max}^1)$ represents the IN sample and hence, $\mathbf{r}(I_{max}^1)$ is assigned zero value. Again, the maximum absolute peak value of the above modified signal \mathbf{r} (after assigning zero to IN sample $\mathbf{r}(I_{max}^1)$) is calculated and classified using (2.9) and (2.10), respectively. This procedure is repeated until the i^{th} maximum absolute peak valued sample $\mathbf{r}(I_{max}^i)$ of signal \mathbf{r} belongs to \mathcal{H}_s . Hence, a signal cluster is detected, and the modified signal \mathbf{r} is applied to the conventional correlator based receiver for signal demodulation. The proposed CDA is very simple and does not require multiplication or division operations. The steps (2.9) and (2.10) are repeated for pN times. The proposed CDA is summarized in **Algorithm 2**.

In **Algorithm 2**, the maximum absolute peak value P_{max}^w and the corresponding index I_{max}^w of pulse \mathbf{w} at the receiver are determined. The parameter μ is selected such that $\mu \geq |\mathbf{w}(I_{max}^w) - \mathbf{w}(I_{max}^w - 1)|$ (or $\mu \geq |\mathbf{w}(I_{max}^w) - \mathbf{w}(I_{max}^w + 1)|$ due to pulse symmetry). The values of $\mathbf{w}(I_{max}^w)$ and $\mathbf{w}(I_{max}^w \pm 1)$ are known a priori at the receiver in a UWB communication system and an appropriately low value of μ can be selected according to the above expression for good system performance. Further

in **Algorithm 2**, the mask vector $\mathbf{m}_{I_{max}^i} \in \mathbb{R}^N$ has entry ‘1’ at I_{max}^i position and ‘0’s at the remaining positions.

Algorithm 1 Cluster-Detection Algorithm (CDA)

Initialize: $\mu \geq |\mathbf{w}(I_{max}^w) - \mathbf{w}(I_{max}^w - 1)|$, $i = 1$

Input: received signal $\mathbf{r} \in \mathbb{R}^N$

Output: estimated signal $\hat{\mathbf{s}} \in \mathbb{R}^N$

Calculate: $[P_{max}^i, I_{max}^i] = \max(|\mathbf{r}|)$

While: $|\mathbf{r}(I_{max}^i)| - |\mathbf{r}(I_{max}^i + 1)| \geq \mu$

Set $\mathbf{m}_{I_{max}^i} \in \mathbb{R}^N$ vector using I_{max}^i

Update $\mathbf{r}_i = \mathbf{r}_i - \mathbf{m}_{I_{max}^i} \mathbf{r}_i$

Set $i = i + 1$

Calculate: $[P_{max}^i, I_{max}^i] = \max(|\mathbf{r}|)$

End

Update $\hat{\mathbf{s}} = \mathbf{r}$

2.4.2 False alarm and miss-detection probabilities

The probability of false alarm p_f can be calculated as

$$p_f = Pr\{(|\mathbf{r}(I_{max}^i)| - |\mathbf{r}(I_{max}^i + 1)|) \geq \mu | \mathcal{H}_s\}. \quad (2.11)$$

Let $\tilde{r}_s | \mathcal{H}_s = \mathbf{r}(I_{max}^i) - \mathbf{r}(I_{max}^i + 1) = \mathbf{s}(I_{max}^i) + \mathbf{n}(I_{max}^i) - \mathbf{s}(I_{max}^i + 1) - \mathbf{n}(I_{max}^i + 1)$, which is distributed as $\tilde{r}_s | \mathcal{H}_s \sim \mathcal{N}(0, 2((1 - \rho_s)\sigma_s^2 + \sigma_n^2))$, where ρ_s represents the correlation between two consecutive samples of signal \mathbf{s} , while noise samples are independent of each other. The p_f in (2.11) can be written as

$$p_f = \frac{1}{\sqrt{2\pi\sigma_{\tilde{r}_s}^2}} \int_{\mu}^{\infty} \exp^{-\frac{x^2}{2\sigma_{\tilde{r}_s}^2}} dx + \frac{1}{\sqrt{2\pi\sigma_{\tilde{r}_s}^2}} \int_{-\infty}^{-\mu} \exp^{-\frac{x^2}{2\sigma_{\tilde{r}_s}^2}} dx, \quad (2.12)$$

where $\sigma_{\tilde{r}_s}^2 = 2((1 - \rho_s)\sigma_s^2 + \sigma_n^2)$. Therefore, $p_f = 2Q\left(\frac{\mu}{\sqrt{2((1 - \rho_s)\sigma_s^2 + \sigma_n^2)}}\right)$. Similarly, the probability of miss-detection p_m is expressed as

$$p_m = Pr\{(|\mathbf{r}(I_{max}^i)| - |\mathbf{r}(I_{max}^i + 1)|) < \mu | \mathcal{H}_i\}. \quad (2.13)$$

Let $\tilde{r}_i|\mathcal{H}_i = \mathbf{r}(I_{max}^i) - \mathbf{r}(I_{max}^i + 1)$ and $\tilde{r}_i|\mathcal{H}_i$ is distributed as $\tilde{r}_i|\mathcal{H}_i \sim \mathcal{N}(0, 2((1 - \rho_s)\sigma_s^2 + \sigma_n^2 + \sigma_I^2))$. After some intermediate steps, p_m can be written as $p_m = 1 - 2Q\left(\frac{\mu}{\sqrt{2((1-\rho_s)\sigma_s^2 + \sigma_n^2 + \sigma_I^2)}}\right)$. The proposed IN mitigation method selects the parameter μ based on the transmitted UWB pulse design, which is standardized by FCC. Further, the proposed method does not rely on selection of optimal threshold unlike clipper and blanking receiver [30–32], thereby making it robust and versatile in a practical environment.

2.4.3 BER performance

In this subsection, the BER performance of the proposed receiver is analyzed. Let $\hat{\mathbf{s}}$ be the output of the CDA. The signal $\hat{\mathbf{s}}$ includes the background Gaussian noise and hence, $\|\hat{\mathbf{s}} - \mathbf{s}\|_2 \geq 0$. Therefore, signal $\hat{\mathbf{s}}$ can be written as $\hat{\mathbf{s}} = \mathbf{s} + \mathbf{e}$, where \mathbf{e} is the undesired (noise) additive Gaussian noise in the signal $\hat{\mathbf{s}}$. The pdf of \mathbf{e} is Gaussian distributed and is given by $\mathcal{N}(0, \sigma_e^2)$. In general, $\sigma_e^2 \geq \sigma_n^2$ because a few samples of IN may appear similar in amplitude to Gaussian background noise and hence, may not have been filtered out by **Algorithm 2** and still be present in the output signal $\hat{\mathbf{s}}$. However, $Pr\{\sigma_e^2 > \sigma_n^2\} \approx 0$ for the suitable value of μ . Further, the probability of overlap of the desired signal and IN samples is also low due to the sparse nature of both \mathbf{s} and \mathbf{i} . Therefore, the probability of assigning zero value to the desired signal sample during cluster detection is almost zero. This will not lead to power deterioration of the desired signal in the proposed receiver design. However, the deterioration in the signal's power in case of signal blanking due to overlapping IN is analyzed in the next subsection.

This work considers correlation-based coherent receiver for data symbol detection. Thus, the correlator output ζ for a positive transmitted data symbol is written as

$$\zeta = \langle \mathbf{s} + \mathbf{e}, \phi \rangle, \quad (2.14)$$

where ϕ is the template signal. The template signal is generated using UWB pulse \mathbf{w} and CIR \mathbf{h} with known time hopping code as $\phi = \mathbf{h} * \mathbf{w}$. Correlator output ζ is

Gaussian distributed, i.e.,

$$\zeta \sim \mathcal{N}(\|\mathbf{w}\|_2^2 \sum_{l=0}^{L-1} |\alpha_l|^2, \|\mathbf{w}\|_2^2 \sigma_e^2 \sum_{l=0}^{L-1} |\alpha_l|^2), \quad (2.15)$$

where α_l is the channel coefficient of the l^{th} path and L is the total number of resolved paths in CIR \mathbf{h} . The bit error probability $p_{pr}(e|\mathbf{h})$ in the presence of IN for a given CIR \mathbf{h} using the proposed receiver in a TH-BPSK system is given as

$$p_{pr}(e|\mathbf{h}) = Q\left(\sqrt{\frac{(1-\rho)\|\mathbf{w}\|_2^2 \sum_{l=0}^{L-1} |\alpha_l|^2}{\sigma_e^2}}\right), \quad (2.16)$$

where $Q(\cdot)$ is the tail probability of normal Gaussian distribution and all the transmitted symbols are equally likely in (2.16). The factor ρ depends on the blanking of UWB signal samples and $\rho \rightarrow 0$ as the sparsity of UWB signal \mathbf{s} and/or multiple signal clusters (due to multipath channel) increase for a fixed sparsity level of IN. In the absence of IN ($\sigma_e^2 = \sigma_n^2, \rho = 0$), $p_{pr}(e|\mathbf{h})$ in (2.16) corresponds to the conventional TH-BPSK system and expressed as

$$p_{pr,c}(e|\mathbf{h}) = Q\left(\sqrt{\frac{\|\mathbf{w}\|_2^2 \sum_{l=0}^{L-1} |\alpha_l|^2}{\sigma_n^2}}\right). \quad (2.17)$$

The $p_{pr,c}(e|\mathbf{h}) \leq p_{pr}(e|\mathbf{h})$ and $p_{pr,c}(e|\mathbf{h})$ can be considered as the lower bound of BER for the proposed receiver in the presence of IN. For the AWGN channel, (2.16) is expressed as

$$p_{pr}(e) = Q\left(\sqrt{\frac{(1-\rho)\|\mathbf{w}\|_2^2}{\sigma_e^2}}\right). \quad (2.18)$$

2.4.4 UWB signal and IN samples overlap

In this subsection, the effect of overlapping IN sample on UWB signal is analyzed for the proposed CDA based receiver. The number of samples Ω in a frame duration T_f at the sampling frequency F_s can be expressed as $\Omega = \lceil T_f \times F_s \rceil$, where $\lceil(\cdot)\rceil$ represents a ceiling of (\cdot) . The total number of samples of the desired UWB signal

and IN in a frame duration is written as $\Omega_s = \lceil L\Omega_w \rceil$ and $\Omega_i = \lceil p\Omega \rceil$, respectively, where Ω_w is the non-zero samples in the UWB pulse \mathbf{w} . Due to the temporal sparse nature of UWB signal and IN, $\Omega \gg \Omega_s \gg \Omega_i$ and their occupancy rate in a frame is expressed as Ω_s/Ω and Ω_i/Ω , respectively. The probability of a single IN sample occurrence in the desired UWB signal cluster's duration is written as $p_{s,i} = \tilde{\Omega}_i/\Omega_w$, where $\tilde{\Omega}_i = \Omega_i/L$, $\tilde{\Omega}_i < \Omega_w$ and $\tilde{\Omega}_i$ relative IN samples occupancy in a single UWB signal cluster. Therefore, the probability that k -number of clusters have IN is expressed as $p_{s,i,k} = \binom{L}{k} p_{s,i}^k (1 - p_{s,i})^{L-k}$, $k = 1, 2, \dots, L$, where $\binom{L}{k}$ is a binomial coefficient. Thus, the probability $p_{s,i,k}$ (k clusters have IN) reduces as k increases for fixed L and p . Hence, the desired UWB signal sample's blanking probability $p_{s,i,k}$ is small for a multipath channel as compared to an AWGN channel. Further, the desired UWB signal energy loss in a cluster $E_{s,loss,l}$, $l = 1, 2, \dots, L$ due to blanking of a signal sample in the receiver design is expressed in the range of $\|\alpha_{min} \mathbf{w}_{min}\|_2^2$ to $\|\alpha_{max} \mathbf{w}_{max}\|_2^2$, where $\alpha_{min} = \min_l \{\alpha_l\}_{l=1}^L$, $\alpha_{max} = \max_l \{\alpha_l\}_{l=1}^L$, $\mathbf{w}_{min} = \min_i \{\mathbf{w}_i\}_{i=1}^{\Omega_w}$ and $\mathbf{w}_{max} = \max_i \{\mathbf{w}_i\}_{i=1}^{\Omega_w}$. Therefore, effective signal energy loss in a frame is expressed as $E_{s,loss} = p_{s,i,k} E_{s,loss,l}$ and is smaller for a multipath channel as compared to an AWGN channel, i.e., $E_{s,loss,multipath} \leq E_{s,loss,AWGN}$ due to the low value of $p_{s,i,k}$. Intuitively, this would be true because the received signal's energy spreads in more number of low energy clusters in a multipath channel. Hence, blanking of a single UWB signal sample results in extremely low signal energy loss as compared to AWGN channel that has total energy concentration in a single cluster. Hence, the multipath channel diversity (which reduces the effective value of $p_{s,i,k}$) and the desired received UWB signal sparsity (sparsity reduces the overlapping probability of the signal and IN) add robustness against the blanking loss in the proposed UWB receiver.

2.5 Simulation results and discussion

This section presents performance of the proposed receiver as compared to the conventional receivers. Simulations are performed for the TH-BPSK UWB system for $F_s = 12$ GHz sampling frequency using the second derivative Gaussian pulse \mathbf{w} [30, 33] with the pulse width parameter $\tau = 0.4$ nanoseconds with single frame per data symbol. The transmitter and receiver synchronization is assumed with the perfect channel state information at the receiver.

In figures, legend “BPSK” represents the BER performance of the conventional receiver in the IN free system, “Theory” represents semi-analytical results using (2.16) and “BR”, “LR”, “MCA”, and “CDA” represent BER performance using the blanking [43], limiter [44], morphological component analysis (MCA) [36]² based receiver, and the proposed CDA receiver in the presence of IN, respectively. Further, “Guney, L” and “Guney, B” represent the Guney receiver [32] with limiter and blanking non-linearity, respectively, and “Myriad” represents the myriad detector [30] based receiver.

In [43], non-linear blanking receiver is analyzed for mitigating IN in an OFDM system. Here, we use it for the first time in UWB literature for IN mitigation with suitable modification and parameter selection appropriate for a UWB system. The blanking non-linearity is applied to the received signal \mathbf{r} . Samples of \mathbf{r} are assigned zero if $|\mathbf{r}_i| \geq T$, $i = 1, 2, \dots, N$, where T is a blanking threshold. To mitigate IN effect, threshold T for the blanking based receiver in UWB system is selected such that false alarm and miss-detection probabilities are minimized. The optimal value of T is derived as

$$T_{opt} = \min_T \{Pr(\mathcal{H}_s)p_{f,T} + Pr(\mathcal{H}_i)p_{m,T}\}, \quad (2.19)$$

where $p_{f,T}$ and $p_{m,T}$ are false alarm and miss detection error probabilities, respec-

²In this thesis, the separation of signal components is carried out on the basis of resonance. We use the same technique to IN and UWB signal separation.

tively, for given T . Eq. (2.19) can be written as

$$T_{opt} = \min_T \left\{ (1-p) \exp^{-\frac{T^2}{2(\sigma_s^2 + \sigma_n^2)}} + p \left(1 - \exp^{-\frac{T^2}{2(\sigma_s^2 + \sigma_n^2 + \sigma_I^2)}} \right) \right\}. \quad (2.20)$$

After some mathematical steps, T_{opt} can be given as

$$T_{opt} = \sigma_s \sqrt{2 \left(1 + \text{SIR} + \frac{1}{\text{INR}} \right) \left(1 + \frac{1}{\text{SNR}} \right) \ln \left(\frac{1-p}{p} \cdot \frac{\text{SNR} + \text{INR} + 1}{\text{SNR} + 1} \right)}. \quad (2.21)$$

For optimum threshold, p should satisfy $p \leq \frac{1+\text{SNR}+\text{INR}}{2(1+\text{SNR})+\text{INR}}$. For example, at $\text{SIR} = -30$ dB and $\text{SNR} = 20$ dB with $p = 0.01$, the optimal value of $T_{opt} \approx 4.8\sigma_s$. Further, if $\sigma_I^2 \gg \sigma_n^2$, $\sigma_I^2 \geq 10\sigma_s^2$ and $\sigma_s^2 \gg \sigma_n^2$, $T_{opt} \approx \sigma_s \sqrt{2 \ln \left(\frac{1-p}{p \cdot \text{SIR}} \right)}$. In simulations, the fixed value of T throughout the entire range of SNR is used, although SNR specific T can be selected using the SNR estimation (employing a guard band), thereby increasing the computational complexity of the receiver.

The received signal \mathbf{r} , blanking output signal \mathbf{y} (using the method in [43]) and the proposed CDA output signal $\hat{\mathbf{s}}$ are shown in Figure 2.1. Signals are plotted for five frame time duration in multipath channel model CM1 [6] in Figure 2.1. The $\text{SINR} = -40$ dB, $\text{SNR} = 20$ dB, blanking threshold $T = 4$ (for blanking receiver) and IN's probability $p = 0.01$ are considered in this simulation setup. The amplitude of IN samples is very high as observed in Figure 2.1 (at the top) and the desired signal \mathbf{s} is completely buried by IN. The high amplitude samples of IN are blanked (assigned zero value) and low amplitude samples are present at the output of blanking non-linearity as shown in Figure 2.1 (in the center). While using the proposed CDA, all the samples of IN are removed without any modification in the desired signal as observed in Figure 2.1 (at the bottom).

Next, the BER performance of TH-BPSK UWB system in the presence of IN using the proposed receiver and other receivers [30, 32, 36, 43, 45] is analyzed in multipath IEEE 802.15.4a channel CM1 (residential LOS) and CM9 (industrial NLOS) [6]. Simulation results with $\text{SIR} = -30$ dB, $p = 0.01$, $T = 2, 1$ (for blanking and limiter receiver respectively), $\mu = 0.5$, and frame duration $T_f = 100$ nanoseconds

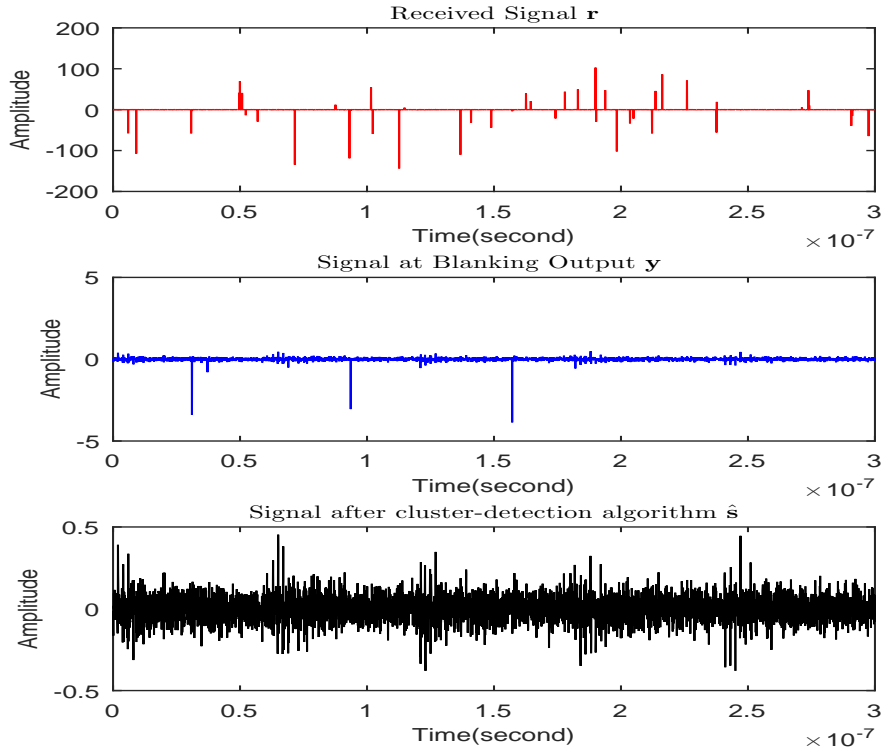


Figure 2.1: The received signal \mathbf{r} (at the top), blanking output signal \mathbf{y} and signal $\hat{\mathbf{s}}$ (at the bottom) after the proposed CDA.

(ns) are shown in Figure 3.5. The blanking and limiter based receivers exhibit bit error floor for both CM1 and CM9 channels in the presence of IN due to a fixed value of thresholds [44]. Further, blanking provides better BER performance as compared to a limiter as observed in Figure 3.5. The Guney receiver [32] with limiter (“Guney, L”) has improved BER as compared to Guney with blanking (“Guney, B”) receiver. Further, Guney (both with limiter and blanking) and Myriad [30] (“Myriad”) receivers BER performance is better in CM9 as compared to CM1 due to higher number of Rake fingers (significant energy paths). However, the MCA based receiver [36] provides better BER performance as compared to the other non-linear (Guney, blanking, limiter and Myriad) receivers. The MCA receiver [36] exhibits bit error floor due to the presence of small IN samples in the received signal after signal separation. The proposed receiver (“CDA”) has the best BER performance amongst all receivers in the presence of additive IN and is free from any bit error floor. It also overlaps with IN free system’s performance (“BPSK”) as shown in

Figure 3.5. Thus, the proposed receiver can be used in sparse IN or outliers mitigation in robust UWB receiver design where training or parameter estimation may not be possible. Also, theoretical results (using (2.16)) overlap simulation results (“CDA”) in the presence of IN at high SNR (Figure 3.5). However, at low SNR, UWB cluster’s shape is distorted, which results in theoretical and simulation results mismatch due to inaccurate blanking loss ρ estimation. BER vs SINR results in CM1 channel shown in Figure 2.3 (left) indicate best BER performance of the proposed CDA based receiver.

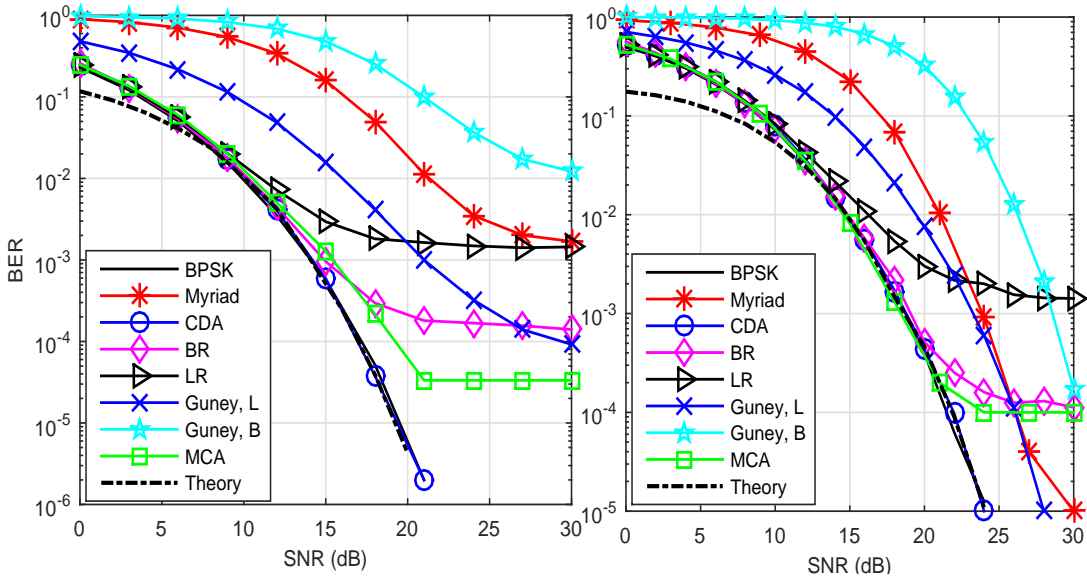


Figure 2.2: Average BER vs. SNR performance of TH-BPSK system in the presence of IN at $SIR = -30$ dB in multipath IEEE 802.15.4a channel CM1 (left) and CM9 (right) channels.

Further, the effect of overlapping IN sample on UWB signal is analyzed for the proposed CDA based receiver and results are shown in Figure 2.3 (right) for AWGN and multipath channels. In Figure 2.3 (right), $L = 10$ multipath (signal clusters), maximum ($E_{\text{loss,max}}$) and minimum ($E_{\text{loss,min}}$) UWB signal blanking loss are considered. As the UWB signal clusters increase, blanking loss decreases and is very less (19 and 46 dB less as compared to AWGN at $p = .05$ and $p = .01$, respectively, for 4 signal clusters) as compared to an AWGN channel as observed in Figure 2.3 (right). Hence, the proposed receiver is free from the UWB signal blanking loss due to multipath channel diversity.

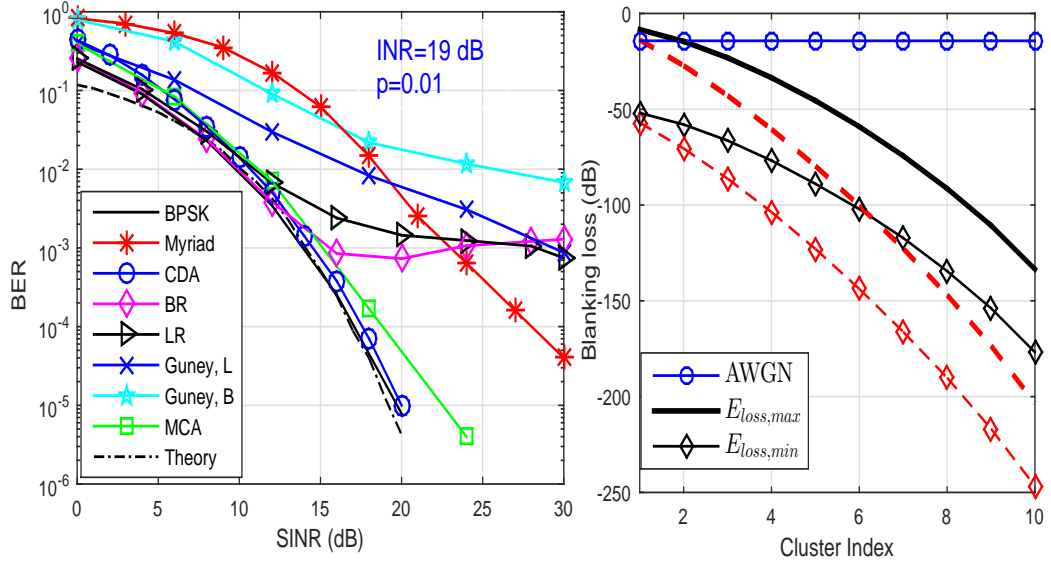


Figure 2.3: Average BER vs. SINR performance at $p = 0.01$, $INR = 19$ dB (left), and UWB signal blanking loss vs number of signal clusters (right) in \mathbf{s} at $p = 0.05$ (solid lines) and $p = 0.01$ (dashed lines).

2.6 Summary

In this chapter, a novel signal cluster sparsity based receiver design for the IN mitigation in a UWB system is proposed. The receiver exploits the deterministic cluster sparsity of the IR-UWB signal and observed to be robust and has improved BER performance (close to the IN free system) as compared to the various existing receivers in the presence of Bernoulli-Gaussian IN for multipath channels. Further, numerical results using the proposed receiver have been validated using the semi-analytic results. The work is helpful for robust operation and analysis of UWB based devices such as WSN, IoT, vehicular-to-vehicular (V2V), and M2M that work in harsh impulsive environments.

Chapter 3

Sparsity-Based Narrowband Interference Mitigation in Ultra Wide-Band Communication for 5G and Beyond

In the previous chapter, performance of UWB communication is investigated in IN effected channel, and a cluster detection algorithm using UWB signal sparsity is proposed to mitigate the IN. Further, since low power UWB systems use very wide frequency range from 3 ~ 10 GHz and overlap with various narrowband communication systems such as IEEE 802.11ac standard. Thus, impact of relatively high power narrowband interferes need to be analyzed on the wideband UWB signals, and effective NBI mitigation method(s) is required to robust operation of UWB systems.

In this chapter, affect of NBI on the UWB system is analyzed and a sparsity-based NBI mitigation method is proposed that exploits distinct characteristics of UWB signals and NBI. The proposed NBI mitigation method does not require a non-linear operator such as limiter [40] or blanker [46]. Improved performance of the proposed receiver has been validated via time hopping binary phase shift keying (TH-

BPSK) UWB signal transmission in both AWGN and multipath fading channels.

3.1 Introduction

Large bandwidth UWB signals experience interference from narrowband and other radio frequency signals in some common operating frequency regions [47–50]. The transmitted power of UWB signals is limited to be within the FCC spectral mask (maximum allowed power -41.3 dBm/MHz). Thus, weak UWB signals do not create interference in the licensed narrowband communication systems. However, high power narrowband radio signals can cause severe interference to UWB signals. Narrowband signals can be considered as high amplitude sparse interferers to UWB systems in the frequency domain or as high amplitude noise in the time domain. Therefore, UWB signals may get embedded in the noise floor due to the presence of narrowband interferers and subsequently, worsen the performance of UWB systems.

The conventional matched filter-based UWB receivers perform poorly in NBI due to the non-Gaussian nature of joint additive noise and NBI process. Thus, modified UWB receivers are proposed in the literature for robust UWB receiver design in the presence of NBI. A brief summary of a few existing UWB receiver designs in the presence of NBI is provided in Table 3.1.

NBI mitigation in UWB systems is generally done by either modifying the UWB signal's pulse shape at the transmitter, or by using NBI subspace information at the receiver. However, apriori knowledge of NBI at the receiver is impractical in the unlicensed band. Another method to handle NBI in a UWB system at the receiver, is by using limiter-based methods that use a non-linear limiter before the correlator or matched filter. However, a limiter-based receiver is not optimum for the full range of SNR and requires an adaptive threshold to limit the incoming signal amplitude. Frequency domain-based NBI mitigation techniques require whole UWB spectrum sensing and more hardware to implement multiple filters (either bandpass or notch type or both) and ADCs. Frequency domain based NBI mitigation techniques also

Table 3.1: Literature review on NBI mitigation methods for UWB systems

Method	Method Description and Advantages	Limitations
Benzhou et al. [47]	Uses projection of the received UWB signal onto the null space of NBI. The overall signal-to-interference plus noise ratio (SINR) performance is improved.	1. Requires apriori knowledge of NBI's null space that is not feasible in practical systems.
Stephane et al. [50]	Uses notch filter. The overall receiver performance is improved.	1. Ideal notch filters desirable in this system require higher order filter implementation. Thus, implementation complexity increases.
Omid et al. [51]	Uses bandpass filters followed by limiters in the frequency domain. This is a simple and deterministic method and does not require training symbols.	1. Receiver design is complex and suffers with non-linear effects of limiter. 2. Receiver also suffers with pulse shape distortion due to multiple bandpass filters. Both these may result in deterioration of receivers performance.
Hailiang et al. [52]	Uses complex-valued adaptive notch filter and a gradient-based frequency tracking algorithm. Improved system performance is observed.	1. Ideal notch filters desirable in this system require higher order filter implementation. Thus, implementation complexity increases.
Saleh et al. [53]	Uses a compressive sensing based NBI mitigation method with varying center frequency time window. Once the location of an NBI signal in frequency domain is identified, subsequent corresponding time sample can be treated as NBI samples and dropped from the received signal. Improved system performance is observed.	1. Dropping the mixed samples of UWB and NBI signals can cause system performance degradation especially when a higher number of narrowband interferers are present in the UWB system.
Ningyu et al. [54]	Uses NBI's subspace in the measurement matrix design. Improved system performance is observed.	1. Requires apriori knowledge or estimation of NBI's subspace.
Xiantao et al. [49]	Uses pre-rake/post-rake UWB transceiver design to counteract NBI. Significantly eliminates the adverse effect of narrowband interference.	1. The process is complex and requires pilot signaling.
Zhimeng et al. [48]	Uses a nonlinear Teager-Kaiser operator (TKO) and a highpass filter. NBI is assumed to be present due to an IEEE802.11a system. Improved system performance is observed.	1. This approach may not be suitable for other NBI signal and pulse shape distortion during UWB channel transmission.
Mohamed et al. [55]	Uses an adaptive method to mitigate NBI in a UWB system. Improved BER performance is observed.	1. Method requires multiple bandpass filters, ADC, and spectrum sensing for the whole range of UWB signal.
Zhiquan et al. [56]	Uses chirp waveforms and orthogonal complementary codes (OCCs). The system complexity is shifted to the transmitter side. There is an improvement of 2 to 3 dB in BER performance.	1. Requires advance information about NBI that is not feasible in practical systems.

suffer from spectral leakage. Another disadvantage of frequency domain NBI palliate schemes is that they use multiple bandpass filters and thus, UWB pulse amplitude and shape can change resulting in the degradation of receiver's performance [57].

Another issue with NBI is that, the NBI can be non-stationary in nature. Therefore, adaptive and efficient NBI mitigation techniques are required for an UWB system that do not distort UWB signal characteristics. In this chapter, we propose a new NBI mitigation method for a UWB system that exploits the sparsity structure of the composite (UWB+NBI) received signal. The proposed NBI mitigation method uses sparsity-based signal separation technique to remove NBI prior to the use of correlator or matched filter. The proposed method performs satisfactorily in both low-to-moderate NBI scenarios. The proposed receiver design does not require any apriori information about NBI subspace, which makes the proposed UWB receiver robust to current and future interference from unknown sources. Sparsity-based signal separation algorithm at the receiver can be implemented for either frame duration for highly non-stationary radio interferer or for complete data burst duration in quasi-stationary radio interferer environments. The proposed NBI mitigation method is effective for both stationary and non-stationary NBI signals.

3.2 System model

In a UWB system, every data symbol is transmitted over N_f consecutive frames to limit the transmitted signal power within the FCC spectral mask. The combined signal $w_c(t)$ of N_f frames using UWB pulse $w(t)$ of duration T_w is represented as

$$w_c(t) = \sum_{j=0}^{N_f-1} \sqrt{E_w} w(t - jT_f - c_j T_c), \quad (3.1)$$

where T_f , T_c , and E_w are the frame duration, chip duration, and pulse energy, respectively. Pulse energy is calculated using $E_w = \int_{-T_f/2}^{T_f/2} w^2(t) dt$ and is constant over a frame. $\{c_j\}$ is the pseudo random time hopping code with a time period N_p and cardinality of N_h for smoothing the transmitted signal PSD. The k^{th} transmitted

data symbol of TH-BPSK UWB signal can be written as

$$s(t) = \sum_{k=0}^{\infty} d(k)w_c(t - kT_s), \quad (3.2)$$

where $d(k) \in \{-1, 1\}$ is the data symbol and $T_s = N_f T_f$ is the data symbol duration.

The received signal $r(t)$ can be written as [56]

$$r(t) = s(t) * h(t) + i_{\text{nbi}}(t) + n(t) = \sum_{l=0}^{L-1} \alpha_l s(t - \tau_l) + i_{\text{nbi}}(t) + n(t), \quad (3.3)$$

where $*$ is the convolution operator, $h(t)$ is the CIR with L -number of resolved multipaths and expressed as $h(t) = \sum_{l=0}^{L-1} \alpha_l \delta(t - \tau_l)$, where α_l and τ_l are the gain and time delay of l^{th} multipath, respectively. The received signal $r(t)$ in (4.3) represents the weighted summation of time shifted transmitted signal $s(t)$ in the presence of AWGN $n(t)$ of zero mean and σ_n^2 variance, and NBI $i_{\text{nbi}}(t)$. The desired signal $s_r(t) = \sum_{l=0}^{L-1} \alpha_l s(t - \tau_l)$ in (4.3) is sparse in nature due to $\tau_l \geq T_w, \forall l$.

The NBI $i_{\text{nbi}}(t)$, occupies very less bandwidth as compared to UWB signals and can be considered as summation of multiple tone interferers in the frequency domain and can be considered as sparse in nature. The m^{th} narrowband interferer $i_m(t)$ can be written as

$$i_m(t) = \sqrt{2P_m} \cos(2\pi f_m t + \theta_m), \quad m = 1, \dots, M, \quad (3.4)$$

where M is the total number of narrowband interferers. The f_m and P_m are m^{th} narrowband interferer's center frequency and power, respectively. The angle θ_m is the initial random phase of the m^{th} interferer and is uniformly distributed between $[0, 2\pi)$. In this work, we assumed that center frequency f_m of interferers are randomly chosen in the UWB signal frequency range (between 2 to 10 GHz). The composite NBI $i_{\text{nbi}}(t)$ is thus expressed as

$$i_{\text{nbi}}(t) = \sum_{m=1}^M i_m(t). \quad (3.5)$$

The variance of $i_{\text{nbi}}(t)$ is expressed as $\sigma_i^2 = \mathbb{E}\{i_{\text{nbi}}^2(t)\} = \mathbb{E}\{(\sum_{m=1}^M i_m(t))^2\}$, where $\mathbb{E}\{\cdot\}$ is the statistical expectation operator and can be written as

$$\sigma_i^2 = \mathbb{E} \left\{ \sum_{m=1}^M (i_m(t))^2 + \sum_{m=1}^M \sum_{n=1, n \neq m}^M i_m(t) i_n(t) \right\}. \quad (3.6)$$

(3.6) can be re-written as

$$\sigma_i^2 \cong \sum_{m=1}^M P_m. \quad (3.7)$$

The signal-to-interference ratio (SIR) is expressed as $\text{SIR} = E_w / \sigma_i^2$. Therefore, value of P_m can be calculated based on the given SIR and M . In this work, NBI $i_{\text{nbi}}(t)$ as a summation of M tone signals where each tone signal has a random center frequency between 2 to 10-GHz range and each center frequency is separated by at least 1-GHz. For simplicity, we consider that $i_{\text{nbi}}(t)$ is available at the receiver, else it can be passed through a frequency flat fading channel to model NBI effect at the receiver.

The received signal $r(t)$ can be demodulated using the conventional Rake receiver. The k^{th} data symbol z_k of the Rake receiver output can be expressed as [48, 50, 56]

$$z_k = s_k + i_k + n_k, \quad (3.8)$$

where $s_k = \int_{kT_f}^{(k+1)T_f} s_r(t) s_{\text{tem}}(t) dt$ is the desired signal component,

$$i_k = \int_{kT_f}^{(k+1)T_f} i_{\text{nbi}}(t) s_{\text{tem}}(t) dt$$

corresponds to NBI, and $n_k = \int_{kT_f}^{(k+1)T_f} n(t) s_{\text{tem}}(t) dt$ is the noise component at the output of Rake receiver for the k^{th} data symbol. The signal $s_{\text{tem}}(t)$ is the template signal for correlator-based signal detection and is generated using the UWB pulse and CIR $h(t)$. In (3.8), a composite signal of L_r Rake fingers (assuming Rake has L_r fingers) is considered, where fingers' outputs can be combined using maximum ratio combining (MRC) or equal gain combiner (EGC). To determine the transmitted data symbol $d(k)$ from the k^{th} received data symbol signal, Rake output z_k is mapped

according to the following decision criterion:

$$d(k) = \begin{cases} -1, & \text{if } z_k \leq 0 \\ 1, & \text{otherwise} \end{cases} \quad (3.9)$$

3.3 Proposed NBI mitigation method using sparsity

Recently, sparse signal processing methods are increasingly being used in deconvolution, missing data estimation, signals separation, denoising, and many other problems. Since both the UWB signal and NBI signal are sparse in time and frequency domains, respectively, the proposed robust UWB communication receiver design based on signal separation method that exploits this sparsity to mitigate the impact of NBI signal in UWB transmission.

For the proposed system model, it is assumed that the transmitted signal $s(t)$, NBI signal $i_{\text{nbi}}(t)$, Gaussian noise $n(t)$, and CIR $h(t)$ can be reconstructed from signals sampled at Nyquist rate. Thus, signals $s(t)$, $i_{\text{nbi}}(t)$, $n(t)$, and $h(t)$ are denoted by vectors $\mathbf{s} = [s(0), s(1), \dots, s(N-1)]^T$, $\mathbf{i}_{\text{nbi}} = [i_{\text{nbi}}(0), i_{\text{nbi}}(1), \dots, i_{\text{nbi}}(N-1)]^T$, $\mathbf{n} = [n(0), n(1), \dots, n(N-1)]^T$ and $\mathbf{h} = [h(0), h(1), \dots, h(N-1)]^T$, where N is the total number of samples at Nyquist rate in a fixed time duration. Let the received signal \mathbf{r} in the k^{th} frame be given as

$$\mathbf{r} = \mathbf{s} + \mathbf{i}_{\text{nbi}} + \mathbf{n} \in \mathbb{R}^N. \quad (3.10)$$

The transmitted UWB signal \mathbf{s} is sparse due to few non-zero elements within a fixed time duration. Correspondingly, its sparsity can be defined as [58]

$$\text{sparsity}(\mathbf{s}) = \#\{k : s_k \neq 0, k = 1, 2, \dots, N\}, \quad (3.11)$$

where a signal is called K -sparse if it has only K number of non-zero samples with $K \ll N$ [58].

The proposed UWB receiver is shown in Figure 3.1. This receiver has an additional signal separation block that removes NBI signal before feeding the signal to the conventional matched filter structure (refer to Figure 3.1). At the receiver, MCA is applied for NBI separation.

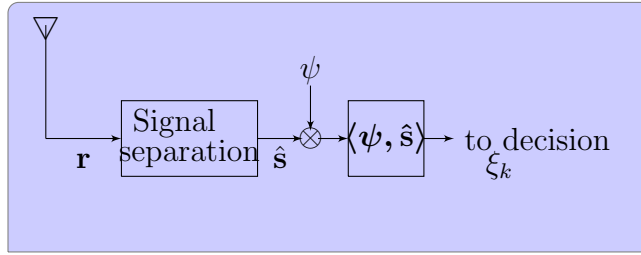


Figure 3.1: Proposed receiver structure for NBI mitigation in UWB communication system.

The MCA is a signal separation method that is generally used in image decomposition and audio decomposition. In MCA, it is assumed that the measured signal is a mixture of morphologically distinct signals that are sparse in some transform domain.

In the proposed work, resonance, duration, and oscillatory nature of UWB signals and NBI are considered to be the differentiating features for signal separation. UWB signals' amplitude and arrival time can be quasi-static (but predictable for a certain time duration) depending upon the operating environment. However, NBI always occupy a time frame due to tone nature. Without loss of generality, the UWB and NBI signals are from independent sources. Hence, statistically they are very different.

Thus, it can be noted that MCA can be used in the proposed receiver design since both the UWB signal and the NBI signal are morphologically distinct and are sparse too. The objective function for MCA optimization can be represented as [59]

$$J(\mathbf{z}_1, \mathbf{z}_2) = \|\mathbf{r} - \mathbf{A}_1\mathbf{z}_1 - \mathbf{A}_2\mathbf{z}_2\|_2^2 + \lambda_1\|\mathbf{z}_1\|_1 + \lambda_2\|\mathbf{z}_2\|_1, \quad (3.12)$$

where λ_1 and λ_2 are regularization parameters and, \mathbf{A}_1 and \mathbf{A}_2 are the sparsity basis for the desired signal and NBI, respectively. The objective function $J(\mathbf{z}_1, \mathbf{z}_2)$ is minimized with respect to \mathbf{z}_1 and \mathbf{z}_2 . Signals (signal and NBI) are estimated using MCA as

$$\hat{\mathbf{s}} = \mathbf{A}_1 \mathbf{z}_1^* \quad \text{and} \quad \hat{\mathbf{i}}_{\text{nbi}} = \mathbf{A}_2 \mathbf{z}_2^*, \quad (3.13)$$

where $(\mathbf{z}_1^*, \mathbf{z}_2^*)$ represent optimal values that minimize the cost function $J(\mathbf{z}_1, \mathbf{z}_2)$ in (3.12).

Equation (3.12) can be solved by using various algorithms such as matching pursuit (MP), basis pursuit (BP) methods, iterated soft-thresholding algorithm, and split augmented Lagrangian shrinkage algorithm (SALSA), etc. In this work, SALSA is applied because it is computationally efficient compared to MP and iterated soft-thresholding algorithms.

Moreover, SALSA is effective in separating two sparse signals (that are different in some form) from their combination [59] and is used for solving linear inverse problems, large scale non-smooth optimization with fast convergence in denoising, deconvolution, and signal separation. The procedure of solving (3.12) for NBI removal using SALSA is described in **Algorithm 2** below. Since the transmitted signal \mathbf{s} is sparse in UWB, \mathbf{A}_1 is considered to be the identity matrix. An NBI signal is a summation of sinusoidal signals and has sparse representation over DFT basis. Hence, for an NBI signal, \mathbf{A}_2 is chosen as the oversampled inverse DFT matrix.

Algorithm 2 SALSA for signal separation

Initialize: $\eta = 0.8, \mathbf{d}_1 = \mathbf{d}_2 = \mathbf{0}, \lambda_1 = 1.5, \lambda_2 = 0.5, \mathbf{A}_1, \mathbf{A}_2$
Input: $\mathbf{r}, \mathbf{z}_1, \mathbf{z}_2$
For : # of iterations=50
 $\mathbf{v}_i \leftarrow \text{soft}(\mathbf{z}_i + \mathbf{d}_i, \lambda_i/\eta) - \mathbf{d}_i, \quad i = 1, 2$
 $\mathbf{c} \leftarrow \mathbf{r} - \mathbf{A}_1 \mathbf{v}_1 - \mathbf{A}_2 \mathbf{v}_2$
 $\mathbf{d}_i \leftarrow \frac{1}{\eta+2} \mathbf{A}_i^H \mathbf{c}, \quad i = 1, 2$
 $\mathbf{z}_i \leftarrow \mathbf{d}_i + \mathbf{v}_i, \quad i = 1, 2$
End

In **Algorithm 2**, \mathbf{A}_i^H is the Hermitian transpose of \mathbf{A}_i and **soft** is a soft-

thresholding function defined as

$$\text{soft}(x, T) = \max(1 - T/|x|, 0)x. \quad (3.14)$$

In **Algorithm 2**, first the parameters λ_i , η , and vector \mathbf{d}_i are initialized. Parameters λ_i and η can be optimized based on the given signal characteristics by the user [59]. Next, we calculate vector \mathbf{v}_i using the given input signal \mathbf{z}_i and \mathbf{d}_i using parameters λ_i and η . The vector \mathbf{c} is then calculated by using the updated vector \mathbf{v}_i and the received vector. The vector \mathbf{d}_i is then updated using the values of \mathbf{c} , \mathbf{A}_i , and η . Finally, a new set of signals \mathbf{z}_i are obtained using currently estimated values of vectors \mathbf{d}_i and \mathbf{v}_i . This completes one iteration of the algorithm. In the next iteration, values are passed from previous iteration and loop runs for specified number ($\#$) of iterations. After completing $\#$ of iterations, $\mathbf{A}_1\mathbf{z}_1$ has the desired estimated signal ($\hat{\mathbf{s}}$). This separated signal $\hat{\mathbf{s}}$ is the input of the conventional correlator based receiver as shown in Figure 3.1.

The error (\mathbf{e}) between the actual transmitted signal (\mathbf{s}) and the estimated signal ($\hat{\mathbf{s}}$) after NBI signal separation from the received signal can be expressed as $\mathbf{e} = \mathbf{s} - \hat{\mathbf{s}}$. The statistical mean value ($\mu_{\mathbf{e}}$) of the error signal (\mathbf{e}) can be expressed as $\mu_{\mathbf{e}} = \mathbb{E}\{\mathbf{e}\}$. The variance ($\sigma_{\mathbf{e}}^2$) of error signal (\mathbf{e}) is calculated as

$$\sigma_{\mathbf{e}}^2 = \mathbb{E}\{\mathbf{e}^T \mathbf{e}\} = \mathbb{E}\{(\mathbf{s} - \hat{\mathbf{s}})^T (\mathbf{s} - \hat{\mathbf{s}})\}, \quad (3.15)$$

where $(\cdot)^T$ represents the transpose of (\cdot) . Further, (3.15) can be written as

$$\begin{aligned} \sigma_{\mathbf{e}}^2 &= \mathbb{E}\{\mathbf{s}^T \mathbf{s}\} - 2\mathbb{E}\{\hat{\mathbf{s}}^T \mathbf{s}\} + \mathbb{E}\{\hat{\mathbf{s}}^T \hat{\mathbf{s}}\}, \\ \sigma_{\mathbf{e}}^2 &= \mathbb{E}\{\mathbf{s}^2\} - \mathbb{E}\{\hat{\mathbf{s}}^2\}, \\ \sigma_{\mathbf{e}}^2 &= E_{\mathbf{s}} - E_{\hat{\mathbf{s}}}, \end{aligned} \quad (3.16)$$

where $E_{\mathbf{s}}$ is the transmitted signal energy and $E_{\hat{\mathbf{s}}}$ is the estimated signal (reconstructed desired signal from the received signal) energy. By assuming \mathbf{e} to be Gaus-

sian distributed, the PDF of error is expressed as $\mathbf{e} \sim \mathcal{N}(\mu_{\mathbf{e}}, \sigma_{\mathbf{e}}^2)$. In fact, the $\mu_{\mathbf{e}}$ is zero because the DC values of transmitted and reconstructed signals are generally considered to be zero. In the case of perfect estimation of the desired signal, variance $\sigma_{\mathbf{e}}^2 = 0$. Therefore, in perfect estimation, the performance of the proposed receiver is same as that of the conventional receiver without NBI.

The error signal (\mathbf{e}) with the proposed receiver structure is shown in Figure 3.2. From Figure 3.2, it is noted that the error is Gaussian distributed. The estimated pdf of error is also compared with the Gaussian pdf with mean zero and variance 1.9857×10^{-4} as shown in Figure 3.3. The error signal in Figure 3.2 is generated at SIR = 5 dB and SNR = 20 dB using the SALSA signal separation method. The value of error is close to zero for all the samples as observed from Figure 3.2 and Figure 3.3. We have also calculated the mean and variance of the error signal numerically to be equal to 2.3481×10^{-6} and 2.4823×10^{-8} , respectively. Therefore, in the presence of NBI (SIR = 5 dB), the proposed receiver has performance similar to that of a conventional receiver without any NBI. This can also be verified using the derived BER performance of the proposed receiver in (3.19). The NBI effect in Figure 3.2 is generated using the summation of four tone signals whose frequencies are selected randomly between 2 to 10 GHz. The error in Figure 3.2 has been generated using 100 noise realizations. More information about simulation environment are discussed in Section 3.4.

Next, the performance of the proposed receiver in the presence of NBI signal is analyzed. The correlator output (ξ_k) (in Figure 3.1) for the k^{th} frame using the estimated signal ($\hat{\mathbf{s}}$) can be written as

$$\begin{aligned}\xi_k &= \langle \psi, \hat{\mathbf{s}} + \mathbf{n} \rangle, \\ \xi_k &= \langle \psi, \mathbf{s} + \mathbf{e} + \mathbf{n} \rangle,\end{aligned}\tag{3.17}$$

where $\langle \cdot, \cdot \rangle$ is the inner product operator. Further, (3.17) can be written as

$$\xi_k = \sqrt{E_s} + e_k + n_k,\tag{3.18}$$

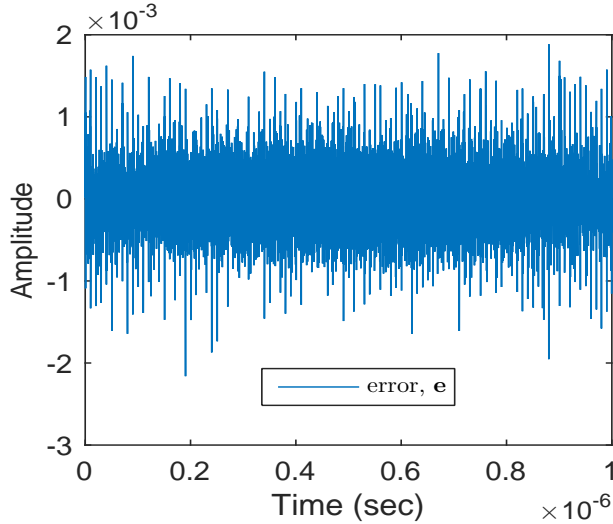
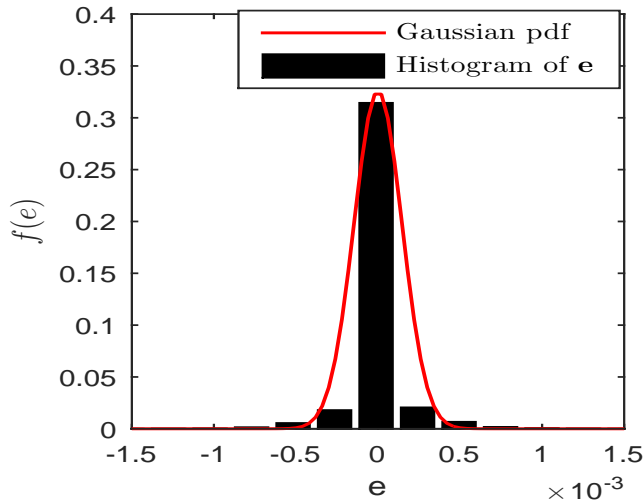

 Figure 3.2: Error signal \mathbf{e} .


Figure 3.3: Gaussian PDF and histogram of error signal.

where $\sqrt{E_s} = \langle \boldsymbol{\psi}, \mathbf{s} \rangle$ represents the correlation between the desired signal component of the received signal and the template signal $\boldsymbol{\psi}$. Symbol $\boldsymbol{\psi}$ denotes the Nyquist rate sampled version of the analog template signal $s_{tem}(t)$, $\mathbf{e}_k = \langle \boldsymbol{\psi}, \mathbf{e} \rangle$ denotes signal reconstruction error, and $\mathbf{n}_k = \langle \boldsymbol{\psi}, \mathbf{n} \rangle$ denotes AWGN noise. Assuming the desired signal (\mathbf{s}), estimation error (\mathbf{e}), and AWGN noise \mathbf{n} to be statistically independent, received signal ξ_k is Gaussian distributed with $\xi_k \sim \mathcal{N}(\sqrt{E_s}, \sigma_r^2 + \sigma_n^2)$, where σ_r^2 is the variance of e_k . The value of σ_r^2 can thus be calculated as $\sigma_r^2 = \sigma_e^2 \langle \boldsymbol{\psi}, \boldsymbol{\psi} \rangle$. Further, assuming that the estimation error is not changing from frame-to-frame and that the transmitted symbols are equally likely, BER performance of the proposed

system with TH-BPSK signal transmission in the presence of NBI is expressed as

$$p(e|\mathbf{h}) = Q\left(\sqrt{\frac{E_s}{\sigma_r^2 + \sigma_n^2}}\right), \quad (3.19)$$

where $Q(\cdot)$ is the tail probability of normal Gaussian variable. In (3.19), BER $p(e|\mathbf{h})$ is calculated for the deterministic channel. Further, in the case of perfect signal estimation using the proposed method, (3.19) is same as the BER performance of a conventional receiver without any NBI due to zero value of σ_r^2 . It is observed that at high NBI, the error can be approximated by Gaussian distribution. In totality, the performance of the proposed receiver is better than the conventional matched filter receiver. The unconditional BER $p(e)$, with TH-BPSK signal transmission is expressed as

$$p(e) = \int_{-\infty}^{\infty} p(e|\mathbf{h})f_{\mathbf{h}}(h)d\mathbf{h}, \quad (3.20)$$

where $f_{\mathbf{h}}(h)$ is the PDF of CIR \mathbf{h} . In this work, $p(e)$ is calculated using ensemble averaging over multiple channel realizations and is expressed as

$$p_{\text{ensemble}}(e) = \frac{1}{Z} \sum_{i=1}^Z p(e|\mathbf{h}_i), \quad (3.21)$$

where Z is the total number of channel realizations and \mathbf{h}_i is the i^{th} CIR realization.

3.4 Simulation and discussion

In this section, simulations are carried out in different UWB operating environment to verify effectiveness of the proposed NBI mitigation method. The transmitted pulse $w(t)$, is the second derivative Gaussian pulse [52] with $\tau = 0.2$ nanoseconds. The sampling frequency of 25 GHz, and normalized pulse transmission are considered. The spectrum of the UWB signal belongs to 2 to 10 GHz frequency range and is centered around 5 GHz. Synchronized transmitter and receiver are considered. SNR denotes the signal-to-background Gaussian noise ratio and is defined

Table 3.2: Value of parameters for TH-BPSK signal transmission

Parameter	AWGN channel	CM1 channel	CM4 channel
N_f	1	1	1
$T_f(\text{ns})$	10	60	80
$T_c(\text{ns})$	1	1	1
N_p	100	100	100
N_h	3	7	7
rms delay (ns)	-	6	24

as $\text{SNR} = E_w/\sigma_n^2$. Other simulation parameters are shown in Table 3.2. NBI is generated using the summation of four tone signals as described in equation (3.6) unless it is specified in the simulation results. The center frequency of tone signals are selected randomly between 2 to 10 GHz with 1 GHz increment. Two scenarios have been considered in the simulation set-up: AWGN and multipath communication channel with tone and non-tone narrowband interferences. BER has been considered as the performance evaluation criterion.

In Figure 3.4, BER performance with TH-BPSK UWB signal transmission in AWGN noise is shown using the conventional matched filter and the proposed receiver in the presence of NBI. In these simulations, SIR = -10, -5 dB (very large NBI), SIR = 0 dB (moderate NBI), and SIR = 10 dB (low NBI) are considered to show the effectiveness of the proposed receiver in the presence of very high to low NBI. From BER curves of Figure 3.4, it is evident that moderate to low amplitude NBI signal can be separated using SALSA algorithm. Further, it is observed that the BER performance of the proposed receiver is not much affected by low and moderate NBI cases. In fact, BER performance of the proposed receiver is close to NBI free system performance in low NBI case and is degraded by around 1.5 dB in the case of moderate NBI. The performance of the proposed receiver is free from BER floor in the presence of all the cases of NBI as is evident from Figure 3.4 due to Gaussian nature of the error. The performance of the proposed receiver is 7-20 dB better than the conventional receiver in all considered cases of NBI. Another important observation from Figure 3.4 is that the conventional matched (correlator)

receiver exhibits BER floor in the presence of very large and moderate NBI cases and hence, the performance is not suitable for any practical system.

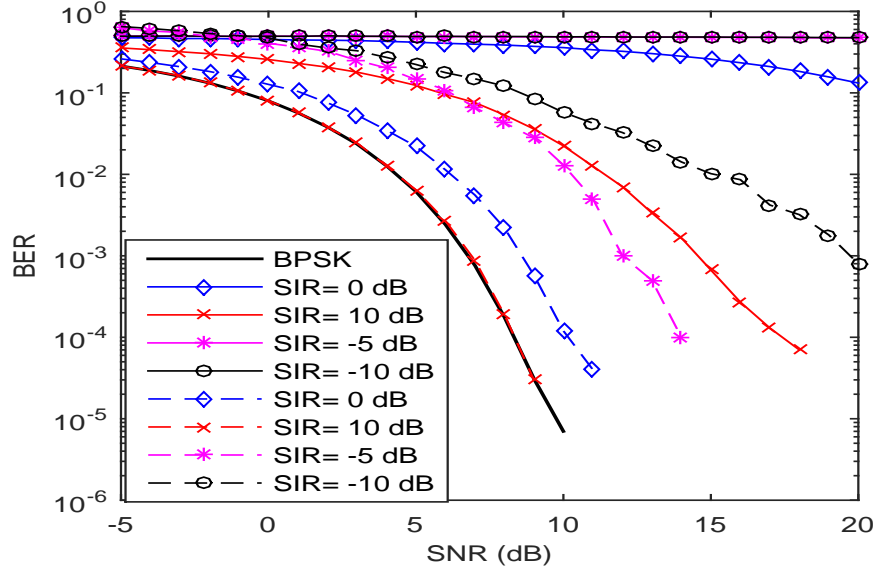


Figure 3.4: Average BER performance of TH-BPSK UWB signal in the presence of NBI using the proposed and the conventional correlator based receiver in AWGN channel. Solid (—) and dashed (---) lines represent the conventional correlator and the proposed receiver performance, respectively, and “BPSK” (thick line) represents the BER performance with TH-BPSK UWB signal transmission without any NBI.

In order to assess the performance of proposed receiver in multipath channel, BER performance of TH-BPSK modulated UWB system in CM1 channel model with additive NBI and AWGN is evaluated. CM1 is a well known line of sight (LOS) channel model for UWB communication with parameters as specified in [6]. For CM1 channel model in the presence of NBI, BER performance of the proposed and the conventional correlator receiver is shown in Figure 3.5. The proposed receiver’s performance at low NBI case (SIR = 10 dB) is similar to the conventional system performance (without NBI) as shown in Figure 3.5. However, performance of the proposed receiver is degraded by approximately 2 and 5 dB at SIR = 0 and -5 dB, respectively, compared to the conventional system (without NBI). Also, we observe from Figure 3.5 that the conventional receiver tends to error floor at high and medium NBI cases due to non-Gaussian nature of interferers. On the other hand, the proposed receiver works satisfactorily even in high NBI case as observed

in Figure 3.5. Further, filtering-based NBI [51] mitigation method has good BER performance but requires knowledge of the NBI's statistics such as frequency and bandwidth.

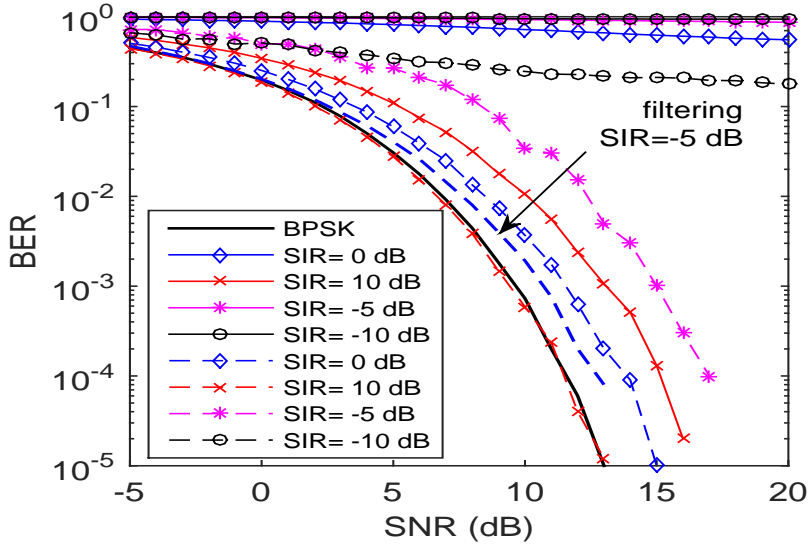


Figure 3.5: Average BER performance with TH-BPSK UWB signal transmission in the presence of NBI using the proposed and the conventional correlator based receiver in CM1 channel model. Solid (—) and dashed (---) lines represent the conventional correlator and the proposed receiver performance respectively, and “BPSK” (thick line) represents the BER performance with TH-BPSK UWB signal transmission without any NBI.

Further, robustness of the proposed receiver is verified in non-line-of-sight (NLOS) UWB communication channel model, namely, CM4 channel. The sparsity of the received UWB signal in CM4 channel model is low as compared to CM1 due to higher contribution of non-line-of-sight signal components at the receiver. The parameter specification and information about CM4 channel model can be found in [6]. BER performance of UWB system in CM4 channel model is shown in Figure 3.6 using both the proposed and the conventional receiver in the presence of NBI. BER performance of the proposed receiver in low NBI scenario (SIR = 10 dB) is same as that of the conventional receiver without any NBI. Compared to the conventional receiver, BER performance improvement of 5-20 dB is observed in CM4 channel model using the proposed receiver. This improvement depends upon NBI level. BER performance improvement in CM4 channel using the proposed receiver is degraded as compared to CM1 channel model at SIR = -5 and 0 dB due to the reduced sparsity

in the received UWB signal in CM4 channel as observed in Figure 3.6.

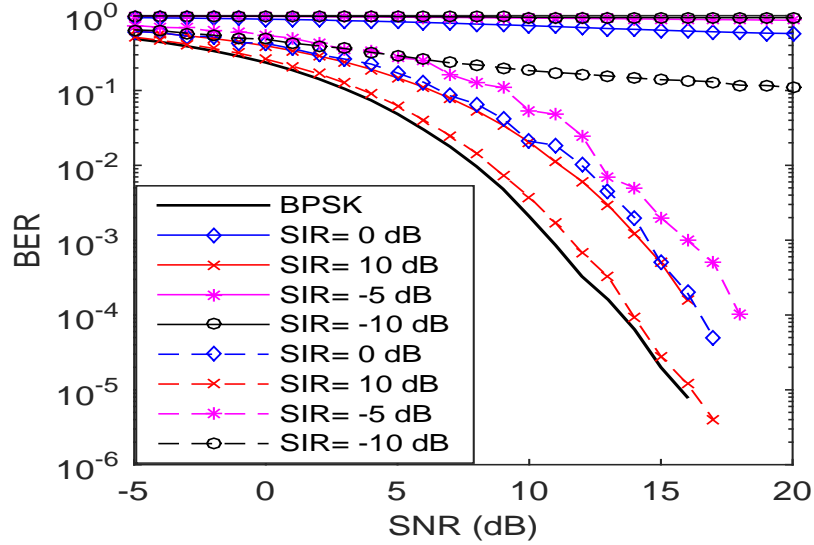


Figure 3.6: Average BER performance with TH-BPSK UWB signal transmission in the presence of NBI using the proposed and the conventional correlator based receiver in CM4 channel model. Solid (—) and dashed (---) lines represent conventional correlator and the proposed receiver performance, respectively. The “BPSK” (thick line) represents BER performance with TH-BPSK UWB signal transmission without any NBI.

Next, the effect of number of tone signals in NBI is shown with the proposed receiver design. BER performance of the proposed UWB receiver under varying number of tone signals in NBI (using (3.6)) is shown in Figure 3.7. Performance of the proposed receiver is independent of the number of tone signals in NBI as observed from Figure 3.7.

In Figure 3.8, BER performance with TH-BPSK signal transmission is shown at constant values of SNR in CM1 channel model. From Figure 3.8, one can observe that for SIR value greater than -2 dB, the proposed signal separation based receiver’s performance is almost similar to the conventional receiver without NBI. Further, effectiveness of the proposed receiver depends upon SNR level and improves as SNR increases as shown in Figure 3.8.

In order to further analyze performance of the proposed receiver, simulations are also carried out using non-tone narrowband interferer. The passband non-tone NBI has center frequency (f_c), and bandwidth $B = 20$ MHz. The center frequency is randomly selected from the range of 2 to 10 GHz with 1 GHz step increment.

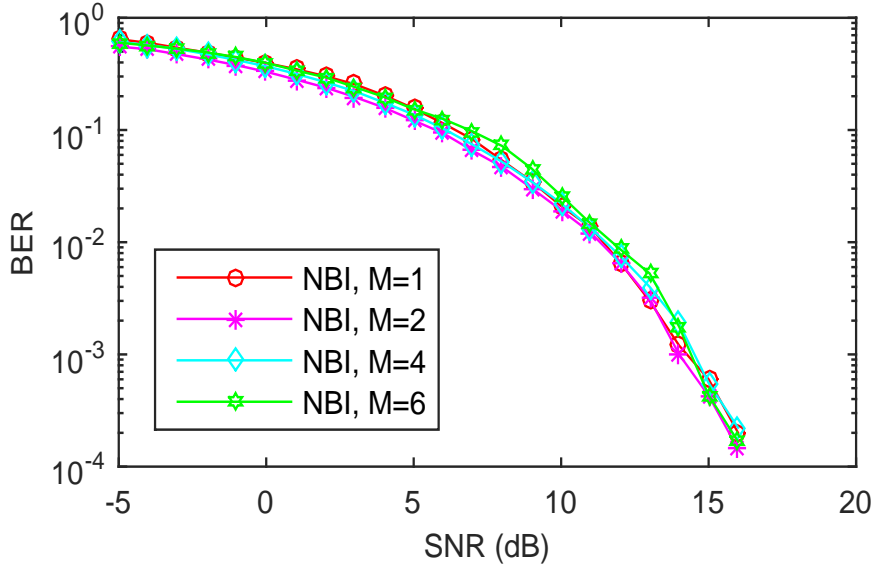


Figure 3.7: BER performance with TH-BPSK UWB signal transmission in the presence of NBI using the proposed receiver in CM1 channel model. BER curves are generated by varying number of tone signals in NBI as mentioned in (3.6) at SIR = 0 dB.

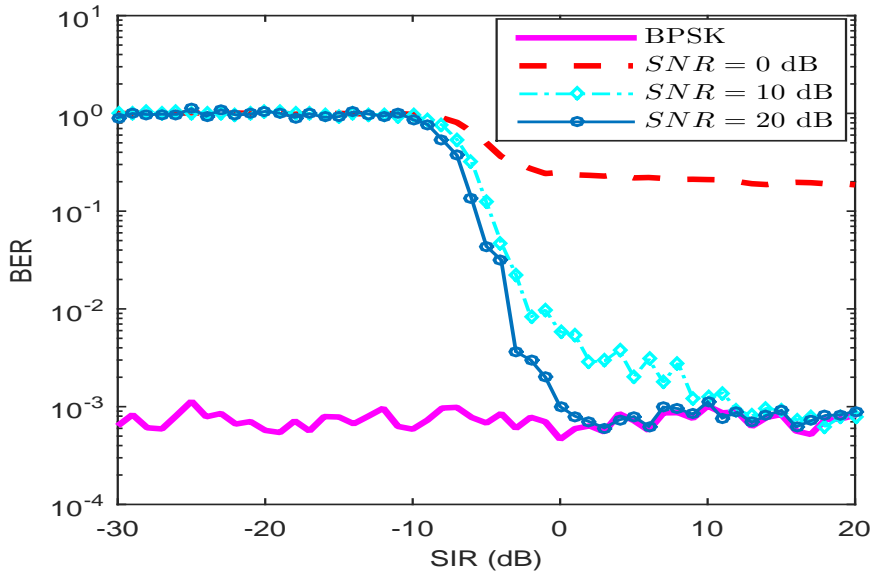


Figure 3.8: BER vs SIR performance with TH-BPSK UWB signal transmission using the proposed receiver in CM1 channel model. BER curves are generated at SNR = 0, 10, and 20 dB. The “BPSK” (solid thick line) represents system performance without any NBI at SNR = 10 dB.

NBI has triangular shape and 25% duty cycle with random pulse polarity. The autocorrelation function $\mathbf{R}_{\text{non-tone}}$ of non-tone NBI can be expressed as $\mathbf{R}_{\text{non-tone}} = \frac{\sin(\pi B \iota)}{\pi B \iota} \cos(2\pi f_c \iota)$, $\iota \in \mathbb{R}^N$. The non-tone NBI $\mathbf{i}_{\text{non-tone}}$ has flat PSD at f_c GHz over bandwidth B MHz. BER performance of the UWB system using the proposed and conventional receiver is shown in Figure 3.9 in the presence of non-tone NBI ($\mathbf{i}_{\text{non-tone}}$) using CM1 channel model. BER performance using the proposed receiver in the

presence of NBI is almost close to the conventional receiver without NBI as observed in Figure 3.9 for all considered SIRs. The conventional receiver exhibits BER floor at moderate to high NBI, while the proposed receiver is free from the BER floor for low, moderate, and very high NBI scenarios. Performance of the proposed receiver design is more effective in the presence of non-tone NBI as compared to tone NBI as observed from the above figures. Hence, in a real operating environment (non-tone NBI), the proposed receiver is able to mitigate NBI effect in a UWB system.

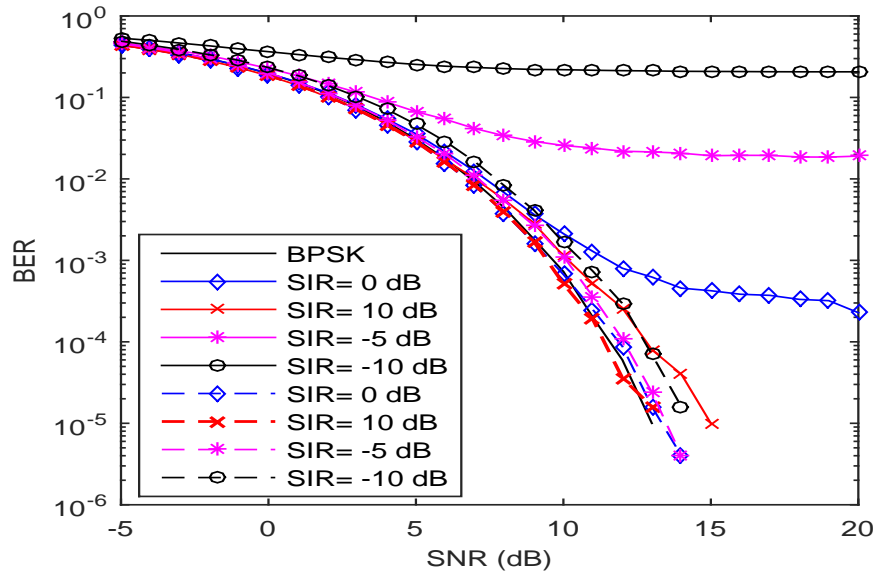


Figure 3.9: Average BER vs. SNR performance with TH-BPSK UWB signal transmission using the proposed receiver in the presence of non-tone bandpass NBI in CM1 channel model. Solid (—) and dashed (---) lines represent the conventional correlator and the proposed receiver performance, respectively. The “BPSK” (thick line) represents BER performance with TH-BPSK UWB signal transmission without any NBI.

Computational complexity of the proposed algorithm is analyzed in Table 3.3, where total number of multiplications and additions have been estimated. In Table 3.3, N is the total number of samples in the received signal vector (\mathbf{r}). Here, number of multiplications represent multiplications and divisions, and the number of additions represent additions and subtractions. This is to note that matrix multiplication consumes maximum computation time of the algorithm. In **Algorithm 2**, \mathbf{A}_1 and \mathbf{A}_2 are identity and inverse DFT matrices, respectively. Hence, the matrix multiplication can be optimized. In short, the proposed algorithm has complexity of the order of $O(N^2)$ approximately as shown in Table 3.3. Further, the total number

of additions and multiplications can be reduced using efficient implementation of the algorithm.

Table 3.3: Computational complexity of NBI mitigation

Operations	Additions	Multiplications
$\mathbf{soft}(\mathbf{x}, T)$	N	$2N$
$\mathbf{c} \leftarrow \mathbf{r} - \mathbf{A}_1 \mathbf{v}_1 - \mathbf{A}_2 \mathbf{v}_2$	$2N^2$	$2N^2$
$\mathbf{d}_i \leftarrow \frac{1}{\eta+2} \mathbf{A}_i^H \mathbf{c}$	$N(N-1)$	N^2
$\mathbf{z}_i \leftarrow \mathbf{d}_i + \mathbf{v}_i$	N	-
Total	$N + 3N^2 \approx O(N^2)$	$2N + 3N^2 \approx O(N^2)$

3.5 Summary

In this chapter, UWB communication receiver using signal separation method is proposed to mitigate the NBI. The proposed receiver is shown to perform better than the conventional matched receiver in the presence of tone and non-tone NBIs in multipath fading channels. The proposed NBI mitigation method does not require NBI's subspace information. Hence, it is free from training phase like other previous proposed methods. Also, the proposed method is not sensitive to the threshold value like in limiter based NBI mitigation methods in the UWB systems. Computational complexity of the proposed receiver design is also analyzed for UWB system in the work. The proposed receiver has a high gain of upto 5-20 dB depending upon the power of NBI as compared to the conventional receiver with a marginal increment in computational complexity. The receiver design is versatile and robust against NBI for future large bandwidth unlicensed and narrowband licensed spectrum coexisting for 5G and beyond communication systems.

Further, it is observed that the considered receiver design in this chapter is generic and can be used for different NBI models and channel conditions without any modification to the proposed receiver structure. In next generation networks, interference is a challenging problem. Therefore, the proposed receiver's performance in the presence of both the NBI and IN scenario can be explored in 5G and beyond systems.

Chapter 4

A New Sparse Signal-Matched Measurement Matrix for Compressive Sensing in UWB Communication

In the previous chapter, impact of NBI and its mitigation methods in the UWB systems were discussed. A sparsity-based NBI mitigation using signal separation method is proposed to overcome the detrimental affect of NBI in UWB communication in the last chapter. Further, UWB signal has very large bandwidth, hence the signal sampling rate is enormously high i.e. order of few GHz. A high sampling rate ADC is not available or has very high complexity and power consumption, which results in complex digital UWB system design. Therefore, low sampling rate ADC is desirable and can be achieved by exploiting the sparsity of the UWB signals using the compressive sensing (CS) method.

In this chapter, to reduce the sampling rate and for low power requirement, UWB systems are implemented using CS or sub-Nyquist rate measured samples by exploiting sparsity of the UWB signal. CS-based UWB systems are being designed in two ways: 1) signal demodulation or detection is performed in the compressive

(or compressed) sensing domain without full signal recovery at the front-end. Thus, demodulation or detection works on compressive measurements. However, system performance deteriorates in the compressive sensing domain as compared to full Nyquist rate sampling; and 2) after, Nyquist rate signal is recovered using efficient algorithms at the front-end, the signal demodulation or detection is performed using the conventional receiver. Thus, one requires an efficient compressive sensing/sampling of signal measurement at the front-end for better system performance for both the cases stated above. In this chapter, a deterministic (partial) UWB waveform-matched measurement matrix is proposed. The proposed measurement matrix has circulant structure and is sparse in nature. The proposed matrix is easy to implement in hardware and is operationally time efficient as needed in a practical system. Further, BER performance of the corresponding UWB system and the operational time complexity with the proposed measurement matrix are analyzed as compared to the existing measurement matrices in the CS domain for both the above receiver designs.

4.1 Introduction

The cost effective UWB technology is limited by requirement of a high sample rate ADC and worldwide unavailability of unique standards for millimeter wave communication. In order to handle ADC requirement, recently, channel estimation and receiver designs are being implemented using CS at sub-Nyquist rate sampling using low sampling rate ADC and low power requirement [60–69]. The sub-Nyquist rate implementation of UWB system also avoids precise synchronization requirement due to frame rate synchronization. In this context, compressive sensing with sparse signal processing can play a very important role in millimeter and 5G communication due to inherent sparse nature of signals at such high frequencies. Importance of sparse signal processing is also highlighted for efficient future 5G communication in [70].

Further, UWB signal received through the multipath channel is sparse in time domain due to short time duration of transmitted pulses and can be processed using CS for efficient system implementation [63, 67, 71]. In [64], performance of various signal recovery algorithms has been analyzed for CS based UWB system by varying the sparsity level of the received UWB signal in multipath communication environment. Results in [64] suggest that lowering the sparsity of received UWB signal culminates in higher signal recovery time and degraded performance as compared to the case of sparser signals.

In [66], CS based receiver design is proposed in high data rate transmission scheme for bursty UWB communication. It is shown that the system is insensitive to the nature of multipath channel. In [69], sparsity of UWB channel and PPM (pulse position modulation) are explored jointly and called dual sparse UWB signal for CS based UWB communication using non-coherent signal detection. However, the proposed method in [69] is valid only for PPM data transmission scheme and for high SNR region. In [68], channel estimation is done using CS based method with Gaussian pulse based signal sparsifying dictionary where signal recovery is done via MP algorithm. In [67, 71], channel estimation is done using CS and signal reconstruction error is analyzed at various sampling ratios of CS. In [67], channel estimation is done using the frequency band division of the received UWB signal. Better signal recovery is reported at sub-Nyquist rate sampling. In [71], sparsifying dictionary has been suggested using the Gaussian pulse for the received UWB signal.

Interestingly, UWB literature [61, 62] highlights signal demodulation or detection in the compressive domain at sub-Nyquist rate without full signal recovery at the front-end. Receiver design using compressive measurements is simple, needs lower power, lower sampling rate ADC, and does not require any signal processing back-end hardware for signal recovery algorithm. In [60], BPSK modulation scheme for the UWB system at 60 GHz using sub-Nyquist rate sampling is demonstrated for futuristic gigabits per second data rate. Authors in [61, 62, 72] suggest efficient system implementation in the CS domain at sub-Nyquist rates to draw signal-based

inferences such as detection, classification, and filtering. The above literature highlights the use of CS for low sampling rate ADC and less power requirement for the UWB system design. This highlights utility of CS method at millimeter wave communication for UWB signal in the near future.

In the CS literature, [73–78] various deterministic (partial) measurement matrices are proposed and analyzed. The hardware computational complexity of deterministic measurement matrices is low as compared to random Gaussian and Bernoulli distributed measurement matrices. Signal recovery from sub-Nyquist rate samples using a deterministic (partial) measurement matrix is less time consuming and computationally efficient especially in the case of Toeplitz and circulant measurement matrices without any performance degradation as compared to independent and identically distributed (i.i.d.) measurement matrices [75, 76, 79]. In [80], a fully deterministic measurement matrix is proposed and results are shown to be better compared to random measurement matrices with significant reduction in implementation complexity. In [81–84] structured measurement matrices designed using data characteristics are proposed for better system performance with or without reducing complexity and operational time of signal recovery algorithms for CS based system. In [85], wavelet measurement matrix is used with CS in image processing and is observed to provide better performance compared to the existing measurement matrices. The wavelet measurement matrix can capture local and global information of image better than other matrices; hence, improved performance is observed in [85]. Further, this work provides additional motivation to explore measurement matrix that can capture higher information rate for UWB signal in wireless communication.

UWB receiver design using compressive measurements without fully recovering the received signal can be achieved by very simple implementation. However, receivers implemented in compressive sensing domain have degraded BER performance compared to traditional analog autocorrelation receivers (ACR) [62, 63, 65, 72, 86], as highlighted in the UWB literature. On the other hand, ACRs require high sam-

pling rate ADC and long analog delay lines for implementation, which makes receiver design complex, power hungry, and technologically unimplementable in current scenario. Thus, the above discussion motivates us to use CS in UWB system by designing a good measurement matrix that can yield better BER performance.

In this chapter, the construction of a measurement matrix using the transmitted UWB waveform for efficient CS signal processing and better system performance is proposed. First, a circulant matrix is derived using the composite transmitted UWB waveform. Next, the proposed measurement matrix is generated using the random selection of rows of the above derived circulant matrix. The proposed measurement matrix designed using the transmitted UWB waveform yields better system performance in both the scenarios, *case-1*: when signal demodulation or detection is performed in the compressive domain without full signal recovery at the front-end; and *case-2*: when Nyquist rate signal is recovered first from compressive measurements using efficient signal recovery algorithms at the front end and then, signal demodulation or detection is performed using the conventional receiver. For brevity, from hereafter, we refer to *case-1* above as *sub-Nyquist rate CS receiver* implementation, and *case-2* as *signal domain based CS receiver* implementation.

In the CS and UWB literature, random Gaussian and Bernoulli distributed measurement matrices are widely used. However, random measurement matrices are difficult to implement in hardware due to randomness in the generated matrices [65, 69, 71, 72, 74, 86]. From implementation simplicity point of view, deterministic (partial) discrete cosine transform (DCT), discrete Fourier transform (DFT), Hadamard, chirp, wavelet and Reed-Muller codes based etc. measurement matrices are designed, where DCT and Hadamard matrices are widely recognized matrices in CS literature [75, 77, 78, 80, 85, 87]. A deterministic measurement matrix is formed using the random selection of rows of the corresponding matrix. In this chapter, performance of the proposed deterministic (partial) measurement matrix with the existing deterministic (partial) DCT, Hadamard and random Gaussian measurement matrices is compared.

4.2 UWB system model and receiver design in CS domain

In this section, UWB system model using TH-BPSK signal is described. Signal acquisition system for compressive measurements, and *sub-Nyquist rate CS receiver* implementation are formulated and analyzed for simple UWB communication system implementation.

4.2.1 UWB system model

In a UWB system, every data symbol is transmitted over N_f consecutive frames to limit the transmitted signal power within the FCC spectral mask. The combined signal, $w_c(t)$ of N_f consecutive frames using UWB pulse, $w(t)$ of duration T_w is represented as

$$w_c(t) = \sum_{j=0}^{N_f-1} \sqrt{E_w} w(t - jT_f - c_j T_c), \quad (4.1)$$

where T_f , T_c , and E_w are frame duration, chip duration and pulse energy, respectively. The pulse energy is calculated using $E_w = \int_{-T_f/2}^{T_f/2} w^2(t) dt$ and is constant over a frame. $\{c_j\}$ is the pseudo random time hopping code with time period N_p and cardinality N_h for smoothing the transmitted signal PSD. The k^{th} transmitted data symbol of TH-BPSK UWB signal can be written as

$$s(t) = \sum_{k=0}^{\infty} d(k) w_c(t - kT_s), \quad (4.2)$$

where $d(k) \in \{-1, 1\}$ is the data symbol and $T_s = N_f T_f$ is the data symbol duration.

The received signal $r(t)$ can be written as

$$r(t) = s(t) * h(t) + n(t) = \sum_{l=0}^{L-1} \alpha_l s(t - \tau_l) + n(t), \quad (4.3)$$

where $'*$ ' is the convolution operator, $n(t)$ is AWGN noise of zero mean and σ_n^2

variance, and $h(t)$ is the CIR with L number of resolved multipaths, expressed as $h(t) = \sum_{l=0}^{L-1} \alpha_l \delta(t - \tau_l)$, where α_l and τ_l are gain and time delay of l^{th} multipath, respectively. The received signal $r(t)$ in (4.3) represents the weighted summation of time shifted transmitted signal $s(t)$ and noise. This is to note that the signal $r(t)$ can be sparse in nature due to large multipath channel delay as compared to the transmitted UWB pulse time.

4.2.2 Signal acquisition block

In this subsection, the measurement process of received signal $r(t)$ for compressive sensing based processing is described. Let Φ be a measurement matrix (or sensing matrix) and expressed as $\Phi = [\phi_1(t) \ \phi_2(t) \ \dots \ \phi_M(t)]^T$, where $[\cdot]^T$ denotes the transpose of matrix and $\{\phi_i(t)\}_{i=1}^M$ is the i^{th} row of measurement matrix Φ . The m^{th} measurement y_m of the received signal $r(t)$ can be expressed as

$$\begin{aligned} y_m &= \langle \phi_m(t), r(t) \rangle, m = 1, 2, \dots, M \\ &= \langle \phi_m(t), \sum_{l=0}^{L-1} \alpha_l s(t - \tau_l) + n(t) \rangle \\ &= \langle \phi_m(t), s_h(t) \rangle + \langle \phi_m(t), n(t) \rangle, \end{aligned} \quad (4.4)$$

where $\langle \cdot, \cdot \rangle$ represents the inner product defined as $\langle \phi_m(t), s_h(t) \rangle = \int_{-\infty}^{\infty} \phi_m(t) s_h(t) dt$, $s_h(t) = \sum_{l=0}^{L-1} \alpha_l s(t - \tau_l)$, and measurements using (4.4) are arranged in a vector $\mathbf{y} = [y_1 \ y_2 \ y_3 \ \dots \ y_M]^T$. Measurements of the received signal are taken directly in analog domain with sub-Nyquist rate sampling and the corresponding signal acquisition system is called analog-to-information (A2I) converter [86]. The measurement vector \mathbf{y} can also be expressed as

$$\mathbf{y} = \mathbf{y}_s + \mathbf{y}_n \quad \in \mathbb{R}^M, \quad (4.5)$$

where $\mathbf{y}_s = \{\langle \phi_m(t), s_h(t) \rangle\}_{m=1}^M$ and $\mathbf{y}_n = \{\langle \phi_m(t), n(t) \rangle\}_{m=1}^M$ are desired signal and noise signal measurements, respectively. Noise \mathbf{y}_n is considered to be statistically

independent Gaussian distributed with zero mean and $\sigma_n^2 \langle \Phi, \Phi \rangle$ variance. In this work, ideal noise free measurement system with noise to be present in the received signal via channel only is assumed.

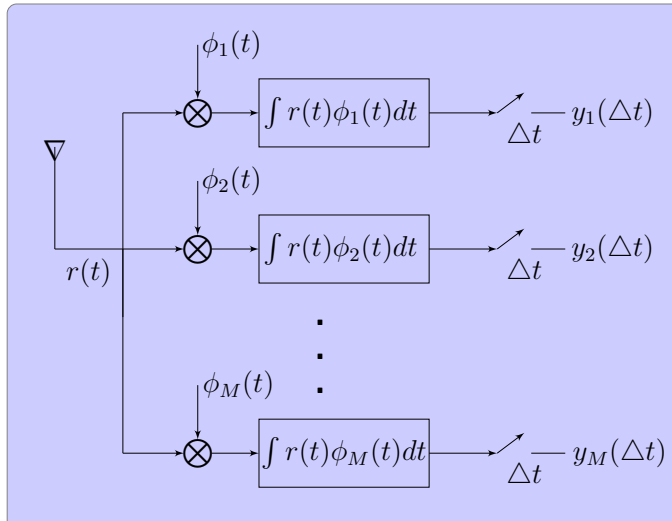


Figure 4.1: Signal acquisition block diagram.

Signal acquisition block is the front-end of the CS-based UWB receiver system and is shown in Figure 4.1. The m^{th} measurement of received signal is generated by multiplying the received signal $r(t)$ with the m^{th} row of the measurement matrix Φ , followed by a low pass filter (integrator) and a sampler. Since the measurement matrix has less number of rows compared to the conventional system, hence, output of the system is at a lower sampling rate (sub-Nyquist rate). Here, “conventional system” refers to the conventional receiver design wherein all signal samples are sensed/sampled and used in the receiver.

The signal acquisition block of Figure 4.1 is also called CS-based ADC [60]. The size of the measurement signal \mathbf{y} depends upon the number of rows in the matrix Φ . The measurement matrix Φ in Figure 4.1 can be a randomly generated or a deterministic matrix. As the number of rows in the measurement matrix increases, information about the received signal from the measurement samples improves. However, implementation complexity of A2I system also increases due to extra hardware requirement for each measurement.

4.2.3 Sub-Nyquist rate CS domain UWB receiver design

In this subsection, the CS based UWB receiver design using less complex, power efficient, and sub-Nyquist rate ADC is presented. the BER performance of TH-BPSK signal in the CS domain for multipath channel scenario is also derived. In order to derive the BER of TH-BPSK signal, discrete-time signal sampled at the Nyquist rate is considered. The received signal $r(t)$, CIR $h(t)$, UWB pulse $w(t)$, and AWGN $n(t)$ are represented by vectors as $\mathbf{r} = [r(0), r(1), \dots, r(N-1)]^T$, $\mathbf{h} = [h(0), h(1), \dots, h(N-1)]^T$, $\mathbf{w} = [w(0), w(1), \dots, w(N-1)]^T$ and $\mathbf{n} = [n(0), n(1), \dots, n(N-1)]^T$, respectively, where N is the total number of samples at Nyquist rate in a fixed time duration.

The sparsity of received signal can be observed in the transform domain and signal can be expressed as $\mathbf{r} = \Psi\mathbf{x}$ (without considering the noise), where Ψ is an $N \times N$ sparsity basis matrix and \mathbf{x} is an $N \times 1$ vector of signal coefficients in the transform domain. If \mathbf{x} has only K non-zero elements with $K \ll N$, then signal \mathbf{r} is called K -sparse in the transform domain or have sparsity of order K . Generally, received UWB signal is sparse in the time domain.

Hence, sparsity basis matrix Ψ is replaced by an identity matrix of the same size. In order to present a general theory, we have considered $\mathbf{r} = \Psi\mathbf{x} + \mathbf{n}$ (in general received signal is noisy), where \mathbf{n} is AWGN. Measurements of the received signal in (4.5) can also be written as

$$\mathbf{y} = \Phi(\mathbf{r}) = \Phi\Psi\mathbf{x} + \Phi\mathbf{n} \in \mathbb{R}^M. \quad (4.6)$$

In (4.6), Φ is the same measurement matrix as considered in (4.5) except that each row is discretized into N samples and hence, Φ has a size of $M \times N$ with $M \ll N$. Further (4.6) can be written as $\mathbf{y} = \Theta\mathbf{x} + \bar{\mathbf{n}}$, where $\Theta = \Phi\Psi$ and $\bar{\mathbf{n}} = \Phi\mathbf{n}$.

The system in (4.6) is an under-determined system of linear equations and needs some apriori knowledge to reconstruct/recover unique full signal (at Nyquist rate) \mathbf{r}

from its sub-Nyquist rate random measurements \mathbf{y} . The received sparse signal can be recovered using the ℓ_0 -norm minimization as below

$$\min \|\hat{\mathbf{x}}\|_0 \quad \text{subject to} \quad \Theta \hat{\mathbf{x}} = \mathbf{y}, \quad (4.7)$$

where $\|\hat{\mathbf{x}}\|_0$ represents the non-zero elements (sparsity of signal) in \hat{x} and defined as

$$\|\hat{\mathbf{x}}\|_0 = \#\{i : \hat{\mathbf{x}}(i) \neq 0, i = 1 \text{ to } N\}, \quad (4.8)$$

where $\#$ represents a number. The solution of underdetermined system of equations in (4.7) using ℓ_0 -norm minimization is difficult to implement because minimization of ℓ_0 -norm is NP hard [58, 74, 88]. In the literature, various solutions of (4.7) are proposed using ℓ_1 -norm minimization under convex optimization framework with less complexity that is practically realizable.

In general, received signal, \mathbf{r} is noisy. Hence, solution of (4.6) using ℓ_1 -norm can be written as

$$\hat{\mathbf{x}} = \arg \min_{\mathbf{x}} \|\mathbf{x}\|_1 : \|\Theta \mathbf{x} - \mathbf{y}\|_2 \leq \eta, \quad (4.9)$$

where η is a user defined parameter and depends upon the difference between actual \mathbf{x} and estimated $\hat{\mathbf{x}}$. Orthogonal matching pursuit (OMP) and compressive sampling matching pursuit (CoSaMP) are some of the signal recovery algorithms using ℓ_1 -norm minimization that have been used in the literature to solve (4.9) [58, 64, 69, 80].

Further in (4.6), noise \mathbf{n} in the received signal is mapped to $\bar{\mathbf{n}} = \Phi \mathbf{n}$ in the measurement signal \mathbf{y} in the compressive sensing domain. If $\Phi \Phi^T = p\mathbf{I}$, then noise observed in the CS domain is white and has variance equal to $p\sigma_n^2$, where \mathbf{I} is the identity matrix and p is a constant that depends upon the measurement matrix Φ .

The received signal corresponding to the k^{th} transmitted data symbol in the j^{th} frame in the CS framework can be written as

$$\mathbf{y}^{k,j} = \Phi \mathbf{r}^{k,j} = \mathbf{y}_s^{k,j} + \mathbf{y}_n^{k,j}, \quad (4.10)$$

where $\mathbf{y}_s^{k,j}$ and $\mathbf{y}_n^{k,j}$ are the desired signal and noise component, respectively, and can be measured using (4.5). In (4.10), it is assumed that the received UWB signal to be sparse in the time domain. If we average signal $\mathbf{y}^{k,j}$ over N_f consecutive frames by assuming channel to be invariant over one data symbol duration and noise to be affecting the desired signal similarly in each frame, then k^{th} data signal in a CS domain can be written as

$$\mathbf{y}^k = \frac{1}{N_f} \sum_{j=0}^{N_f-1} \mathbf{y}^{k,j} = \tilde{\mathbf{y}}_s^k + \tilde{\mathbf{y}}_n^k, \quad (4.11)$$

where $\tilde{\mathbf{y}}_s^k = \frac{1}{N_f} \sum_{j=0}^{N_f-1} \mathbf{y}_s^{k,j}$ and $\tilde{\mathbf{y}}_n^k = \frac{1}{N_f} \sum_{j=0}^{N_f-1} \mathbf{y}_n^{k,j}$. In (4.11), it is assumed that each data symbol has same time hopping code c_j [24, 62].

Further, if each data symbol is affected similarly by noise, then we can write $\tilde{\mathbf{y}}_n^k = \tilde{\mathbf{y}}_n$ and noise distribution in CS domain can be defined as $\tilde{\mathbf{y}}_n \sim \mathcal{N}(0, \sigma_n^2)$, where $\sigma_n^2 = \sigma_n^2 \Phi \Phi^T / N_f$. By assuming that CIR is available at the receiver and invariant over the considered data transmission duration (quasi-static over symbol duration), correlation signal template $\mathbf{y}_{tem}^k \approx \mathbf{y}_{tem}$ for correlator based signal detection scheme can be expressed as

$$\mathbf{y}_{tem} = \Phi(\mathbf{h}(t) * \mathbf{w}(t))_{t=nT_s} = \Phi(\mathbf{H}\mathbf{w}), \quad (4.12)$$

where \mathbf{H} is the channel matrix and is generated using CIR \mathbf{h} . The template signal \mathbf{y}_{tem} can also be generated using the same signal acquisition block as shown in Figure 4.1 by sending a pilot signal before data transmission. However, the template signal generated using the pilot signal is noisy, and will also result in loss of efficiency.

The correlator output in the CS domain for the k^{th} data symbol is expressed as

$$z_{cs}^k = \langle \mathbf{y}^k, \mathbf{y}_{tem} \rangle \approx \langle \tilde{\mathbf{y}}_s^k, \mathbf{y}_{tem} \rangle + \langle \tilde{\mathbf{y}}_n, \mathbf{y}_{tem} \rangle. \quad (4.13)$$

Signal $\tilde{\mathbf{y}}_s^k$ can be written as $\Phi \mathbf{H} \mathbf{w}_k$ by assuming same pulse energy in each frame, where \mathbf{w}_k is the k^{th} data symbol transmitted pulse. Further z_{cs}^k in (4.13) is expressed

as $z_{cs}^k = \mathbf{w}_k^T \mathbf{H}^T \Phi^T \Phi \mathbf{H} \mathbf{w} + \tilde{\mathbf{y}}_n^T \Phi \mathbf{H} \mathbf{w}$. The k^{th} data symbol can be demodulated using z_{cs}^k , where data symbol assignment is as given below

$$d(k) = \begin{cases} -1, & \text{if } z_{cs}^k \leq 0 \\ 1, & \text{otherwise.} \end{cases} \quad (4.14)$$

By assuming transmitted data pulse \mathbf{w}_k , measurement matrix Φ , channel matrix \mathbf{H} , and noise vector $\tilde{\mathbf{y}}_n$ to be statistically independent, the approximate distribution of signal z_{cs}^k with the positive pulse transmission is given by

$$z_{cs}^k \sim \mathcal{N}(\|\Phi \mathbf{H} \mathbf{w}\|_2^2, \sigma_n^2 \|\Phi \mathbf{H} \mathbf{w}\|_2^2). \quad (4.15)$$

Let $E_{cs} = \|\Phi \mathbf{H} \mathbf{w}\|_2^2$ be the energy of the composite multipath signal in the CS domain. The conditional BER $p_c(e|\mathbf{h})$ of TH-BPSK UWB signal using compressively sensed measurements can be written as

$$p_c(e|\mathbf{h}) = Q\left(\sqrt{\frac{E_{cs}}{\sigma_n^2}}\right). \quad (4.16)$$

In (4.16), all data symbols to be equally likely. If the matrix Φ is orthonormal, then $p_c(e|\mathbf{h})$ in (4.16) is $p(e|\mathbf{h}) = Q\left(\sqrt{N_f \frac{\|\mathbf{H} \mathbf{w}\|_2^2}{\sigma_n^2}}\right)$ and equal to the BER of a usual (uncompressed domain) TH-BPSK system. Let us define SNR as $\text{SNR} = \frac{\|\mathbf{H} \mathbf{w}\|_2^2}{\sigma_n^2}$, where $\|\mathbf{H} \mathbf{w}\|_2^2$ represents the composite multipath pulse energy in the signal domain. Assuming that the measurement matrix Φ is random and satisfies the restricted isometry property (RIP), BER in (4.16) can be expressed as [72]

$$Q\left(\sqrt{(1 + \delta_s) N_f \cdot \text{SNR}}\right) \leq p_c(e|\mathbf{h}) \leq Q\left(\sqrt{(1 - \delta_s) N_f \cdot \text{SNR}}\right), \quad (4.17)$$

where $\delta_s \in (0, 1)$ is a RIP constant. The unconditional BER $p_c(e)$ of TH-BPSK

signal can be expressed as

$$p_c(e) = \int_{-\infty}^{\infty} p_c(e|\mathbf{h}) f_{\mathbf{h}}(\mathbf{h}) d\mathbf{h}, \quad (4.18)$$

where $f_{\mathbf{h}}(h)$ is the PDF of CIR \mathbf{h} .

In this chapter, (4.18) is numerically evaluated to find the BER of TH-BPSK signal. Further, (4.18) is simplified to $Q\left(\sqrt{E_w/\sigma_n^2}\right)$ in AWGN channel with single frame per data symbol transmission scheme without any CS scheme, which is same as in [89]. The BER performance of *sub-Nyquist rate CS receiver* for TH-BPSK UWB signal using the proposed and random Gaussian measurement matrices is shown in Figure 4.2 at 30 percent of compressive sensing ratio (CSR). BER curves using simulation and (4.16) overlap considerably for both the proposed and random Gaussian matrices over the deterministic channel model as observed in Figure 4.2.

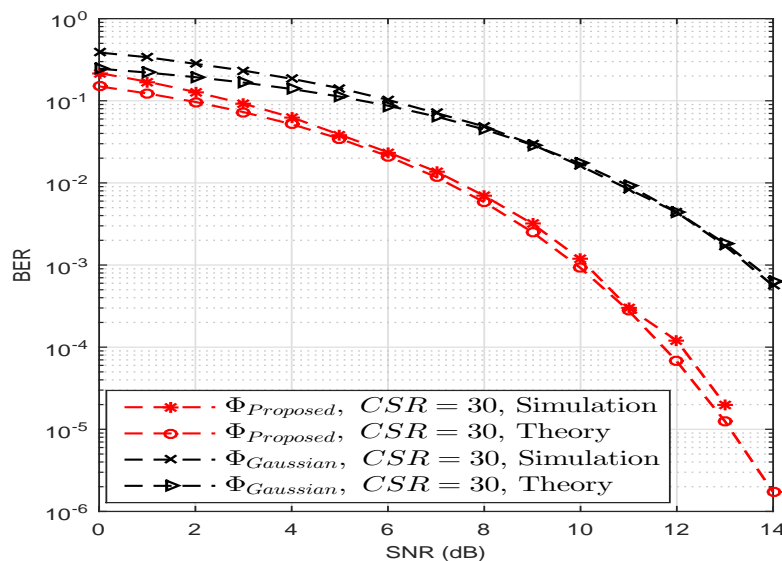


Figure 4.2: BER plot using the proposed ($\Phi_{Proposed}$) and random Gaussian ($\Phi_{Gaussian}$) measurement matrices at 30 percent CS ratio (CSR) for both simulation and theory. Theoretical results have been generated using (4.16).

4.3 Proposed measurement matrix

In this section, a new measurement matrix is proposed to process UWB signal in CS domain that provides improved performance of the UWB system in terms of

reduced operational time with efficient signal recovery. This proposed measurement matrix has circulant structure. Hence, it is computationally time efficient for signal processing in CS based system, thereby resulting in lower latency. The Toeplitz and circulant measurement matrices are also suggested earlier in the CS theory for less storage space requirement and effective signal recovery process in [73, 76, 79]. The existing Toeplitz and circulant measurement matrices in literature are formulated using the i.i.d. random distribution, hence cannot be used for improved performance in the UWB systems. In this chapter, a quasi-random circulant measurement matrix from the composite transmitted waveform is formulated. Detailed discussion of the proposed measurement matrix generation is given below.

For a given vector, $\phi = (\phi_0, \dots, \phi_{N-1})^T$, the circulant matrix can be written as

$$\Phi^\circ = \begin{bmatrix} \phi_0 & \phi_1 & \cdot & \cdot & \cdot & \phi_{N-1} \\ \phi_{N-1} & \phi_0 & \cdot & \cdot & \cdot & \phi_{N-2} \\ \cdot & \cdot & \cdot & \cdot & \cdot & \cdot \\ \cdot & \cdot & \cdot & \cdot & \cdot & \cdot \\ \cdot & \cdot & \cdot & \cdot & \cdot & \cdot \\ \phi_1 & \phi_2 & \cdot & \cdot & \cdot & \phi_0 \end{bmatrix} \in \mathbb{R}^{N \times N} \quad (4.19)$$

where Φ° is a $N \times N$ circulant matrix generated using a cyclic shift of the first row ϕ . The circulant matrix Φ° has N degrees of freedom instead of N^2 elements as compared to the other general square matrices of the same size. Therefore, the measurements taken using circulant matrix are less incoherent and subsequently, should yield poorer results with CS based recovery. However, performance of CS recovery using circulant matrix is observed to be almost similar to Gaussian or Bernoulli random matrices [76, 79]. This encourages us to use the proposed circulant matrix.

The matrix Φ° is diagonalizable and expressed as $\Phi^\circ = \mathbf{U}\mathbf{D}\mathbf{U}^H$, where H represents the Hermitian transpose, $\mathbf{U} = \sqrt{N}F_N^{-1}$, where $F_N = \exp(-2\pi ijk/N)$, $i = \sqrt{-1}$ and $j, k = 0$ to $N - 1$, and \mathbf{D} is the diagonal matrix generated using $\mathbf{D} =$

$diag(\mathbf{F}_N\phi)$, where $diag(\cdot)$ represents the diagonal element of (\cdot) . Hence, circulant matrix multiplication can be performed using fast Fourier transform (FFT) algorithm for efficient CS processing. The RIP constant of circulant matrix with random Gaussian ϕ has been derived by Holger et al. in [73] for efficient signal recovery in CS. In [73], authors also suggested RIP constant for circulant matrix when compressive sensing matrix, i.e., ϕ , is applied in the Fourier domain. Based on the discussion in [73], the proposed circulant matrix satisfies the RIP condition. In general, RIP condition is difficult to prove for any matrix [80]. Moreover, it has been reported in the literature that RIP is not a necessary condition in CS. There have been results with RIPless CS [90, 91]. Thus, it is not necessary that the proposed measurement matrix should satisfy the RIP property.

For the proposed measurement matrix, $\phi = (\sum_{p=0}^{P-1} a_p w(t - \varsigma_p))|_{t=nT_s}$ is considered to generate the circulant matrix, Φ^o , where $t = nT_s$ and $n = 0$ to $N - 1$ represents the samples at the Nyquist rate, where $\{a_p\}_{p=0}^{P-1}$ are the weighting coefficients with random values ± 1 , and $\{\varsigma_p\}_{p=0}^{P-1}$ are the pulse shifting parameters that are generated randomly. The vector ϕ represents the weighted summation of time shifted copies of the transmitted waveform. Hence, ϕ can be considered a random signal due to random nature of the coefficients $\{a_p\}_{p=0}^{P-1}$, and time shifting parameters $\{\varsigma_p\}_{p=0}^{P-1}$.

The circulant matrix Φ^o generated using ϕ ($\phi = (\sum_{p=0}^{P-1} a_p w(t - \varsigma_p))|_{t=nT_s}$) can be considered to be similar in nature to the matrix generated using random distribution of ϕ because vector ϕ has been generated via random realizations. The mean value of each column of matrix Φ^o is zero due to a random distribution of coefficients $\{a_p\}_{p=0}^{P-1}$ and zero DC value of transmitted UWB waveform.

The proposed compressive sensing measurement matrix Φ_{Proposed} generated from the matrix, Φ^o using a selection operator \mathbf{S} can be written as

$$\Phi_{\text{Proposed}} = \mathbf{S}\Phi^o, \quad (4.20)$$

where \mathbf{S} is a matrix of size $M \times N$ that selects randomly spaced M out of N rows of Φ^o where $M \ll N$. The measurement matrix Φ is fixed and same for all

measurements. Many elements of the proposed measurement matrix are zero, hence, it is sparse in nature and we name it as a “sparse sampler”.

The proposed measurement matrix has better UWB system performance with less computational time and hardware complexity requirement due to its sparse nature. The sparsity level of the proposed measurement matrix can be varied by limiting the number of summation terms in the vector ϕ . The sparsity plot of the proposed measurement matrix Φ_{Proposed} is shown in Figure 4.3 that clearly shows that Φ_{Proposed} is a sparse sampler. The proposed measurement matrix shown in Figure 4.3 has a total of 897901 elements, out of which 30549 elements are non-zero. Hence, the density of the proposed matrix is very low ($\approx 3.4\%$). The entries in the proposed measurement matrix are drawn using the UWB waveform’s value. Therefore, information capture rate in the measurement samples may be higher than the other measurement matrix for the UWB system (although it is not always guaranteed). Each column of the proposed measurement matrix is normalized to a unity norm before the measurement process. Rows of the proposed measurement matrix are observed to be almost orthogonal to each other. Thus, measurements are incoherent to each other in the CS domain.

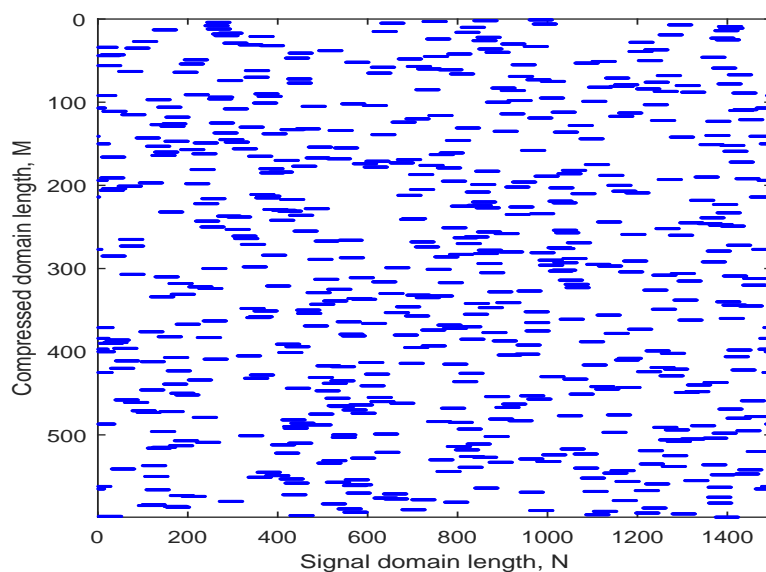


Figure 4.3: Sparsity plot of the proposed measurement matrix Φ_{Proposed} for $M = 599$ and $N = 1499$.

In this work, BER performance of TH-BPSK UWB signal has also been derived using DCT, Hadamard deterministic (partial), and random Gaussian distributed measurement matrices. Next, description of these matrices is given in brief.

4.3.1 DCT matrix

DCT matrix Φ^{DCT} is defined as

$$[\Phi^{\text{DCT}}]_{nk} = \begin{cases} \sqrt{\frac{1}{N}} & k = 0 \\ \sqrt{\frac{2}{N}} \cos \frac{\pi(2n+1)k}{2N} & 1 \leq k \leq N-1, \end{cases} \quad (4.21)$$

where $0 \leq n \leq N-1$ and N is a predefined parameter and depends upon the length of the measured signal. In simulations, N is the total number of samples of the desired signal at Nyquist rate sampling for the considered time duration. The practical implementation of Φ^{DCT} is simple and needs less memory space. DCT measurement matrix Φ_{DCT} from matrix Φ^{DCT} is generated using $\Phi_{\text{DCT}} = \mathbf{S}\Phi^{\text{DCT}}$, where \mathbf{S} is a $M \times N$ selection matrix.

4.3.2 Hadamard matrix

Hadamard measurement matrix formulation is summarized as follows. Each element in Hadamard matrix Φ^{Hadamard} has the value of ± 1 and columns (or rows) of Hadamard matrix are orthogonal to each other. Hadamard matrix of size 2^k , $2 \leq k \in \mathbb{Z}^+$ is generated using the Kronecker product between matrix Φ_2^{Hadamard} and Φ^{Hadamard} of size 2^{k-1} , and expressed as $\Phi_{2^k}^{\text{Hadamard}} = \Phi_{2^{k-1}}^{\text{Hadamard}} \otimes \Phi_2^{\text{Hadamard}}$, where \otimes is the Kronecker product sign and Φ_2^{Hadamard} is given by [87]

$$\Phi_2^{\text{Hadamard}} = \begin{bmatrix} 1 & 1 \\ 1 & -1 \end{bmatrix}. \quad (4.22)$$

The Hadamard measurement matrix Φ_{Hadamard} from Φ^{Hadamard} matrix is generated using $\Phi_{\text{Hadamard}} = \mathbf{S}\Phi^{\text{Hadamard}}$, where \mathbf{S} is a $M \times N$ selection matrix.

4.3.3 Gaussian matrix

The i.i.d. random Gaussian measurement matrix Φ_{Gaussian} is generated using Gaussian distribution of each element of matrix Φ_{Gaussian} i.e. $\phi_{mn} \sim \mathcal{N}(0, 1/M)$, $m = 1, \dots, M$, $n = 1, \dots, N$, where M and N are total rows and columns in the matrix, respectively [69, 72, 74, 80].

4.4 Simulation results and discussion

In this section, simulation results are presented on the performance of the proposed and the existing deterministic (partial) DCT, Hadamard, and random Gaussian measurement matrices. Average BER, reconstruction error, and operational time are considered as performance metrics. UWB system performance analysis is carried out for both the receiver designs- *sub-Nyquist rate CS receiver* implementation and *signal domain based CS receiver* implementation as described earlier.

Although the sparsifying basis for the UWB signal is the identity matrix, results can be extended for any sparsifying basis. To analyse UWB system's performance in the CS domain, compressive sensing ratio (CSR) is defined as $\text{CSR}[\%] = \frac{N-M}{N} \times 100$, where N and M represent the total number of samples of a signal at Nyquist and sub-Nyquist rate (CS-domain), respectively. Therefore, sub-Nyquist sampling rate is equal to $(1 - \text{CSR})$ times Nyquist rate. Samples of a signal in the CS domain are captured using the A2I conversion system shown in Figure 4.1. During the measurement time, measurement matrix Φ is kept to be same. Hence, all samples are measured in the same environment. Further, it is considered that at a time measurement samples are taken for one single frame time duration of a received signal. Accordingly, measurement process is repeated from frame to frame.

In simulation, transmitted UWB pulse \mathbf{w} is the second derivative Gaussian pulse of duration around 0.8 ns. Each data symbol is transmitted using single pulse per frame and without any frame repetition ($N_f = 1$) for simulation ease.

4.4.1 Coherence and signal reconstruction error

In this subsection, coherence and signal reconstruction error are plotted and discussed using the proposed and the existing measurement matrices.

Coherence $\mu(\Theta)$ of a matrix $\Theta = \Phi\Psi$ can be defined as [58]

$$\mu(\Theta) = \max_{i < j} \frac{|\langle \Theta_i, \Theta_j \rangle|}{\|\Theta_i\|_2 \|\Theta_j\|_2}, \quad (4.23)$$

where Θ_i and Θ_j denote columns of Θ . In Figure 4.4, coherence, $\mu(\Phi, \Psi)$ is plotted for the proposed measurement matrix Φ_{Proposed} , random Gaussian Φ_{Gaussian} , and random Bernoulli $\Phi_{\text{Bernoulli}}$ measurement matrices using inverse DCT and inverse DFT as sparsity basis Ψ . For orthonormal matrices Φ and Ψ , the coherence is $1/\sqrt{N} \leq \mu(\Phi, \Psi) \leq 1$. In Figure 4.4, $N = 1499$ and M to be ranging from 99 to 1499 are considered. Moreover, the columns of the measurement matrices are normalized to a unity norm. The coherence between the proposed measurement matrix and the sparsity basis matrix is slightly less than that between the existing measurement matrices (random Gaussian and Bernoulli measurement matrices) and the sparsity basis matrix.

In the case of DCT Ψ_{IDCT} and DFT Ψ_{IDFT} as the sparsity basis, the coherence value with the proposed matrix is higher by approximately 0.08 compared to the two existing matrices at higher values of M with $M/N > 0.3$ as observed in Figure 4.4. The higher coherence value for $M/N > 0.3$ with the proposed matrix is because of the correlation induced among the rows similar to circular and Toeplitz matrices. The Figure 4.4 indicates that measurement samples with the proposed matrix are incoherent to each other. Hence, based on Figure 4.4, one can say that measurements are incoherent using the proposed matrix, Φ_{Proposed} especially at high CSR without any loss of generality.

The normalized mean square error in signal reconstruction using the proposed measurement matrix Φ_{Proposed} and DCT Φ_{DCT} , Hadamard Φ_{Hadamard} , and random Gaussian Φ_{Gaussian} measurement matrices is shown in Figure 4.5. The normalized

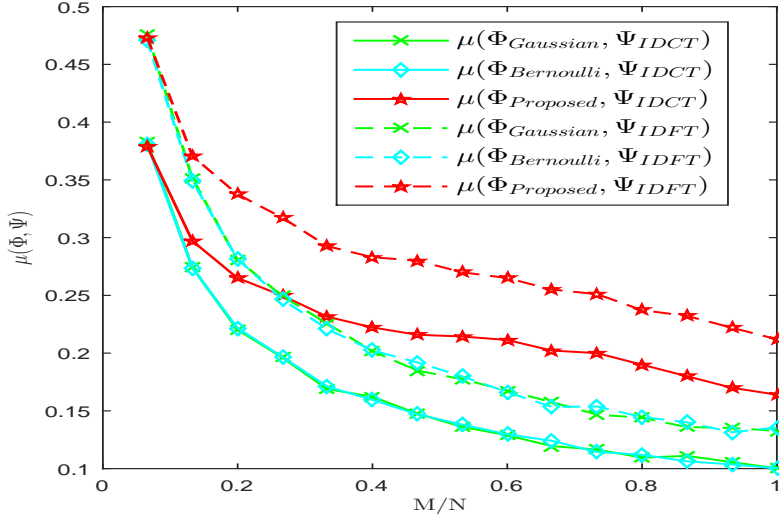


Figure 4.4: Coherence curves between the measurement matrix Φ and the sparsity matrix Ψ as a function of $\frac{M}{N}$ ratio.

mean square error (NMSE) is defined as

$$\text{NMSE} = \frac{\|\mathbf{x} - \hat{\mathbf{x}}\|_2^2}{\|\mathbf{x}\|_2^2}, \quad (4.24)$$

where \mathbf{x} is the original signal at Nyquist rate and $\hat{\mathbf{x}}$ is the reconstructed signal generated using the OMP signal recovery algorithm from the compressively sensed samples (as shown in (4.5)). In this simulation, \mathbf{x} is the received multipath UWB signal in channel model CM1 considering only ten highest amplitude multipath pulses arrived at the receiver. The normalized error using the proposed measurement matrix is smaller than the existing matrices as shown in the Figure 4.5 for both the cases with and without additive white Gaussian noise. The performance improvement with the proposed matrix is small at $SNR = \infty$ (noiseless), i.e., the performance is almost the same as other measurement matrices. However, there is a considerable improvement in performance at $SNR = 5$ dB with the proposed matrix as observed in Figure 4.5. Thus, in noisy scenario, the proposed matrix performs comparatively better. Further, it is noticed that the relative improvement in normalized error with the proposed measurement matrix decreases as M/N ratio increases. Lower improvement at the higher values of M/N ratio is due to increase

in signal information with all the matrices. Therefore, results in Figure 4.5 clearly establish the superior performance of the proposed matrix at lower CS rates as well as in noisy scenarios.

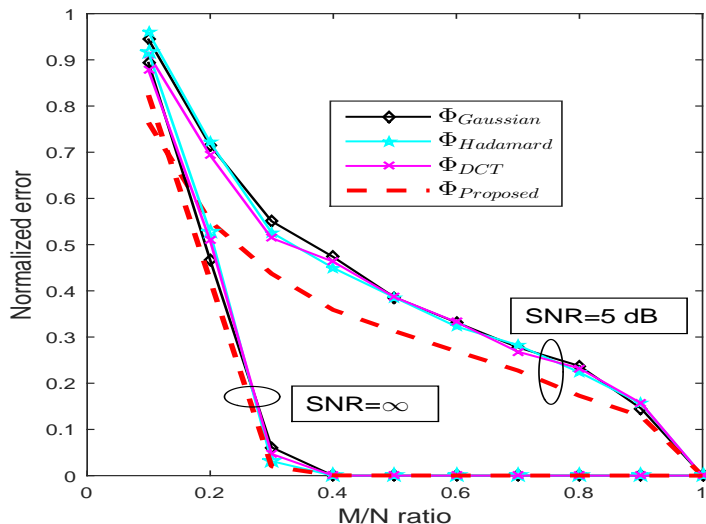


Figure 4.5: Normalized mean squared error vs M/N ratio.

4.4.2 BER performance of sub-Nyquist CS UWB receiver in multipath channel

In this subsection, average BER performance of TH-BPSK UWB signal in the CS domain by considering multipath communication environment is shown. To verify the robustness of the proposed measurement matrix for UWB signal, we have carried out simulations in both LOS and NLOS multipath channel models CM1 and CM4 with 6 and 24 nanoseconds *rms* (root mean square) delay spread, respectively. More about multipath channel models CM1, CM4 and their parameters specification can be found in [6, 24]. The system performance at three different CS ratios $CSR = 30$ (low), $CSR = 60$ (medium), and $CSR = 80$ (high) is analyzed. Further, it is assumed that all the multipaths of the received signal \mathbf{r} in the measurement process for sub-Nyquist rate samples.

The channel model CM4 with inter symbol interference (ISI) and CM1 without any ISI are considered to demonstrate the robustness of the proposed measurement

matrix with improved performance in various operating scenario. Further, it is noted that CM4 channel model is less sparse as compared to CM1 as reported in the literature [64, 68, 69, 71]. Hence, sparsity level is also different among simulation results in this subsection. The frame duration $T_f = 60$ nanoseconds is considered for both the CM1 and CM4 channel models.

Average BER performance of TH-BSPK signal is shown in Figure 4.6, Figure 4.7 and Figure 4.8 in the CS domain for both the CM1 and CM4 channel models with the proposed, DCT, Hadamard, and random Gaussian measurement matrices at $\text{CSR} = 80$, $\text{CSR} = 60$ and $\text{CSR} = 30$, respectively. The average BER performance using the proposed measurement matrix Φ_{Proposed} is 1-5 dB better than DCT Φ_{DCT} , Hadamard Φ_{Hadamard} , and random Gaussian Φ_{Gaussian} measurement matrices depending upon the values of BER and CSR as shown in Figure 4.6, Figure 4.7 and Figure 4.8. Again, improved performance with the proposed matrix is observed.

Improved BER performance of the UWB system with the proposed measurement matrix is observed as compared to other existing matrices in both CM1 and CM4 channel models (Figure 4.6, Figure 4.7 and Figure 4.8). BER performance of DCT, Hadamard, and random Gaussian measurement matrix are close in both the CM1 and CM4 channel models. The slope of the BER curves in CM4 channel model is low compared to CM1 due to ISI effect in CM4 simulation. Same trend of BER slope is followed by all measurement matrices. Therefore, results generated in this subsection help us infer that the BER improvement ($\approx 1-5$ dBs) using the proposed measurement matrix can always be observed irrespective of the system operational environment such as sparsity level and ISI effect.

4.4.3 BER performance of signal domain based CS UWB receiver in frame repetition environment

In this subsection, signal recovery and frame repetition factor N_f for the same data symbol are analyzed for BER performance using the proposed and random Gaussian measurement matrices.

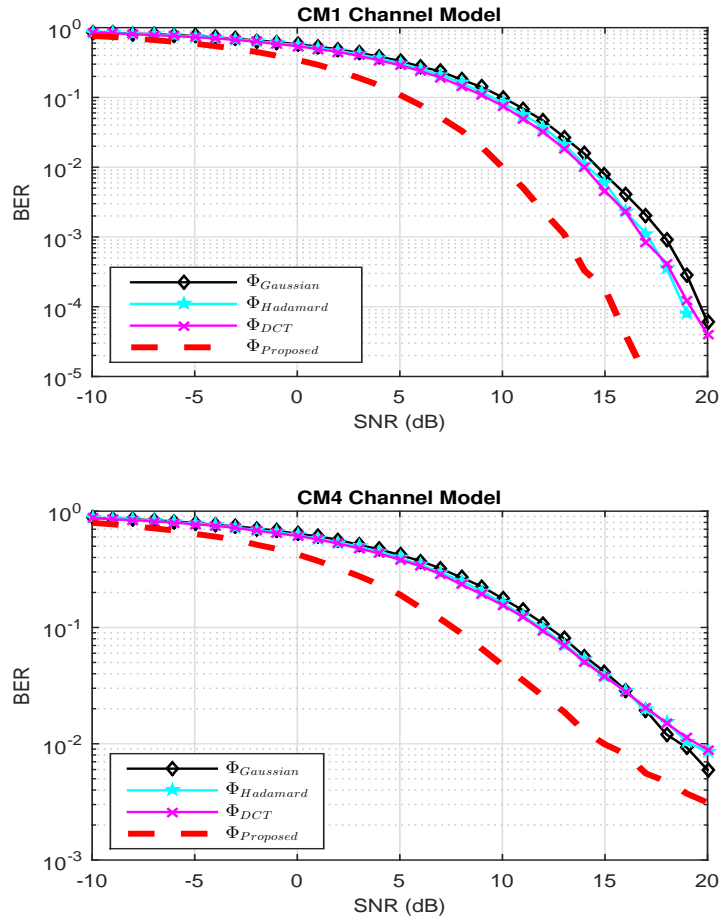


Figure 4.6: Average BER performance of TH-BSPK signal in CM1 and CM4 channel models at CSR = 80.

To demonstrate the performance of the proposed measurement matrix Φ_{Proposed} in signal recovery from the compressive measurements, the BER of TH-BPSK signal using the proposed and random Gaussian Φ_{Gaussian} matrices is shown in Figure 4.9. In this simulation, it is considered that signal received via all of the multipaths and used the OMP signal recovery algorithm. In Figure 4.9, CSR = 30 and CSR = 60 are considered in CM1 channel model with single frame per data symbol transmission. The BER performance of TH-BPSK signal using the proposed matrix is 4-5 dB better than the random Gaussian measurement matrix with the OMP signal recovery algorithm as shown in the Figure 4.9. The BER performance improvement in *signal-domain compressive sensing UWB system* is higher than the *sub-Nyquist compressive sensing UWB system* using the proposed matrix, which further estab-

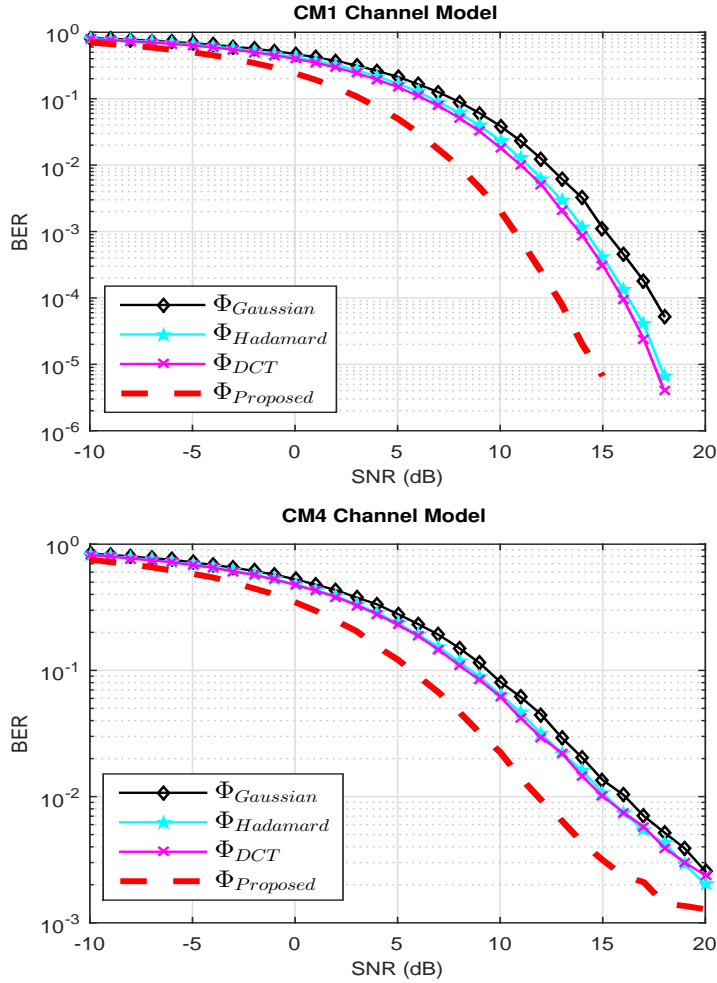


Figure 4.7: Average BER performance of TH-BSPK signal at 60 percent compressive sensing ratio in CM1 and CM4 channel models.

lishes the importance of the proposed matrix in the UWB communication. One can also notice that loss of signal information during signal recovery phase is less with the proposed matrix as compared to the random Gaussian matrix.

Further, the effect of frame repetition per data symbol N_f is also analyzed on the BER performance of TH-BPSK signal using the proposed and random Gaussian measurement matrices in the CS domain and results are shown in Figure 4.10. The BER performance improvement is almost same in both cases of $N_f = 1, 2$ using the proposed matrix as observed in Figure 4.10 at $\text{CSR} = 60$. In this simulation, the constant transmitted pulse energy E_w that is equal to that of single frame per data symbol is assumed. Therefore, average pulse energy per data symbol is E_w and noise variance is reduced by a factor of N_f as mentioned in (4.1). The improvement

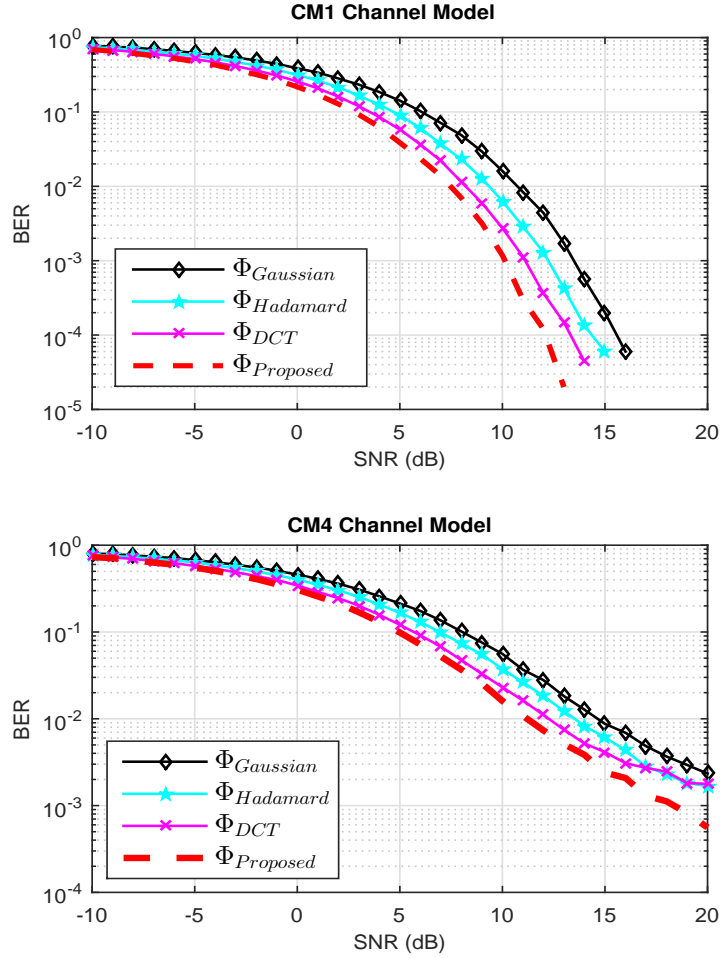


Figure 4.8: Average BER performance of TH-BSPK signal at 30 percent compressive sensing ratio in CM1 and CM4 channel models.

in BER using the frame repetition per data symbol is around $10 \log(N_f)$ and same is shown in Figure 4.10 for $N_f = 2$ with around 3 dB BER improvement. From Figure 4.10, one can conclude that relative BER improvement using the proposed measurement matrix is independent of the frame repetition factor N_f .

In Figure 4.11, BER performance comparison with and without CS using the proposed measurement matrix in channel model CM1 is shown. The BER performance improves as the compressive sensing ratio decreases and reaches close to the Nyquist rate as observed in Figure 4.11. In Figure 4.11, “BPSK” represents the conventional system performance without using compressive sensing and “ $\Phi_{Proposed}$, $CSR = 30$, Recovery” represents system performance using CS and OMP signal recovery algorithm on the compressive measurements at $CSR = 30$ in

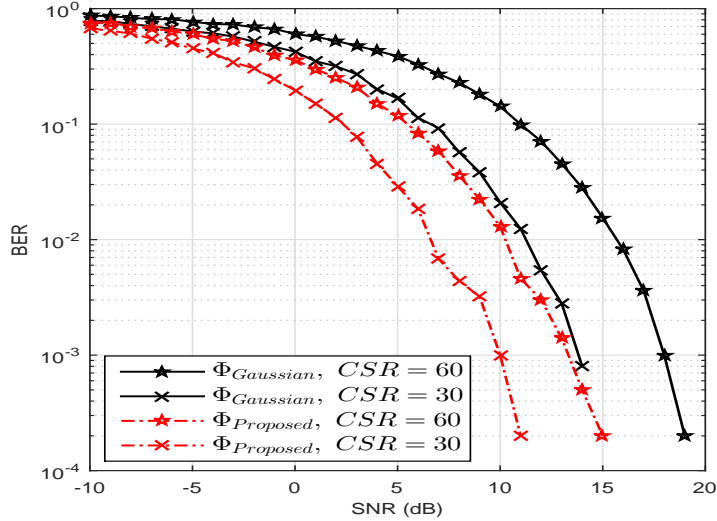


Figure 4.9: BER performance of TH-BSPK signal including the OMP signal recovery algorithm at CSR = 30 and CSR = 60 using the proposed and random Gaussian measurement matrices in CM1 channel model.

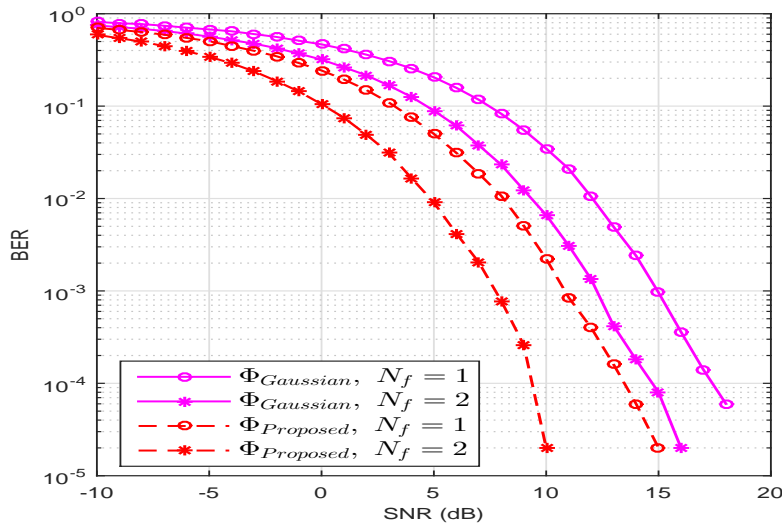


Figure 4.10: Average BER performance of TH-BSPK UWB signal in CS domain at CSR = 60 using the proposed and random Gaussian measurement matrices in CM1 channel model for $N_f = 1, 2$.

signal domain. The UWB system performance using CS with signal recovery algorithm at CSR = 30 is almost similar to the conventional system (without CS) performance as shown in In Figure 4.11. However, previous system performance is implemented at sub-Nyquist rate using the low sampling rate ADC as compared to conventional system (“BPSK”) at Nyquist rate using very high rate ADC.

Further, observe that performance in CS domain at CSR = 30 and CSR = 60

degrades by 0.5 and 1 dB at $\text{BER} = 2 \times 10^{-5}$ as compared to full Nyquist rate. Hence, the proposed measurement matrix can prove effective in implementing simple UWB system in the CS domain with low sampling rate ADC and less power requirement without significant loss in system performance.

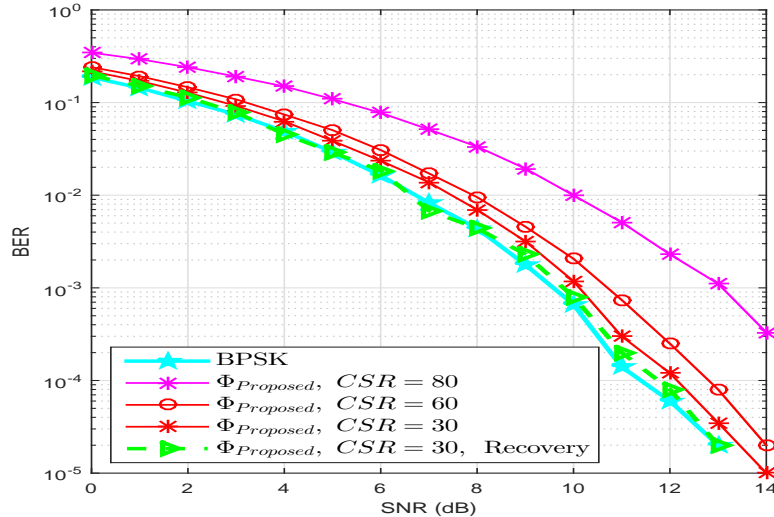


Figure 4.11: Average BER performance vs SNR.

Next, the affect of P and ς_p , $p = 1, \dots, P$ used in the proposed measurement matrix are investigated. The average BER performance of the proposed measurement matrix for $\text{CSR} = 60$ using different values of P with for $\varsigma_p > T_w$ is shown in Figure 4.12. As P increases, the sparsity of matrix decreases that may enhance the information capturing rate of the desired signal as well as noise contribution in the measurement signal. Until the value of $P \leq 5$, the impact of noise and information capturing ability perhaps match and we do not observe any change in the performance as is evident from Figure 4.12. However, the BER performance is observed to degrade as P increases, say for $P = 8$ with $\varsigma_p > T_w$ (Figure 4.12). Also, system complexity increases with higher value of P . Thus, a low value of P , in general, is preferable.

Further, for ς_p greater than T_w , there is no problem. However, as ς_p reduces below T_w , Φ has an overlap of UWB pulses. Since every column of Φ is normalized to unity, it has no perceptible impact on the performance of the proposed matrix.

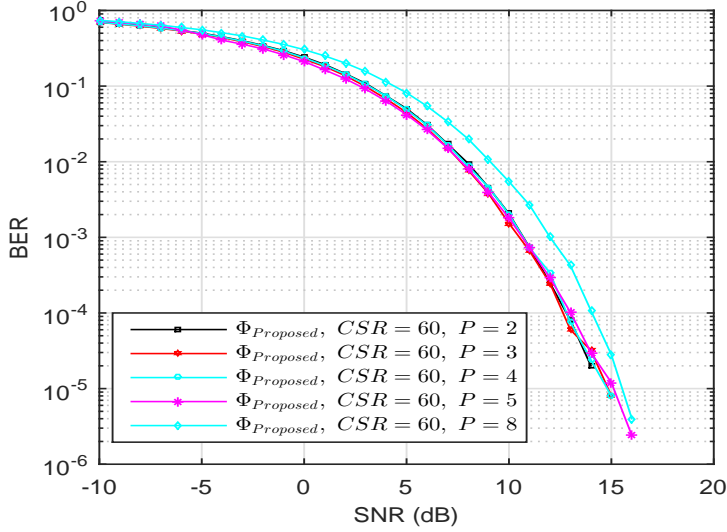


Figure 4.12: Average BER performance of the TH-BPSK UWB system in CM1 channel using the proposed measurement matrix with different values of P .

The estimate of computational performance depends upon the number of operations. Therefore, number of multiplications and additions for the Gaussian and the proposed measurement matrix is given in Table 4.1 for the system $\mathbf{y} = \Phi \mathbf{r} \in \mathbb{R}^M$, $\mathbf{r} \in \mathbb{R}^N$. In Table 4.1, N_1 is the total number of non-zero elements in a received signal \mathbf{r} and M_1 is the total number of non-zero elements in a row of the proposed measurement matrix. The value of $M_1 < N_1$ because multipath received signal has more number of non-zero elements as compared to a row of the proposed measurement matrix (for smaller value of P). Hence, the proposed matrix has a smaller number of multiplications and additions for the receiver design in the compressive sensing domain. Further, the memory requirement for the proposed sparse circulant matrix is also lower than the full Gaussian measurement matrix.

Table 4.1: Computational complexity of the proposed and Gaussian matrices

Measurement matrix	Multiplications	Additions
Gaussian	MN_1	$M(N_1 - 1)$
Proposed	MM_1	$M(M_1 - 1)$

4.5 Summary

In this chapter, a measurement matrix matched to the transmitted UWB waveform with circulant matrix structure is proposed. The BER performance of the UWB receiver system with the proposed matrix is derived in the compressive sensing domain and is compared with other deterministic DCT, Hadamard and random Gaussian measurement matrices in AWGN and multipath communication scenarios. BER performance of the compressive sensing based UWB receiver is better using the proposed measurement matrix as compared to the existing matrices with low hardware implementation complexity such as memory storage and operational time requirement. Same has also been verified through extensive simulations in both the compressed domain based detector and detector after signal recovery from the compressive measurements.

Chapter 5

IR-UWB Sensor Network using Massive MIMO Decision Fusion

In the previous chapter, sub-Nyquist rate UWB receiver design using compressive sensing is analyzed to reduce the sampling rate of the ADC. Further, 5G mobile communication network based IoT applications require high data rate, low power consumption, and reliable ubiquitous wireless connectivity to connect billions of devices together. To connect a large number of IoT devices, various licensed and unlicensed communication technologies can be used. Of these, the low power, large bandwidth and low cost IR-UWB technology is a viable solution for short-range wireless communication in picocell and femtocell networks.

In this chapter, IR-UWB system for WSN using MAAs at fusion center (FC) for distributed detection is proposed and analyzed. The coherent and energy based fusion rules are analyzed for the proposed WSN over multiple access channels. The trade-off between performance and implementation complexity of the coherent and energy based fusion is studied. Further, it is shown that the MAAs at FC and various level of channel knowledge can enhance the performance of energy-based detector in UWB sensor network with simple system implementation and signal processing requirement. Performance of the proposed UWB sensor network with reference to probability of detection, false alarm, and error are analyzed over standard IEEE

802.15.4a multipath channels and results are validated using simulations. The impact of various design parameters such as the number of sensors, receiver antennas, sensor quality, and integration interval on the system performance is also analyzed.

5.1 Introduction

In the UWB literature, both coherent and energy based detectors are used for detection and estimation of UWB signal. The coherent detector (CD) has better performance than the energy detector (ED) [92]. However, the CD is more complex than the ED due to a large number of taps-based UWB CIR estimation and requirement of high sampling rate and very accurate synchronization [92]. The ED is simple since it does not require knowledge of CIR and high sampling rate with sub-optimal performance due to the presence of noise. In this chapter, the performance of both CD and ED based fusion rules is explored. Further, ED's performance is improved by including the various statistics of the CIR at the FC. Therefore, a trade-off exists between detectors complexity and performance of the UWB WSN .

In WSNs, the sensor nodes function under severe constraints on energy consumption, size, precise self-location of the nodes, and high wireless data transmission rate. These requirements are fulfilled by the UWB transmission technology [93, 94]. In [94], a low-cost UWB sensor node is presented, wherein the UWB sensor uses power from piezoelectric harvester or solar cells. In literature, various UWB based WSN applications including localization and imaging of objects [95, 96], infrastructure quality monitoring [97], monitoring of highways, bridges and railways crossings [98], vehicle monitoring [99], and medicine [100, 101] have been considered. One important application of IoT is in assisted living (AL) that is gaining importance due to aging society [102, 103]. The AL technologies require accurate localization and reliable data transmission methods that may be achievable using UWB technology. In [101], length optimization of the medium access control frame body is carried out to maximize the energy efficiency in IEEE 802.15.6 UWB WBAN. In [96], passive UWB

RFID based high accuracy localization for tagged items are analyzed. Further, the UWB based RFID systems offer accurate localization with low power as compared to ultra high frequency (UHF) RFID system [96]. Thus, UWB-based sensor network concepts are being developed for both the industrial and the civil/military applications, especially, WSN systems based on the IEEE 802.15.4a standard [96, 97, 101].

In [104, 105], UHF/UWB hybrid transceiver design is proposed for RFID in IoT applications. In [104, 105], UHF signal is used to power up and tag the inventory, and UWB signal is used for data transmission and localization. Therefore, UHF/UWB hybrid RFID system (tags and readers) has better data rate and localization with marginal increment in implementation complexity as compared to a single UHF or UWB system. In [104, 105], ED is used, where performance can be enhanced using advanced signal processing techniques at the reader because the reader has higher processing power as compared to a tag. The UWB transmitted-reference (UWB-TR) transmission scheme based distributed detection in WSN s is described in [106]. The optimized number of UWB pulses used by each node to enhance the detection performance is also proposed in [106]. The UWB-TR does not require channel estimation at the FC. However, its performance degrades due to the noisy signal template in the correlator detector and battery life of sensor node can also decrease due to transmitted reference pulse in the TR scheme.

To reduce the energy consumption and communication resources¹ in WSNs, high array processing gain at FC is desirable. The higher array processing gain in WSN system can be achieved using a large number of sensor nodes and multiple antennas at FC. However, the large number of sensor nodes are not desirable in the sensor networks. Hence, multiple antennas at FC is a better design due to more processing power and energy availability. Thus, in this chapter, a UWB WSNs using multiple antennas at FC for distributed detection is proposed. In the proposed work, each sensor node has a single antenna, while MAAs are considered at FC to enhance detection performance.

¹The minimization of each sensor node's power requirement and the number of sensors in a WSN, leads to reduced energy consumption and communication resources respectively.

Both coherent and energy based fusion methods are studied at FC in wireless sensing over MAC. The CD has optimum performance with higher implementation complexity due to multiple CIR estimation, accurate synchronization and high sampling rate requirement. On the other hand, ED is attractive in terms of computational complexity, very low sampling rate and limited system knowledge requirement such as CIR with degraded system performance as compared to CD, especially, at low SNR. Further, the CIR estimation in CD is done at FC, where control and synchronization information² are broadcasted to each sensor node by FC. Therefore, local exchange of information among the sensor nodes is not required.

The use of multiple antennas can effectively increase the throughput of a wireless link. Further, recently researchers have investigated the use of MAAs in wireless communication systems in order to improve spectral and energy efficiency [108]. Hence, MAAs with various level of CIR knowledge can be used in ED to improve the system's performance. Fusion based on energy is suboptimal in UWB sensor network since the channel statistics do not follow the Rayleigh fading model. Hence, it is interesting and useful to study the UWB signal detection using ED with MAAs at FC. The proposed UWB sensor network system is analyzed for time hopping binary pulse position modulated (TH-BPPM) UWB signal over the standardized IEEE 802.15.4a multipath channel. The main contributions of this chapter are summarized as:

1. IR-UWB system for WSNs in massive multiple-input and multiple-output (MIMO) decision fusion is proposed and analyzed.
2. The UWB WSN is studied using both the coherent and energy based fusion rules. CD has optimum performance with higher implementation complexity due to multiple CIR estimation, accurate synchronization and high sampling rate requirement. On the other hand, ED is simple and has sub-optimum performance.

²The UWB or ultra-high-frequency (UHF) signal can be used for control and synchronization [107].

3. The MAAs and/or with various level of CIR knowledge are used with ED to improve the system's performance.
4. The impact of various design parameters such as the number of sensor nodes, sensor quality, integration interval and number of receive antennas on the system's performance is also analyzed.
5. The global detection, false alarm, and error probabilities of the proposed UWB sensor system are numerically analyzed and compared with semi-analytical results.

5.2 UWB-based WSN system model and general assumptions

In this section, the proposed UWB system for WSN using MAAs at FC is described for accurate localization and low power requirement based IoT applications. The proposed distributed WSN system consists of K sensing nodes and N antennas at FC with $K \ll N$. Since the proposed WSN system has multiple sensors and antennas at FC, it can be referred as the MIMO based sensor network. Each sensor observes desired events independently and sends its local observation wirelessly to FC through MAC. Observations at individual sensor nodes is sent using low power UWB signal to FC. The combined received signal from all N antennas is used for event detection and an antenna array processing gain can be obtained in the WSN. Based on the combined received signal from all the sensors and antennas, FC generates a global estimate of the event (present or absent in the considered system model). The proposed UWB system for WSN is shown in Figure 5.1. Each sensor node observes the desired event through the sensing channel and sends its individual decision using a TH-BPPM UWB signal to FC through the multipath reporting channel. This is to add that perfect sensing channels with reporting MAC to be noisy [106, 109–112] are considered. The k^{th} sensor and n^{th} antenna link are

denoted by $\text{link}_{u=(k,n)}$, where $k = 1, 2, \dots, K$, $n = 1, 2, \dots, N$ and $u = 1, 2, \dots, KN$. Therefore, the proposed system architecture in Figure 5.1 represents MIMO based distributed detection system model for WSN. In Figure 5.1, sensors and antennas are considered as inputs and outputs, respectively, for MIMO based FC. Further, quasi-synchronization³ among the sensors has been considered at FC and single hop-transmission in the network is assumed, i.e., each sensor node transmits its data to FC directly.

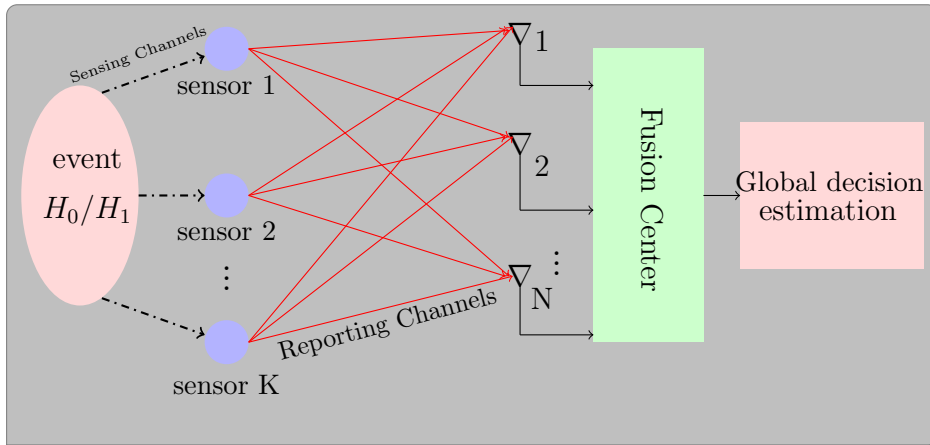


Figure 5.1: The proposed UWB WSN with large antenna arrays at fusion center.

5.2.1 Event-sensor link:sensing

In the proposed system model, each sensor senses the binary event Θ and decides for the absence or presence of the event. The absence and presence of an event is denoted by two hypothesis \mathcal{H}_0 and \mathcal{H}_1 with apriori probabilities \mathcal{P}_0 and \mathcal{P}_1 , respectively. Hence, Θ belongs to the set hypothesis $\mathcal{H} = \{\mathcal{H}_0, \mathcal{H}_1\}$, and \mathcal{H}_0 and \mathcal{H}_1 are defined as

$$\begin{aligned} \mathcal{H}_0 : r_s(t) &= n_\Theta(t) \\ \mathcal{H}_1 : r_s(t) &= a_\Theta(t) + n_\Theta(t), \end{aligned} \tag{5.1}$$

³The synchronization among the sensors can be established using a control signal from FC to each sensor.

where $r_s(t)$ is the received signal at the sensor node. $a_\Theta(t)$ and $n_\Theta(t)$ are the event signals (such as temperature, humidity) and noise, respectively. The noise is distributed as $n_\Theta(t) \sim \mathcal{N}(0, \sigma_\Theta^2)$. The decision variable using energy detection at the sensor node is expressed as $\mathcal{Y} = (\int_0^{T_{\text{obs}}} r_s^2(t) dt) / \sigma_\Theta^2$, where T_{obs} is the energy accumulation time. Therefore, event's presence and absence at the sensor node is written as

$$\begin{aligned} \mathcal{H}_0 : \text{event is absent} : d_m = 0 \text{ if } \mathcal{Y} < \mathcal{Y}_{\text{th}} \\ \mathcal{H}_1 : \text{event is present} : d_m = 1 \text{ if } \mathcal{Y} \geq \mathcal{Y}_{\text{th}}, \end{aligned} \tag{5.2}$$

where \mathcal{Y}_{th} is the threshold value and d_m is the sensor's binary decision. In (5.2), subscript m denotes the m^{th} observation time interval. Each sensor sends the corresponding decision ($d_m = 0$ or $d_m = 1$) through MAC to FC. Further, each sensor has the same⁴ local false alarm and detection probabilities denoted as p_f and p_d , respectively, that are expressed as

$$\begin{aligned} p_f &= Pr(\mathcal{Y} > \mathcal{Y}_{\text{th}} | \mathcal{H}_0) \\ p_d &= Pr(\mathcal{Y} \geq \mathcal{Y}_{\text{th}} | \mathcal{H}_1). \end{aligned} \tag{5.3}$$

All sensors are assumed to be perfect (perfect sensing case with $p_f = 0$ and $p_d = 1$). The estimation error for the event Θ at FC is assumed to occur due to noisy MAC links between the local sensors nodes and FC. In perfect sensing and noisy reporting links scenario, the detection or estimation error of event at FC is referred to as “*communication bound*” [109], since error occurs only during reporting phase like communication scenarios.

⁴Sensors may have different p_f and p_d depending on the noise level and, the distance between sensor and event. For simplicity, we assume a homogeneous scenario in which both p_f and p_d be the same for all sensor nodes.

5.2.2 Sensor-FC link:reporting

Each sensor node transmits the local decision ($d_m = 0$ or 1) using the TH-BPPM⁵ UWB signal to the FC. In UWB, each data symbol is transmitted over N_f consecutive frames to limit the transmitted signal power within the FCC spectral mask. The transmitted signal by the k^{th} sensor using UWB pulse $w(t)$ of duration T_w can be written as

$$s_k(t) = \sqrt{P_k} \sum_{m=0}^{\infty} p(t - mT_s), \quad t \in \mathbb{R}, \quad (5.4)$$

where $P_k \in (0, 1]$ is the power scaling used by the k^{th} sensor, $T_s = N_f T_f$ symbol duration and

$$p(t) = \sqrt{\frac{E}{N_f}} \sum_{j=0}^{N_f-1} w(t - jT_f - c_j^k T_c - d_m^k \Delta), \quad (5.5)$$

where T_f , T_c , and E are frame duration, chip duration, and transmitted energy per data symbol, respectively. $\{c_j^k\}$ is the pseudo-random TH code for the k^{th} sensor with period N_p and cardinality N_h , and $d_m^k \in \{0, 1\}$ is the data symbol of the k^{th} sensor in m^{th} time instant. Δ is the pulse shift parameter for $d_m^k = 1$ in a frame. Further, the UWB pulse has unit energy, i.e., $E_w = \int_{-\infty}^{\infty} w^2(t) dt = 1$. The UWB sensors can have energy harvesting unit and may not continuously send the data to the FC. Therefore, it is assumed that only few sensor nodes K^6 send the observation to the FC at a random observation time interval due to limited energy in the system. Thus, total energy of all the sensors for transmission at a time is limited as $\sum_k P_k \leq \mathcal{E}_{\text{sys}}$, where \mathcal{E}_{sys} is the available energy in the system.

Received signal corresponding to the k^{th} sensor and n^{th} antenna link over mul-

⁵If event presence (\mathcal{H}_1) is less likely, i.e., ($Pr(\mathcal{H}_1) \ll Pr(\mathcal{H}_0)$), On-Off keying can be employed for energy efficiency.

⁶ \mathcal{K} is the total number of sensors in the system. However, only K sensors are active at a time with $K \ll \mathcal{K}$.

tipath MAC [106] is given as

$$r_{n,k}(t) = \overbrace{s_k(t - \varsigma_k)}^{\tilde{s}_{n,k}(t - \varsigma_k)} * h_{n,k}(t) + z_{n,k}(t), \quad n = 1, 2, \dots, N, \quad k = 1, 2, \dots, K, \quad (5.6)$$

where $'*$ ' is the convolution operator. Parameter ς_k is the time arrival difference among sensor signals at the n^{th} antenna. The $h_{n,k}(t)$ is the CIR between k^{th} sensor and n^{th} antenna link with L number of resolved multipath, expressed as $h_{n,k}(t) = \sum_{l=0}^{L-1} \alpha_l^{n,k} \delta(t - \tau_l^{n,k})$, where $\alpha_l^{n,k}$ and $\tau_l^{n,k}$ are the gain and time delay of l^{th} multipath, respectively. The $z_{n,k}(t)$ is AWGN of zero mean, and $\sigma_{z_{n,k}}^2$ variance i.e. $z_{n,k}(t) \sim \mathcal{N}(0, \sigma_{z_{n,k}}^2)$. The combined signal $y_n(t)$ of all the transmitted sensors K at the n^{th} antenna is expressed as

$$y_n(t) = \frac{1}{K} \sum_{k=1}^K r_{n,k}(t) = r_n(t) + z_n(t), \quad n = 1, 2, \dots, N, \quad (5.7)$$

where

$$r_n(t) = \frac{1}{K} \sum_{k=1}^K \tilde{s}_{n,k}(t - \varsigma_k) = \sum_{k=1}^K \sum_{l=0}^{L-1} \alpha_l^{n,k} s_k(t - \tau_l^{n,k} - \varsigma_k), \quad (5.8)$$

and $z_n(t) = \frac{1}{K} \sum_{k=1}^K z_{n,k}(t)$

To avoid ISI at FC, frame duration to be higher than the delay spread T_{del} of the channel is considered i.e., $T_f \geq T_{\text{del}}$. Further, time-resolved multiple replicas of the transmitted signal are assumed, i.e., $|\tau_l^{n,k} - \tau_{l-1}^{n,k}| \geq T_w \quad \forall n, k, l$. Therefore, each $r_{n,k}(t)$ is sparse at the FC in the time domain. The estimation of d_m at the FC is referred to as global decision estimation of the event. The accurate estimation of d_m is desirable using very less number of sensors (to save communication resource and energy) in the presence of noise at the FC. The individual link's (sensor-antenna) signal-to-noise ratio (SNR $_{n,k}$) for a data symbol is defined as $\text{SNR}_{n,k} = (P_k EN_f \mathbb{E}\{\|h_{n,k}(t)\|^2\}) / \sigma_{z_{n,k}}^2$. Further, SNR at the n^{th} antenna is de-

defined as $\text{SNR}_n = \mathbb{E}\{\|r_n(t)\|^2\}/\mathbb{E}\{\|z_n(t)\|^2\}$. Furthermore, SNR enhancement at FC depends on the coherent or non-coherent fusion methods to process the combined signal of all the antennas.

5.3 Decision fusion

The coherent and energy detectors for global event detection at the FC for the proposed UWB sensor network are considered. If we detect $d_m = 0$ or $d_m = 1$ at m^{th} observation time using all the sensors' signal at FC, the event Θ is absent (\mathcal{H}_0) or present (\mathcal{H}_1) in the sensor system, respectively. Advantages and drawbacks of each coherent and non-coherent based fusion rule in terms of complexity, system knowledge required, and performances are discussed.

5.3.1 Coherent detection

The correlator based coherent detection is used for event detection at FC. The correlation between received signal and the local reference signal is calculated, and its value is compared with predetermined threshold for hypothesis detection at FC. The reference signal is derived using the CIR of each antenna-sensor link and is expressed as

$$\text{ref}_{n,k}(t) = [w(t - jT_f - c_j^k T_c - \varsigma_k) - w(t - jT_f - c_j^k T_c - \varsigma_k - \Delta)] * h_{n,k}(t). \quad (5.9)$$

Further, reference signal for each frame⁷ is expressed as $\text{ref}_{n,k}(t) = \tilde{w}(t) - \tilde{w}(t - \Delta)$, where $\tilde{w}(t) = w(t) * h_{n,k}(t)$. The correlator output for each signal frame at n^{th}

⁷Analysis is carried out for the first frame signal and the frame index is removed for simplicity. Further, terms $c_j^k T_c$ and ς_k can be adjusted inside the CIR; hence, removed in the $\text{ref}_{n,k}(t)$, and $\tilde{s}_{n,k}(t) \cong \tilde{s}_{n,k}(t - \varsigma_k)$ is used.

antenna for k^{th} sensor is expressed as

$$r_{n,k} = \int_0^{T_f} r_{n,k}(t) \text{ref}_{n,k}(t) dt, \quad n = 1, 2, \dots, N, \quad k = 1, 2, \dots, K \quad (5.10)$$

Next, $r_{n,k}$ is expressed as

$$\begin{aligned} r_{n,k} &= \int_0^{T_f} \{\tilde{s}_{n,k}(t) + z_{n,k}(t)\} \text{ref}_{n,k}(t) dt \\ r_{n,k} &= \underbrace{\int_0^{T_f} \tilde{s}_{n,k}(t) \text{ref}_{n,k}(t) dt}_{s_{n,k} = s_{n,k,0} - s_{n,k,1}} + \underbrace{\int_0^{T_f} z_{n,k}(t) \text{ref}_{n,k}(t) dt}_{z_{n,k} = z_{n,k,0} - z_{n,k,1}} \end{aligned} \quad (5.11)$$

where $s_{n,k,0}$, $s_{n,k,1}$, $z_{n,k,0}$ and $z_{n,k,1}$ are expressed in (5.13) and the combined signal of all sensor at n^{th} antenna is given as

$$\begin{aligned} r_n &= \frac{1}{K} \sum_{k=1}^K r_{n,k} \\ r_n &= \underbrace{\frac{1}{K} \sum_{k=1}^K s_{n,k,0}}_{s_{n,0}} - \underbrace{\frac{1}{K} \sum_{k=1}^K s_{n,k,1}}_{s_{n,1}} + \underbrace{\frac{1}{K} \sum_{k=1}^K z_{n,k,0}}_{z_{n,0}} - \underbrace{\frac{1}{K} \sum_{k=1}^K z_{n,k,1}}_{z_{n,1}} \end{aligned} \quad (5.12)$$

$$\begin{aligned} s_{n,k} &= \underbrace{\int_0^{T_f} \tilde{s}_{n,k}(t) \tilde{w}(t) dt}_{s_{n,k,0}} - \underbrace{\int_0^{T_f} \tilde{s}_{n,k}(t) \tilde{w}(t - \Delta) dt}_{s_{n,k,1}}, \\ z_{n,k} &= \underbrace{\int_0^{T_f} z_{n,k}(t) \tilde{w}(t) dt}_{z_{n,k,0}} - \underbrace{\int_0^{T_f} z_{n,k}(t) \tilde{w}(t - \Delta) dt}_{z_{n,k,1}} \end{aligned} \quad (5.13)$$

Further, the combined signal of all the antennas is expressed as

$$r = \frac{1}{N} \sum_{n=1}^N r_n = s_0 - s_1 + z_0 - z_1, \quad (5.14)$$

where $s_0 = \frac{1}{N} \sum_{n=1}^N s_{n,0}$, $s_1 = \frac{1}{N} \sum_{n=1}^N s_{n,1}$, $z_0 = \frac{1}{N} \sum_{n=1}^N z_{n,0}$ and $z_1 = \frac{1}{N} \sum_{n=1}^N z_{n,1}$. The decision variable r at FC is distributed as $r \sim \mathcal{N}(\mu_{r,\text{coh}}, \Omega_{\text{coh}})$, where $\mu_{r,\text{coh}} = \mathbb{E}\{r\}$ and $\Omega_{\text{coh}} = \text{Var}\{r\}$.

Further, $\mu_{r,\text{coh}}$ and Ω_{coh} are expressed as

$$\begin{aligned}\mu_{r,\text{coh}} &= \mathbb{E}\{s_0 - s_1\} = \frac{1}{N} \sum_{n=1}^N \mathbb{E}\{s_{n,0}\} - \frac{1}{N} \sum_{n=1}^N \mathbb{E}\{s_{n,1}\} \\ \mu_{r,\text{coh}} &= \frac{1}{NK} \sum_{n=1}^N \sum_{k=1}^K \mathbb{E}\{s_{n,k,0}\} - \frac{1}{NK} \sum_{n=1}^N \sum_{k=1}^K \mathbb{E}\{s_{n,k,1}\}\end{aligned}\quad (5.15)$$

with $\mathbb{E}\{s_{n,k,0}\} = \mathbb{E}\left\{\int_0^{T_f} \tilde{s}_{n,k}(t)\tilde{w}(t)dt\right\}$ and $\mathbb{E}\{s_{n,k,1}\} = \mathbb{E}\left\{\int_0^{T_f} \tilde{s}_{n,k}(t)\tilde{w}(t-\Delta)dt\right\}$, and variance

$$\Omega_{\text{coh}} = \frac{1}{N^2K^2} \sum_{n=1}^N \sum_{k=1}^K \tilde{\sigma}_{n,k,0}^2 + \frac{1}{N^2K^2} \sum_{n=1}^N \sum_{k=1}^K \tilde{\sigma}_{n,k,1}^2 \quad (5.16)$$

where $\tilde{\sigma}_{n,k,0}^2$ and $\tilde{\sigma}_{n,k,1}^2$ are expressed in (5.17).

$$\begin{aligned}\tilde{\sigma}_{n,k,0}^2 &= \mathbb{E}\left\{\left(\int_0^{T_f} z_{n,k}(t)\tilde{w}(t)dt\right)^2\right\} - \left(\mathbb{E}\left\{\int_0^{T_f} z_{n,k}(t)\tilde{w}(t)dt\right\}\right)^2 \quad \text{and} \\ \tilde{\sigma}_{n,k,1}^2 &= \mathbb{E}\left\{\left(\int_0^{T_f} z_{n,k}(t)\tilde{w}(t-\Delta)dt\right)^2\right\} - \left(\mathbb{E}\left\{\int_0^{T_f} z_{n,k}(t)\tilde{w}(t-\Delta)dt\right\}\right)^2.\end{aligned}\quad (5.17)$$

The global probabilities of false alarm (\mathcal{P}_F) and correct detection (\mathcal{P}_D) at FC are defined as

$$\begin{aligned}\mathcal{P}_F &= Pr(r|\mathcal{H}_0 \leq \Upsilon_{\text{coh}}) \\ \mathcal{P}_D &= Pr(r|\mathcal{H}_1 \leq \Upsilon_{\text{coh}}),\end{aligned}\quad (5.18)$$

where Υ_{coh} is a threshold value. Further, the global probability of error \mathcal{P}_E at FC is defined as $\mathcal{P}_E = Pr(\mathcal{H}_1)Pr(\mathcal{H}_0|\mathcal{H}_1) + Pr(\mathcal{H}_0)Pr(\mathcal{H}_1|\mathcal{H}_0)$, where $Pr(\mathcal{H}_0)$ and $Pr(\mathcal{H}_1)$ is the probability of hypothesis \mathcal{H}_0 and \mathcal{H}_1 , respectively and $Pr(\mathcal{H}_0) + Pr(\mathcal{H}_1) = 1$. $Pr(\mathcal{H}_i|\mathcal{H}_j)$ is the conditional probability of hypothesis \mathcal{H}_i for given hypothesis \mathcal{H}_j , $i, j = 0, 1$, $i \neq j$.

\mathcal{P}_F using (5.14) and (5.18) is expressed as

$$\mathcal{P}_F = Q \left(\sqrt{\frac{NK \left[\Upsilon_{\text{coh}} - \frac{1}{NK} \sum_{n=1}^N \sum_{k=1}^K \mathbb{E}\{s_{n,k,0}\} \right]^2}{\frac{1}{N^2 K^2} \sum_{n=1}^N \sum_{k=1}^K \tilde{\sigma}_{n,k,0}^2 + \frac{1}{N^2 K^2} \sum_{n=1}^N \sum_{k=1}^K \tilde{\sigma}_{n,k,1}^2}} \right) \quad (5.19)$$

In (5.19) without loss of generality, it is assumed that signal and noise to be independent and equally distributed across all the antennas at FC. Further, by considering $\bar{U} = \mathbb{E}\{s_{n,k,0}\} \forall k, n$ and $\tilde{\sigma}_{\text{coh}}^2 = \tilde{\sigma}_{n,k,0}^2 = \tilde{\sigma}_{n,k,1}^2$, \mathcal{P}_F in (5.19) is written as

$$\mathcal{P}_F = Q \left(\sqrt{\frac{NK [\Upsilon_{\text{coh}} - \bar{U}]^2}{2\tilde{\sigma}_{\text{coh}}^2}} \right) \quad (5.20)$$

The threshold Υ_{coh} can be derived by fixing the \mathcal{P}_F and is expressed as

$$\Upsilon_{\text{coh}} = \bar{U} + \sqrt{\frac{2\tilde{\sigma}_{\text{coh}}^2 [Q^{-1}(\mathcal{P}_F)]^2}{NK}}. \quad (5.21)$$

In (5.20), the diversity order is $\mathcal{C}_{\text{div,coh}} = NK$. Hence, as $\mathcal{C}_{\text{div,coh}}$ increases, \mathcal{P}_F reduces, and approaches zero for $\mathcal{C}_{\text{div,coh}} \rightarrow \infty$. Further, SNR at FC using all links is expressed as $\text{SNR} = 10 \log_{10}(NK) + \text{SNR}_{\text{link}}$, where SNR_{link} is a single link SNR as defined earlier in Section II. Therefore, SNR enhancement in the proposed UWB sensor network is expressed as

$$\text{SNR}_{\text{en}} = 10 \log_{10}(NK). \quad (5.22)$$

One of the key observation of the CD-based fusion for the proposed UWB WSN application is that the sensor's transmitted power can be reduced by a factor of $1/N$ to maintain a constant detection error probability performance of the sensor network at FC as $N \rightarrow \infty$.

Lemma 1. *The test statistic $\bar{\nabla} = \frac{(\mathbb{E}\{s_0\} - \mathbb{E}\{s_1\})^2}{\text{Var}(s_1|d_m=0)}$ remains almost constant as $N \rightarrow \infty$ provided that the sensor's transmitted power satisfies $\frac{P_k}{N}$ for arbitrary energy constant P_k .*

Proof. Using (5.14)

$$\lim_{N \rightarrow \infty} \bar{\nabla} = \frac{(\mathbb{E}\{s_0\} - \mathbb{E}\{s_1\})^2}{\text{Var}(s_1|d_m = 0)} \quad (5.23)$$

where

$$\begin{aligned} \lim_{N \rightarrow \infty} \mathbb{E}\{s_0\} &= \lim_{N \rightarrow \infty} \mathbb{E} \left\{ \frac{1}{N} \sum_{n=1}^N s_{n,0} \right\} \\ \lim_{N \rightarrow \infty} \mathbb{E}\{s_0\} &= \sigma_{\text{sig}}^2 \end{aligned} \quad (5.24)$$

Similarly, we derive

$$\begin{aligned} \lim_{N \rightarrow \infty} \mathbb{E}\{s_1\} &= \lim_{N \rightarrow \infty} \mathbb{E} \left\{ \frac{1}{N} \sum_{n=1}^N s_{n,1} \right\} \\ \lim_{N \rightarrow \infty} \mathbb{E}\{s_1\} &= 0 \end{aligned} \quad (5.25)$$

and

$$\begin{aligned} \lim_{N \rightarrow \infty} \text{Var}(s_1|d_m = 0) &= \lim_{N \rightarrow \infty} \text{Var} \left\{ \frac{1}{N} \sum_{n=1}^N (s_1|d_m = 0) \right\} \\ \lim_{N \rightarrow \infty} \text{Var}(s_1|d_m = 0) &= \frac{\sigma_{\text{sig}}^2 \sigma_{z_0}^2}{N} \end{aligned} \quad (5.26)$$

Therefore, using (5.24), (5.25) and (5.26), $\bar{\nabla}$ is expressed as

$$\lim_{N \rightarrow \infty} \bar{\nabla} = \frac{N \sigma_{\text{sig}}^2}{\sigma_{z_0}^2} \quad (5.27)$$

Now, substituting $\sigma_{\text{sig}}^2 = P_k/N$ into (5.27), we obtain

$$\lim_{N \rightarrow \infty} \bar{\nabla} = \frac{P_k}{\sigma_{z_0}^2} \quad (5.28)$$

The $\bar{\nabla}$ is asymptotically independent of N . Thus, asymptotically non-zero statistic $\bar{\nabla}$ requires that sensor energy (P_k) not decrease faster than $1/N$. \square

The coherently combined sensors' signal produces array processing gain at FC and SNR grows linearly as the number of sensor nodes and antennas at FC increases.

Hence, the noise level in hypothesis estimation at FC reduces significantly using CD for a moderate value of antennas and sensor nodes in WSNs. However, synchronization among all individual links (between the k^{th} sensor node and the n^{th} antenna at FC) is difficult to achieve due to a very short time duration of UWB signal. Further, UWB multipath channels have large number of non-zero channel taps, which makes CIR estimation more complex and time demanding, i.e., higher latency. Thus, for assisted living and critical applications such as biomedical, coherent detection is not a feasible solution due to large processing time requirement for a hypothesis estimation and complex design of FC in UWB sensor network. Furthermore, CD also needs Nyquist rate sampling, which may not be feasible or require costly ADC. Therefore, the coherent processing of all sensors' data using multiple antennas at FC is practically unrealizable (or difficult) [92], and needs some simple signal processing methods to estimate the hypothesis at FC in WSN.

5.3.2 Non-coherent energy detector

In this subsection, a signal energy based non-coherent detector is analyzed for the proposed UWB based WSN because ED is simple and does not need CIR, SNR and local sensor performance. The ED based fusion at FC has been analyzed over flat frequency and Rayleigh fading channels in the literature. In this chapter, for the first time, we show how ED can provide an interesting test for the estimation of hypothesis at FC for UWB channels that are neither flat nor Rayleigh distributed. Since BPPM UWB signal is transmitted by the sensor nodes, ED calculates the energy of the received signal in the first and second halves in each frame separately. The first and second half signals in a frame are expressed as $r_{n,k,0}(t)$ and $r_{n,k,1}(t)$, respectively, where

$$\begin{aligned} r_{n,k,0}(t) &= \tilde{s}_{n,k}(t) + z_{n,k}(t), \text{ and} \\ r_{n,k,1}(t) &= \tilde{s}_{n,k}(t - \Delta) + z_{n,k}(t - \Delta). \end{aligned} \tag{5.29}$$

The energy of the received signal for each half of a frame for a single link at FC is expressed as

$$\begin{aligned}
 \mathcal{E}_{n,k,0} &= \int_0^{T_f/2} r_{n,k,0}^2(t) dt = \int_0^{T_f/2} \tilde{s}_{n,k}^2(t) dt + \\
 &\quad \int_0^{T_f/2} z_{n,k}^2(t) dt + 2 \int_0^{T_f/2} \tilde{s}_{n,k}(t) z_n(t) dt, \quad \text{and} \\
 \mathcal{E}_{n,k,1} &= \int_{T_f/2}^{T_f} r_{n,k,1}^2(t) dt = \int_{T_f/2}^{T_f} \tilde{s}_{n,k}^2(t - \Delta) dt + \\
 &\quad \int_{T_f/2}^{T_f} z_{n,k}^2(t - \Delta) dt + 2 \int_{T_f/2}^{T_f} \tilde{s}_{n,k}(t - \Delta) z_{n,k}(t - \Delta) dt. \quad (5.30)
 \end{aligned}$$

The average energy of all the sensors' received signal at n^{th} antenna is expressed as

$$\mathcal{E}_n = \underbrace{\frac{1}{K} \sum_{n=1}^K \mathcal{E}_{n,k,0}}_{\mathcal{E}_{n,0}} - \underbrace{\frac{1}{K} \sum_{n=1}^K \mathcal{E}_{n,k,1}}_{\mathcal{E}_{n,1}}, \quad (5.31)$$

where $\mathcal{E}_{n,0}$ and $\mathcal{E}_{n,1}$ are the first and second half energy, respectively, at a single antenna. The decision variable for a frame after combining all antennas' energy is expressed as

$$\begin{aligned}
 \mathcal{E} &= \underbrace{\frac{1}{N} \sum_{n=1}^N \mathcal{E}_{n,0}}_{\mathcal{E}_0} - \underbrace{\frac{1}{N} \sum_{n=1}^N \mathcal{E}_{n,1}}_{\mathcal{E}_1} \\
 \mathcal{E} &= \mathcal{E}_0 - \mathcal{E}_1
 \end{aligned} \quad (5.32)$$

Therefore, \mathcal{E} is the energy difference between first and second halves of the signal in a frame at FC using all sensor nodes and antennas. The objective is to estimate unknown hypothesis \mathcal{H}_0 or \mathcal{H}_1 based on the derived variable \mathcal{E} . The variable \mathcal{E} is distributed as $\mathcal{E} \sim \mathcal{N}(\mu_{\mathcal{E}}, \sigma_{\mathcal{E}}^2)$ ⁸, where $\mu_{\mathcal{E}} = \mathbb{E}\{\mathcal{E}\}$ and $\sigma_{\mathcal{E}}^2 = \text{Var}\{\mathcal{E}\}$.

Next, the global probabilities of false alarm \mathcal{P}_F and correct detection \mathcal{P}_D are

⁸For large time-bandwidth product (i.e., large samples in a frame) of UWB signal and, for large number of sensors and antennas, the distribution of \mathcal{E} is approximated as Gaussian distributed using the central limit theorem as shown in Figure 5.6.

defined as

$$\begin{aligned}\mathcal{P}_F &= Pr(\mathcal{E}|\mathcal{H}_0 \leq \Upsilon_{ED}) \\ \mathcal{P}_D &= Pr(\mathcal{E}|\mathcal{H}_1 \leq \Upsilon_{ED}).\end{aligned}\tag{5.33}$$

where Υ_{ED} is a threshold value. Let $d_m = 0$ be the sensor node's transmitted decision about the event. $\mathcal{E}_{n,k,0}$ and $\mathcal{E}_{n,k,1}$ are expressed as

$$\mathcal{E}_{n,k,0} = \underbrace{\int_0^{T_f/2} \tilde{s}_{n,k}^2(t) dt}_{\sigma_{\text{sig}}^2} + \underbrace{\int_0^{T_f/2} z_{n,k}^2(t) dt}_{\sigma_{\tilde{z}_{n,k,0}}^2} + 2 \underbrace{\int_0^{T_f/2} \tilde{s}_{n,k}(t) z_{n,k}(t) dt}_{\zeta_{n,k}}\tag{5.34}$$

$$\text{and } \mathcal{E}_{n,k,1} = \underbrace{\int_{T_f/2}^{T_f} z_{n,k}^2(t - \Delta) dt}_{\sigma_{\tilde{z}_{n,k,1}}^2}.\tag{5.35}$$

Further,

$$\mathcal{E}_n = \frac{1}{K} \sum_{k=1}^K \left(\sigma_{\text{sig}}^2 + \sigma_{\tilde{z}_{n,k,0}}^2 + 2\zeta_{n,k} \right) - \frac{1}{K} \sum_{k=1}^K \sigma_{\tilde{z}_{n,k,1}}^2.\tag{5.36}$$

Therefore, \mathcal{E} can be written as

$$\mathcal{E} = \sigma_{\text{sig}}^2 + \frac{1}{NK} \sum_{n=1}^N \sum_{k=1}^K \sigma_{\tilde{z}_{n,k,0}}^2 - \frac{1}{NK} \sum_{n=1}^N \sum_{k=1}^K \sigma_{\tilde{z}_{n,k,1}}^2 + \underbrace{\frac{2}{NK} \sum_{n=1}^N \sum_{k=1}^K \zeta_{n,k}}_{\Sigma}\tag{5.37}$$

Hence, $\mu_{\mathcal{E}} = \sigma_{\text{sig}}^2 + \mathbb{E}\{\Sigma\}$ and $\sigma_{\mathcal{E}}^2 = \frac{4}{NK} \sigma_{\text{sig}}^2 \sigma_{\tilde{z}_0}^2 - (\mathbb{E}\{\Sigma\})^2$, with $\sigma_{\tilde{z}_0}^2 = (\sigma_{\tilde{z}_{n,k,0}}^2 \cong \sigma_{\tilde{z}_{n,k,1}}^2)$ and $\sigma_{\tilde{z}_0}^4 = (\sigma_{\tilde{z}_{n,k,0}}^4 \cong \sigma_{\tilde{z}_{n,k,1}}^4)$, since noise is independent and identically distributed across all the antennas and frames. Therefore, \mathcal{P}_F for non-coherent ED is expressed as

$$\mathcal{P}_F = Q \left(\sqrt{\frac{NK(\Upsilon_{ED} - \sigma_{\text{sig}}^2 - \mathbb{E}\{\Sigma\})^2}{4\sigma_{\text{sig}}^2 \sigma_{\tilde{z}_0}^2 - NK(\mathbb{E}\{\Sigma\})^2}} \right).\tag{5.38}$$

As K and N increases, the \mathcal{P}_F in (5.38) decreases.

As $N \rightarrow \infty$ for fixed value of K with $K \ll N$, mean term $\mu_{\mathcal{E}}$ converges to σ_{sig}^2 and variance $\sigma_{\mathcal{E}}^2$ term converges to $\frac{4}{NK} \sigma_{\text{sig}}^2 \sigma_{\tilde{z}_0}^2$ in (5.37). Therefore, the noise level

in the ED approaches zero by exploiting the sum of large numbers. Hence, a large number of received antenna arrays makes ED performance close to the coherent detection and \mathcal{P}_F in (5.37) is rewritten as

$$\mathcal{P}_F = Q \left(\sqrt{\frac{NK(\Upsilon_{\text{ED}} - \sigma_{\text{sig}}^2)^2}{4\sigma_{\text{sig}}^2\sigma_{z_0}^2}} \right). \quad (5.39)$$

Further, to understand the effect of MAAs at FC in energy based fusion, let us consider $K = 1$. \mathcal{E} is given as

$$\begin{aligned} \mathcal{E} &= \frac{1}{N} \sum_{k=1}^N \xi_{n,0}^2 - \frac{1}{N} \sum_{k=1}^N \xi_{n,1}^2 \\ &= \frac{1}{N} \|\xi_0\|_2^2 - \frac{1}{N} \|\xi_1\|_2^2, \end{aligned} \quad (5.40)$$

where $\xi_{n,0}^2 = \int_0^{T_f/2} r_{n,0}^2(t) dt$ and $\xi_{n,1}^2 = \int_{T_f/2}^{T_f} r_{n,1}^2(t) dt$. Equation (5.40) for $d_m = 0$ can be written as

$$\mathcal{E} = \underbrace{\frac{1}{N} \|s\|_2^2}_{\text{signal}} + \underbrace{\frac{1}{N} \|n_0\|_2^2 - \frac{1}{N} \|n_1\|_2^2}_{\text{noise}} + \underbrace{\frac{2}{N} \sum_{n=1}^N (\langle s_n(t), z_n(t) \rangle)}_{\mathcal{SN}} \quad (5.41)$$

Thus, as $N \rightarrow \infty$, the first signal term in (5.41) converges to σ_{sig}^2 according to the sum of large numbers. Further, the second term noise $\rightarrow 0$ in (5.41), and the last term \mathcal{SN} in (5.41) is arbitrary close to zero as $N \rightarrow \infty$. Therefore, ED using large number of received antenna arrays makes the noise level zero in the decision variable \mathcal{E} ($N \rightarrow \infty, \mathcal{E} \rightarrow \sigma_{\text{sig}}^2$) before the estimation of hypothesis is performed at the FC in the proposed UWB sensor network. Hence, the error-free event estimation ($\Theta \in \mathcal{H}$) at FC can be achieved using an arbitrary small number of sensor nodes and MAAs based UWB WSNs. Therefore, the proposed sensor network results in an extended lifespan of sensor's battery (using MAAs) and saves communication resources (using less sensors) in WSN.

Further, one of the significant properties of the ED-based fusion for the proposed UWB WSN application is that the sensor's transmit power can be reduced by a

factor of $1/\sqrt{N}$ to maintain a constant energy difference between the first and the second half signal in a frame as $N \rightarrow \infty$ at FC.

Lemma 2. *The test statistic $\bar{\mathcal{E}} = \frac{(\mathbb{E}\{\mathcal{E}_0\} - \mathbb{E}\{\mathcal{E}_1\})^2}{\text{Var}(\mathcal{E}_1|d_m=0)}$ almost remains constant as $N \rightarrow \infty$ provided that the sensor transmit power satisfies $\frac{P_k}{\sqrt{N}}$ for arbitrary energy constant P_k .*

Proof. Using (5.32)

$$\lim_{N \rightarrow \infty} \bar{\mathcal{E}} = \frac{(\mathbb{E}\{\mathcal{E}_0\} - \mathbb{E}\{\mathcal{E}_1\})^2}{\text{Var}(\mathcal{E}_1|d_m=0)} \quad (5.42)$$

where

$$\begin{aligned} \lim_{N \rightarrow \infty} \mathbb{E}\{\mathcal{E}_0\} &= \lim_{N \rightarrow \infty} \mathbb{E} \left\{ \frac{1}{N} \sum_{n=1}^N \mathcal{E}_{n,0} \right\} \\ &= \lim_{N \rightarrow \infty} \frac{1}{N} \mathbb{E} \left\{ \sum_{n=1}^N \left(\frac{1}{K} \sum_{k=1}^K (\underline{s}_{n,k} + \sigma_{\underline{z}_{n,k,0}}^2 + 2\zeta_{n,k}) \right) \right\} \\ \lim_{N \rightarrow \infty} \mathbb{E}\{\mathcal{E}_0\} &= \sigma_{\text{sig}}^2 + \sigma_{\underline{z}_0}^2 \end{aligned} \quad (5.43)$$

Similarly, we derive

$$\begin{aligned} \lim_{N \rightarrow \infty} \mathbb{E}\{\mathcal{E}_1\} &= \lim_{N \rightarrow \infty} \mathbb{E} \left\{ \frac{1}{N} \sum_{n=1}^N \mathcal{E}_{n,1} \right\} \\ &= \sigma_{\underline{z}_0}^2 \end{aligned} \quad (5.44)$$

$$\begin{aligned} \lim_{N \rightarrow \infty} \text{Var}(\mathcal{E}_1|d_m=0) &= \lim_{N \rightarrow \infty} \text{Var} \left\{ \frac{1}{N} \sum_{n=1}^N (\mathcal{E}_{n,1}|d_m=0) \right\} \\ &= \frac{\sigma_{\underline{z}_0}^4}{N} \end{aligned} \quad (5.45)$$

Therefore, using (5.43), (5.44) and (5.45), $\bar{\mathcal{E}}$ is expressed as

$$\lim_{N \rightarrow \infty} \bar{\mathcal{E}} = \frac{N\sigma_{\text{sig}}^4}{\sigma_{\underline{z}_0}^4} \quad (5.46)$$

Introducing new variable $\sigma_{\text{sig}}^2 = \mathcal{G}$, (5.46) is written as

$$\lim_{N \rightarrow \infty} \bar{\mathcal{E}} = \frac{N\mathcal{G}^2}{\sigma_{\underline{z}_0}^4} \quad (5.47)$$

Now, substituting $\mathcal{G} = P_k/\sqrt{N}$ into (5.47), we obtain

$$\lim_{N \rightarrow \infty} \bar{\mathcal{E}} = \frac{P_k^2}{\sigma_{z_0}^4} \quad (5.48)$$

We observe that $\bar{\mathcal{E}}$ is asymptotically independent of N . Hence, asymptotically non-zero statistic $\bar{\mathcal{E}}$ requires that sensor energy (P_k) does not decrease faster than $1/\sqrt{N}$.

□

The ED based sensor fusion suffers due to the presence of noise in the decision variable as shown (5.36). However, ED based sensor fusion is simple to implement and needs low level signal processing. Also, its performance can achieve CD's performance at high SNR by using a large number of antenna arrays at FC.

5.4 ED performance enhancement using various side system information

In this section, performance enhancement of the ED-based fusion in the sensor network is proposed using available apriori information of the system.

5.4.1 Amplitude envelope of CIR

The UWB CIR has amplitude discontinuity due to cluster sparse nature [6, 92]. The shape of the cluster power delay profile (PDP) is useful in non-coherent receiver design. The most common PDP model of UWB CIR is the one-side exponential decay function [6, 92, 113] based on the ray tracking theory and the statistical property of UWB signal propagations as shown in Figure 5.2. The amplitude envelope of clustered CIR can lead to efficient energy computation of the received signal in a non-coherent morereceiver. It is evident that the accurate side information of the clustered CIR PDP can contribute a larger detection gain as compared to a conventional ED.

Therefore, energy of the UWB signal in each half of a frame is weighted using the PDP of the channel and is expressed as

$$\begin{aligned}\mathcal{E}_{n,k,0}^W &= \int_0^{T_f/2} h_{\text{pdp}}(t) r_{n,k,0}^2(t) dt \\ \mathcal{E}_{n,k,1}^W &= \int_{T_f/2}^{T_f} h_{\text{pdp}}(t) r_{n,k,1}^2(t) dt,\end{aligned}\tag{5.49}$$

where $h_{\text{pdp}}(t)$ is the exponentially decreasing channel amplitude envelope. Hence, the large amplitude signal gets more contribution in the energy calculation in (5.49). In a practical implementation, $h_{\text{pdp}}(t)$ can be derived using the small sub-intervals (bins) based signal energy computation and hence, (5.49) will be expressed as

$$\begin{aligned}\mathcal{E}_{n,k,0}^W &= \sum_{\iota=1}^M \mathcal{W}_\iota E_{\iota,0} \\ \mathcal{E}_{n,k,1}^W &= \sum_{\iota=1}^M \mathcal{W}_\iota E_{\iota,1},\end{aligned}\tag{5.50}$$

where M is the total number of bins in each half frame duration. \mathcal{W}_ι and $E_{\iota,z}$, $z = 0, 1$ are the weight and energy of ι^{th} bin, respectively. The $E_{\iota,z}$ is expressed as $E_{\iota,z} = \int_0^{T_f/M} r_{\iota,n,k,z}^2(t) dt$ with $r_{\iota,n,k,z}(t) = r_{n,k,z}(t - \iota T_f/M)$. The weight \mathcal{W}_ι can be calculated using the energy difference between the first and the second halves' signals in a frame and is written as

$$\mathcal{W}_\iota = |E_{\iota,0} - E_{\iota,1}|, \quad \iota = 1, 2, \dots, M.\tag{5.51}$$

In (5.51), noise contribution is subtracted since noise is equally distributed across a frame. Therefore, weights are calculated according to the channel PDP. Hence, no training or a priori information is required to estimate the weight coefficient \mathcal{W}_ι for the proposed ED-based fusion.

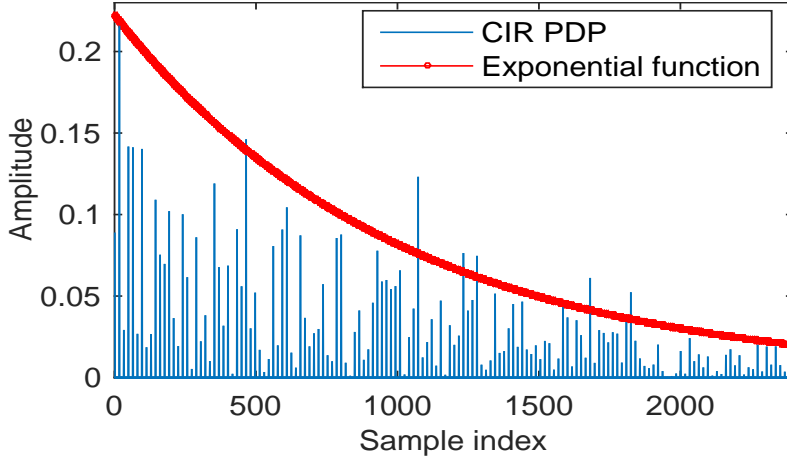


Figure 5.2: Amplitude envelope of UWB multipath channel.

5.4.2 Noise hardening

Noise is the main cause of ED's performance deterioration in WSN. The noise level is minimized in decision variable at an antenna (as shown in (5.36)) using the proposed BPPM UWB signaling. However, the small fluctuations of noise's variance in the first and the second halves of a frame leads to errors in the hypothesis estimation at the FC. Therefore, improvement in ED's performance could be achieved if the energy estimates of noise were as close to their average values as possible. Hence, the noise effect in the decision variable \mathcal{E} is minimized by using the average of noise variance over a block length.

Let $\zeta_{n,k,0} = [\mathcal{E}_{n,k,0}^1, \mathcal{E}_{n,k,0}^2, \dots, \mathcal{E}_{n,k,0}^{N_b}]^T \in \mathbb{R}^{N_b}$ and $\zeta_{n,k,1} = [\mathcal{E}_{n,k,1}^1, \mathcal{E}_{n,k,1}^2, \dots, \mathcal{E}_{n,k,1}^{N_b}]^T \in \mathbb{R}^{N_b}$ be the received signal energy in the first and second halves, respectively, for k^{th} sensor and n^{th} antenna link for a block length N_b . The two-time index vectors \mathbf{I}_1 and \mathbf{I}_2 are generated from $\zeta_{n,k,0}$ and $\zeta_{n,k,1}$ as:

$$\begin{aligned} \mathbf{I}_1 &= \{\mathbf{I}_1 \cup \{i\} \text{ if } \mathcal{E}_{n,k,0}^i \geq \mathcal{E}_{n,k,1}^i, i = 1, 2, \dots, N_b, \\ \mathbf{I}_2 &= \{\mathbf{I}_2 \cup \{i\} \text{ if } \mathcal{E}_{n,k,0}^i < \mathcal{E}_{n,k,1}^i, i = 1, 2, \dots, N_b. \end{aligned} \quad (5.52)$$

Initially, \mathbf{I}_1 and \mathbf{I}_2 are considered to be empty sets. The index vectors \mathbf{I}_1 and \mathbf{I}_2 correspond to the $d_m = 0$ and $d_m = 1$, respectively. Let $Z_1 = |\mathbf{I}_1|$ and $Z_2 = |\mathbf{I}_2|$ denote the cardinality of index vectors that depends on the element values of the

vectors $\zeta_{n,k,0}$ and $\zeta_{n,k,1}$. The two new variables are generated as

$$\begin{aligned}\Omega_{\text{noise}} &= \frac{1}{Z_1} \sum_{z_1=0}^{Z_1-1} \mathcal{E}_{n,k,1}^{\mathbf{I}_1(z_1)} + \frac{1}{Z_2} \sum_{z_2=0}^{Z_2-1} \mathcal{E}_{n,k,0}^{\mathbf{I}_2(z_2)}, \\ \Omega_{\text{sig-noise}} &= \frac{1}{Z_1} \sum_{z_1=0}^{Z_1-1} \mathcal{E}_{n,k,0}^{\mathbf{I}_1(z_1)} + \frac{1}{Z_2} \sum_{z_2=0}^{Z_2-1} \mathcal{E}_{n,k,1}^{\mathbf{I}_2(z_2)}.\end{aligned}\tag{5.53}$$

Therefore, noise and signal power can be estimated as Ω_{noise} and $\Omega_{\text{sig}} = \Omega_{\text{sig-noise}} - \Omega_{\text{noise}}$, respectively. For a large value of N_b , $\Omega_{\text{noise}} \approx \sigma_{z_0}^2$ and referred as noise hardening⁹. Further, the decision variable for k^{th} sensor and n^{th} antenna link in a frame is expressed as

$$\mathcal{E}_{n,k}^{\text{harding}} = \frac{\Omega_{\text{sig}}}{\Omega_{\text{noise}}} [(\mathcal{E}_{n,k,0} - \Omega_{\text{noise}}) - (\mathcal{E}_{n,k,1} - \Omega_{\text{noise}})]\tag{5.54}$$

Hence, in (5.54), noise variance is subtracted and the decision variable is weighted using the SNR. Next, the combined decision variable of all the sensors and antennas is calculated as similar in (5.31) and (5.32) by replacing $\mathcal{E}_{n,k}^{\text{harding}} = \mathcal{E}_{n,k,0} - \mathcal{E}_{n,k,1}$.

5.4.3 Sensor nodes' power optimization

In the WSN, some sensors are close to the FC and have better SNR than the relatively far sensors. Similarly, some sensors have better local performance (higher p_d and lower p_f) than the others in the system. Moreover, every link (between k^{th} sensor and n^{th} antenna) has a different SNR at the FC and that this average SNR is known for each sensor, we optimize the energy by selecting the sensing nodes of higher SNR. Therefore, the global detection error probability \mathcal{P}_E can be minimized by optimizing the system power among the sensor nodes. Since \mathcal{P}_E is the function of transmitted power (also referred as channel quality in the literature), the power

⁹Let $\Gamma = \|n(t)\|_2^2 / \mathbb{E}\{\|n(t)\|_2^2\}$ be the ratio between the instantaneous noise power and its average. If the fluctuations of the ratio Γ are small, then there is noise hardening.

optimization in the WSN can be written as

$$\begin{aligned}
 P_k^* &= \arg \max_{\mathbf{P}} \mathcal{P}_E, \\
 \text{subject to } & \sum_{k=1}^K P_k \leq \mathcal{E}_{\text{sys}} \quad P_k \geq 0 \quad \forall k
 \end{aligned} \tag{5.55}$$

where $\mathbf{P} = [P_1, P_1, \dots, P_K]^T$. Since (5.55) is difficult to solve and there is no closed form solution, hence, the numerical solution is used in this work.

5.5 Numerical results and discussion

In this section, simulation results are presented and insights are drawn for the proposed UWB based WSN system. Simulation results are also verified using the semi-analytical results. The second derivative Gaussian pulse $w(t)$ of duration $T_w \approx 0.8\text{ns}$ is used by the sensor nodes for transmission. Each sensor reading (presence or absence of the event) is transmitted using single pulse per frame with employing single frame per data symbol ($N_f = 1$) for simulation ease. The TH code $\{c_j^k\}$ is generated using chip duration $T_c = 1$ ns, cardinality $N_h = 20$, and period $N_p = 100$. In simulations, the standardized IEEE 802.15.4a multipath channels [6, 92] are used. $P_k = 1 \quad \forall k$ and sampling frequency of 16 GHz are considered. Further, SNR represents the link SNR in the numerical analysis, and all the sensor nodes are quasi-synchronized.

In the simulations, each sensor is considered to have equal probability of local false alarm (p_f) and the probability of detection (p_d). The global probabilities of false alarm (\mathcal{P}_F), detection (\mathcal{P}_D) and error probability \mathcal{P}_E are calculated at the FC. Performance of event's presence or absence estimation at FC (apart from the noisy reporting link) is also limited by sensors' quality, the number of sensor nodes and antennas and hence, needs to be studied in WSN. If the detection performance at FC is considered using observations in the noiseless MAC link, it is referred to as (upper) "observation bound" [109]. The observation bound using uniform performance of

all sensors can be written as

$$\begin{aligned}\mathcal{P}_{D,O} &= \sum_{l=\kappa}^K \binom{K}{l} p_d^l (1-p_d)^{K-l} \\ \mathcal{P}_{F,O} &= \sum_{l=\kappa}^K \binom{K}{l} p_f^l (1-p_f)^{K-l}\end{aligned}\tag{5.56}$$

where $\kappa \in \{1, 2, \dots, K\}$ is a discrete threshold. In simulations, perfect sensors ($p_f = 0$ and $p_d = 1$) are used.

5.5.1 Coherent detection at FC

The CD-based fusion rule is studied in a UWB based WSN. The average global detection error probability \mathcal{P}_E at FC using the CD is shown in Figure 5.3. The CD's \mathcal{P}_E performance over IEEE 802.15.4a multipath CM1 and CM4 channels¹⁰[6, 92] using multiple sensor nodes and the single antenna at FC is shown in Figure 5.3. The frame duration $T_f = 100$ ns and $T_f = 150$ ns are used for CM1 and CM4 channels, respectively, with pulse shift parameter $\Delta = 2$ ns in the CD. As the number of sensor nodes increases in the UWB sensor network, detection error performance improves as observed in Figure 5.3. The gain obtained using the number of sensor nodes in CD can be expressed as $\text{SNR}_{\text{gain}} \approx 10 \log_{10}(K)$ dB. For example, $K = 10$, $\text{SNR}_{\text{gain}} = 10$ dB, and the same is observed in Figure 5.3 for both CM1 and CM4 channels. However, performance improvement using more number of sensor nodes obtained with increased system power and communication resources.

Further, impact of both the number of sensors and antennas on the average \mathcal{P}_E in CD is shown in Figure 5.4 in CM1 channel. The SNR gain using sensors and antennas is expressed as $\text{SNR}_{\text{gain}} = 10 \log_{10}(NK)$ dB at fixed \mathcal{P}_E . Therefore, SNR gain can be obtained in the WSN using more number of antennas at FC for fixed sensor nodes. Thus, the CD-based fusion \mathcal{P}_E performance is benefitted logarithmically ($\text{SNR}_{\text{gain}} \propto \log_{10}(NK)$) using the number of sensors and antennas at FC. However,

¹⁰The LOS in indoor residential and the NLOS in office wireless communication environment is referred as IEEE 802.15.4a CM1 and CM4 respectively [6, 92].

CD needs CIR for each link, which may not be feasible for large value of K and N in the UWB based WSN system [92]. Numerical results are validated against the analytical results as shown in Figure 5.3 and Figure 5.4.

Next, simulation results are presented for ED-based fusion for the proposed UWB sensor networks and henceforth only ED's performance is studied due to its suitability for the WSN system.

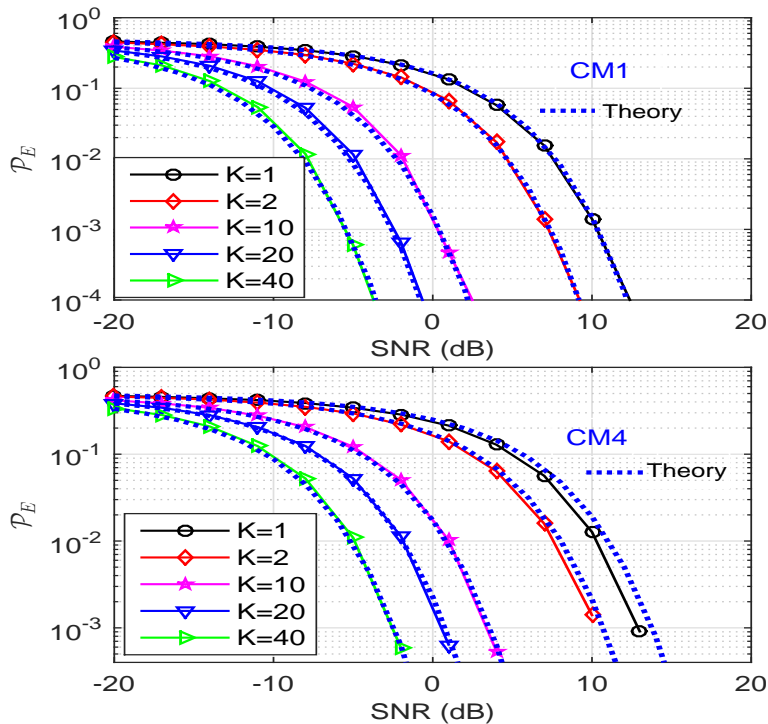


Figure 5.3: Average detection error probability \mathcal{P}_E performance using the CD at FC in IEEE 802.15.4a multipath CM1 (“top”) and CM4 (“bottom”) channels for various number of sensor nodes in the network.

5.5.2 Energy based detection

The ED-based fusion at FC is used for simple UWB based WSN s and impact of various system parameters such as the number of sensors and antennas are analyzed. In ED-based numerical simulations, frame duration $T_f = 200$ ns, $\Delta = 100$ ns, and integration interval $T_f/2$ are used.

The average global detection error probability \mathcal{P}_E of event Θ detection using varying number of sensor nodes and single antenna is shown in Figure 5.5. As the number of sensors increase, \mathcal{P}_E reduces as observed in Figure 5.5. The SNR gain

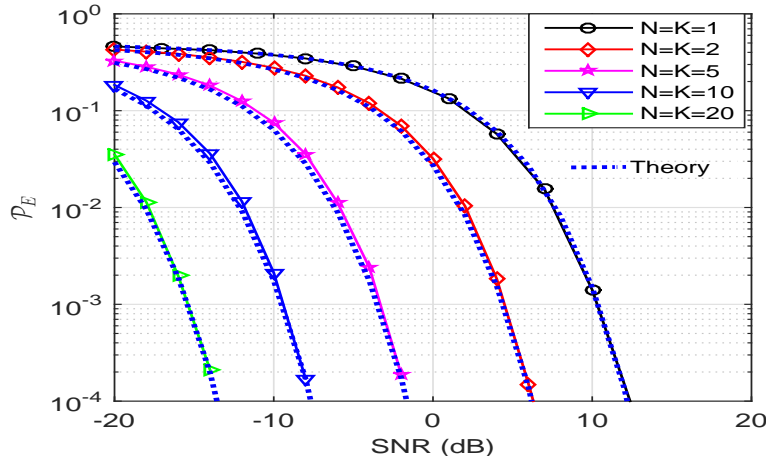


Figure 5.4: Average \mathcal{P}_E performance using the CD-based fusion in IEEE 802.15.4a multipath CM1 channel for various number of sensor nodes and antennas at FC.

obtained by using more number of sensors in ED is $\text{SNR}_{\text{gain,ed}} \approx 10 \log_{10} \sqrt{K}$ dB at fixed \mathcal{P}_E . In order to assess the sensitivity with respect to the number of sensor nodes, it is worth noticing that moving from $K = 1$ to $K = 40$ at $\mathcal{P}_E = 10^{-2}$, SNR requirement reduces from 20 dB to 12 dB. Therefore, use of large K in the network decreases either the SNR requirement or value of \mathcal{P}_E as observed in Figure 5.5.

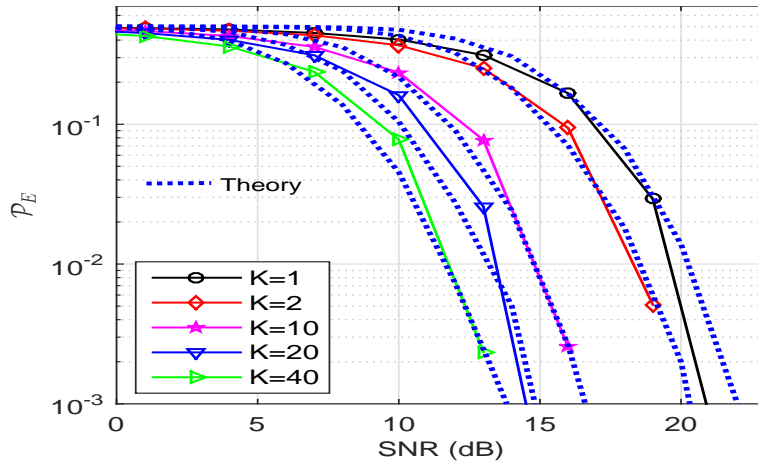


Figure 5.5: Average detection error probability \mathcal{P}_E of event detection at FC using ED-based fusion in CM1 channel for the various number of sensor nodes K .

The ED's performance can be ameliorated using the processing gain obtained by the large number of antennas at FC. The noise level can be reduced to arbitrary close to zero in the decision variable \mathcal{E} using massive antennas at the FC. The conditional PDF of decision variable (energy of each half in a frame) for a given data symbol $f(\mathcal{E}|d = 0)$ is shown in the Figure 5.6. In Figure 5.6, $K = 2$ and UWB multipath

CM1 channel are used. From Figure 5.6, one can observe that the PDF of each half signal energy is easily distinguishable with the increase in the number of antennas. Therefore, MAAs reduce the noise level in the proposed ED-based UWB sensor network.

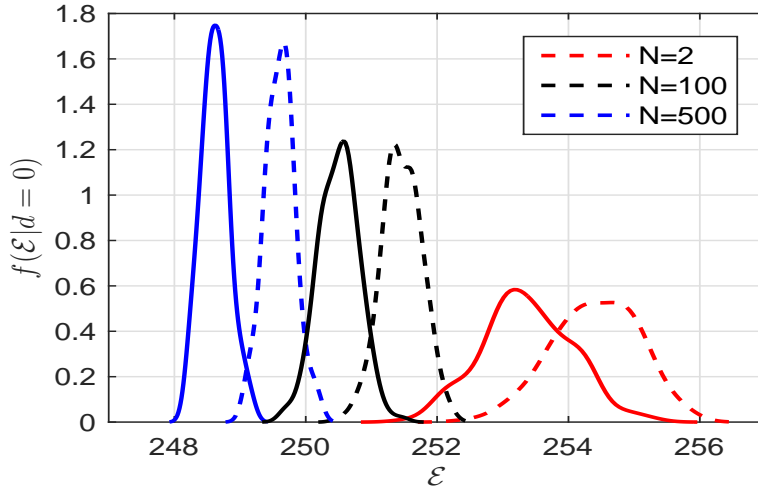


Figure 5.6: Impact of N on the conditional PDF $f(\mathcal{E}|d=0)$ at fixed value of $K=2$. The dashed and solid lines represent the PDF of first and second halves signal energy \mathcal{E}_0 and \mathcal{E}_1 in a frame respectively.

Detection Error Probability vs # of Links: The combined effect of the number of sensor nodes and antennas (referred as # of links) on the error probability \mathcal{P}_E is shown in Figure 5.7. As the number of links increase, \mathcal{P}_E decreases as observed in Figure 5.7. The SNR gain by increasing number of links in the system around $10 \log_{10}(\sqrt{NK})$ dB as observed in the Figure 5.7. Hence, a lower value of error probability can be achieved by increasing the number of antennas at FC with a moderate number of sensor nodes as observed in Figure 5.7. The effect of MAAs on \mathcal{P}_E is also evaluated. As $N \rightarrow \infty$ for fixed $K=2$, noise effect on \mathcal{P}_E approaches zero (See Figure 5.7). Therefore, a massive number of antennas at FC reduces the noise floor in the ED, which results in the ED's performance close to the CD, albeit with no apriori CIR, and accurate synchronization.

Global False Alarm and Detection Probabilities: The impact of the number of sensor nodes K on the global false alarm and detection probabilities are shown in Figure 5.8 using a single antenna $N=1$ at FC. It is observed that the performance of \mathcal{P}_D and \mathcal{P}_F improves as the SNR and the number of sensors increase. With a large

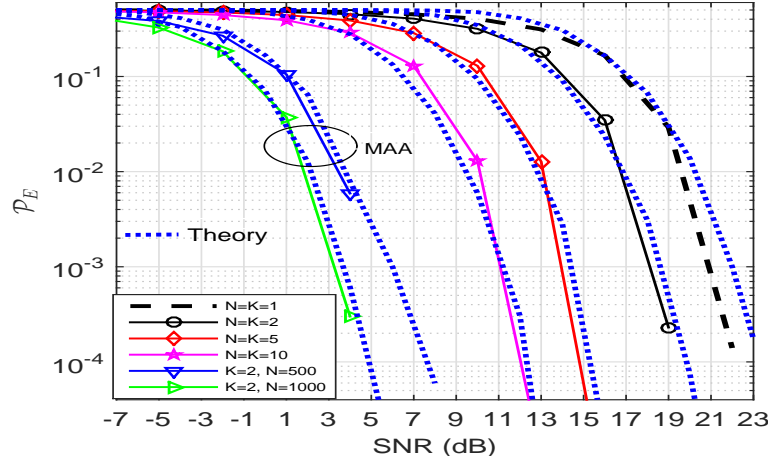


Figure 5.7: Average error probability \mathcal{P}_E performance using the various number of links (KN) in the sensor network.

number of sensors ($K = 40$), \mathcal{P}_D is high even at low SNR as observed in Figure 5.8 (bottom). Further, \mathcal{P}_F is also very low ($\approx 10^{-3}$) at SNR = 10 dB with a large number of sensor nodes ($K = 100$) as shown in Figure 5.8 (top).

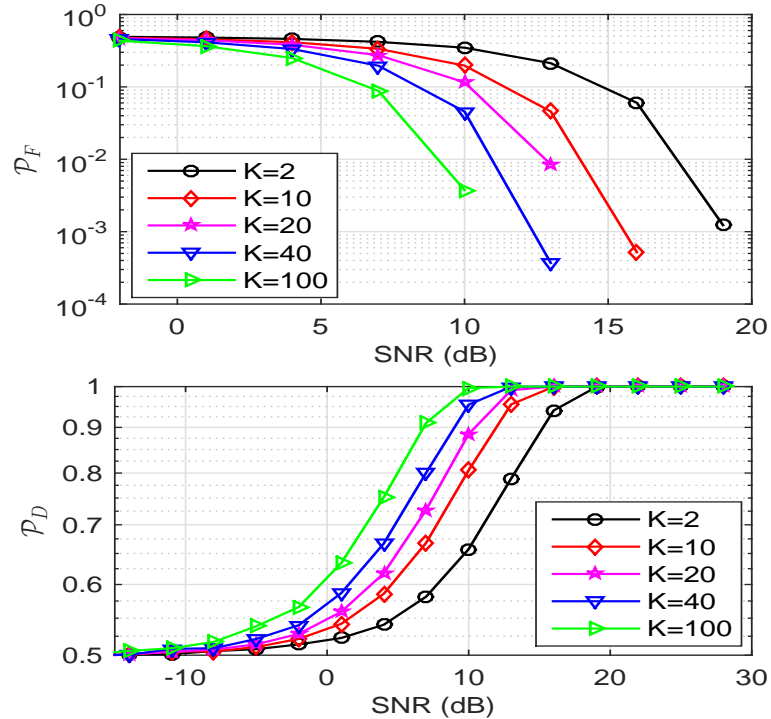


Figure 5.8: Average false alarm \mathcal{P}_F and detection \mathcal{P}_D probabilities using various number of sensors (K) with $\Upsilon_{ED} = 0$ in the WSN system.

Impact of Channel PDP: In Figure 5.9, the effect of signal energy optimization in a frame on the \mathcal{P}_E is shown. The number of bins in each half frame duration $M = 5, 10, 20$ are considered in (5.50). The weighted energy based fusion using

(5.51) by considering apriori information of the channel PDP can give SNR gain of approximately 3 dB at $\mathcal{P}_E = 10^{-3}$ as compared to a conventional ED as observed in Figure 5.9. Further, the number of bins $M = 10$ and $M = 20$ have almost equal \mathcal{P}_E performance.

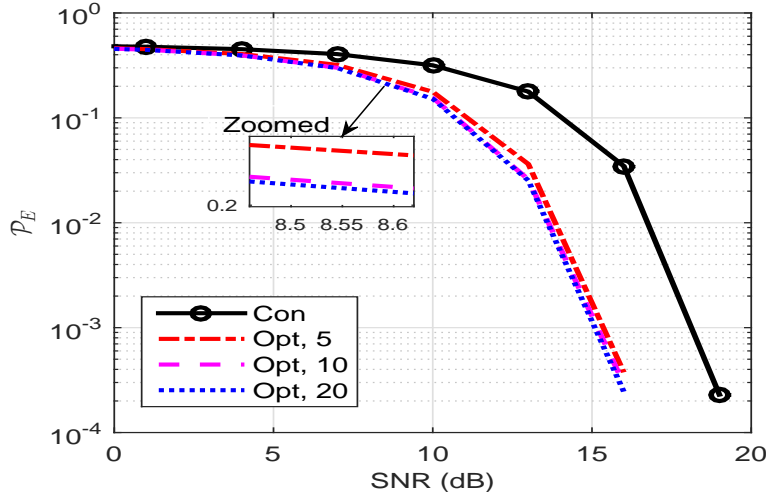


Figure 5.9: Average detection error probability using signal energy optimization at $K = 2$ and $N = 2$. The “Con” and “Opt” denote the conventional ED and the proposed energy optimization in (5.50) respectively.

Observation Bound: The effect of number of antennas N and SNR on \mathcal{P}_D is shown in Figure 5.10. For comparison, the “observation bound” of \mathcal{P}_D is reported, which is obtained using local detection probability $p_d = 0.5$ of each sensor with $K = 10$ and $\kappa = 2$. As the number of antennas increases for fixed SNR, \mathcal{P}_D approaches close to the observation bound as observed in Figure 5.10. Therefore, using the MAAs at FC, an arbitrary high detection probability of ED-based fusion at low SNR can be achieved. The maximum value of \mathcal{P}_D is limited by the observation bound as shown in Figure 5.10. Since observation bound on \mathcal{P}_D uses the noise-free reporting channel while considering the sensors’ local performance.

Impact of Integration Interval: The effect of the integration interval T_{int} on the error probability \mathcal{P}_E is shown in Figure 5.11 at $K = 2$ and $N = 2$. For $T_{\text{int}} = 10$ ns, the SNR improvement is around 3 dB at $\mathcal{P}_E = 10^{-3}$ as compared to $T_{\text{int}} = 100$ ns as observed in Figure 5.11. The received UWB signal has signal plus noise and noise only region, since the UWB channel is cluster sparse [92]. Further, UWB signal energy does not distribute uniformly in a frame. Therefore, optimal integration

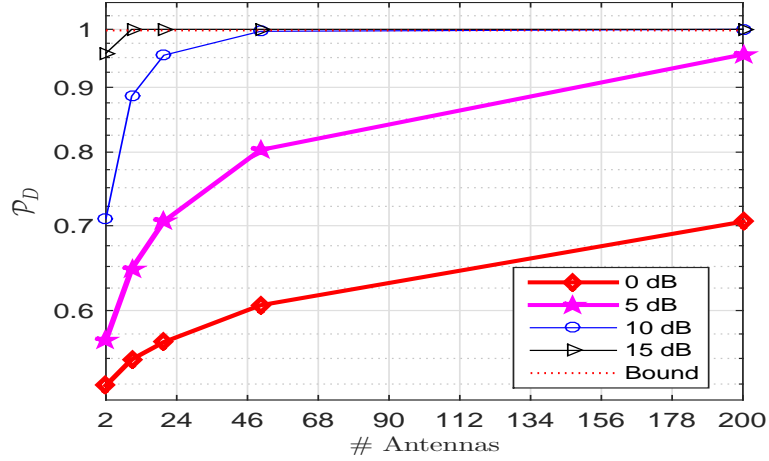


Figure 5.10: Global detection probability \mathcal{P}_D performance at $\Upsilon_{ED} = 0$ and SNR = 0, 5, 10, 15 dB, and it is also compared with observation bound (“Bound”). The observation bound is obtained using $K = 10$ and $\kappa = 2$.

interval can provide improved system performance as compared to the whole frame duration integration interval. The integration interval optimization for ED-based fusion at FC is expressed as

$$T_{\text{int,opt}} = \max_{T_{\text{int}} \in T_{\text{f}}/2} \{|\mathcal{E}_{n,k,0} - \mathcal{E}_{n,k,1}|\}. \quad (5.57)$$

Although closed-form expression for $T_{\text{int,opt}}$ is difficult to get, $T_{\text{int,opt}}$ can be obtained by dividing each half of a frame duration into small subintervals (bins) and adding those bins duration where signal plus noise bins’ energy is higher than the noise only bins’ energy, i.e., $T_{\text{int,opt}} = ZT_{\text{B}}$, where Z is the number of bins whose energy is higher than the noise energy and T_{B} is a bin’s time duration.

Effect of Noise Hardening: The \mathcal{P}_E performance improvement using the noise hardening (5.54) for the various K and $N = 1$ is shown in the Figure 5.12. The gain using the noise hardening (dashed lines) is around from 0.7 dB to 1 dB at $\mathcal{P}_E = 10^{-3}$ as observed in Figure 5.12. Further, the noise hardening does not require any additional implementation complexity (due to the non-existence of multiplication and division operations) except for few memory bytes as mentioned in the subsection 5.4.2. Moreover, noise hardening is also free from a training process or apriori knowledge of the sensor system such as signal and noise statistics.

Impact of Power Optimization: The impact of the power optimization in the system

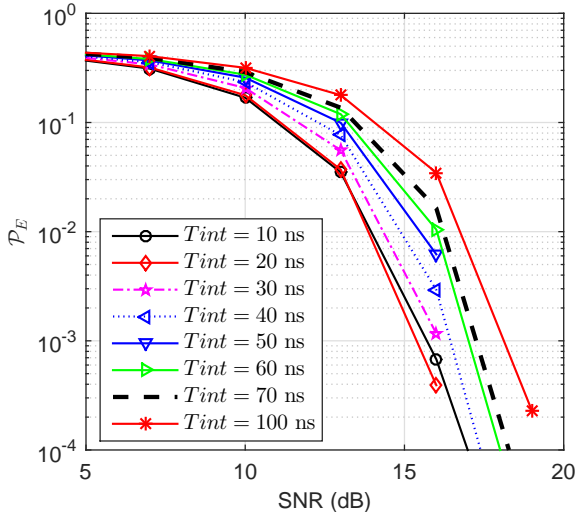


Figure 5.11: Impact of integration interval T_{int} on the \mathcal{P}_E .

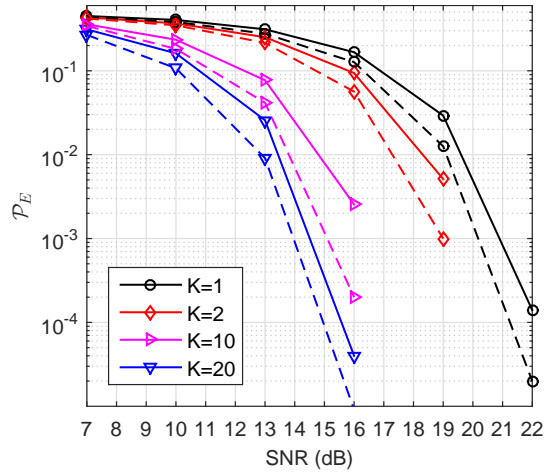


Figure 5.12: Effect of noise hardening on \mathcal{P}_E performance using the various K and the single antenna.

on \mathcal{P}_E is shown in Figure 5.13. The SNR gain is approximately 2 dB at $\mathcal{P}_E = 10^{-3}$ as observed in Figure 5.13. The higher power is assigned to those sensors whose CIR is better in the system while keeping total power of the system constant, i.e., \mathcal{E}_{sys} . Therefore, power optimization can be used to extend the battery life or communication range of the WSN.

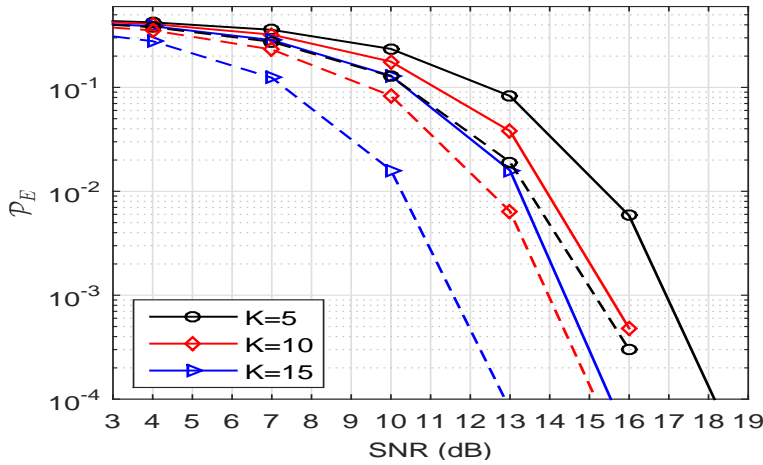


Figure 5.13: Impact of power optimization on \mathcal{P}_E performance using the various sensors and the single antenna in the WSN system. The solid and dashed lines denote the equal and optimized power respectively of the sensor nodes.

Therefore, tradeoff exists between system implementation complexity and performance for CD and ED-based fusion at FC. The ED is simple and more suitable in dynamic channel environment. Further, MAAs for the proposed WSN system provides large processing gain with marginal increment in system implementation

complexity. CD is preferable when CIR is static for a longer period and a small number of antennas at FC. Further, ED's performance can be enhanced using knowledge of various parameters such as noise hardening, integration interval, CIR's amplitude envelope, and MAAs at the FC. Fusion performance is the key of a WSN because it measures the conditions of the event or environment being monitored. Furthermore, the joint energy detection and a massive array design, with phase shifters and delay elements similar to [114], and timing synchronization error can be used to analyze the proposed sensor network performance in future.

5.6 Summary

A UWB system for WSN in massive MIMO decision fusion is proposed and analyzed in this chapter. The global detection, false alarm and error probabilities at the fusion center are derived and compared with simulation results. Both coherent and non-coherent (energy) detection based fusion methods are discussed for a sensor network. The CD-based fusion has optimal performance with very high implementation complexity. However, ED-based fusion is better due to its low computational complexity and limited requirements on system knowledge with sub-optimal performance for WSN. Further, the noise level is significantly reduced (close to zero) in the ED-based fusion using massive antenna arrays that results in a very high gain in the sensor network. Hence, the low error probability of event estimation can be achieved at very low SNR. Further, the impact of number of sensors, antennas, and various other system parameters are analyzed. The proposed system based on low power UWB technology can be used for precise localization in indoor and short-range scenarios such as picocell and femtocell networks in assisted living, body-to-body, and many 5G based IoT applications.

Chapter 6

Conclusion and Future Work

This thesis addressed some issues relevant for UWB communication systems. This chapter summarizes primary contributions and insights of the work addressed in this thesis, and proposes some directions for future research.

6.1 Summary of contribution

This thesis carried out extensive performance evaluation of low power and ultra wideband UWB system using the sparsity-based signal processing methods.

Firstly, a robust UWB receiver design is carried out that utilizes the received UWB signal cluster sparsity characteristics to mitigate IN. The proposed cluster detection algorithm-based receiver's BER performance is theoretically analyzed and compared with some popular existing non-linear receivers in the presence of IN over standardized IEEE 802.15.4a channel models.

Next, the sparsity of the UWB signal is used to remove the NBI effect in the coherent receiver. Since both NBI and UWB signals are sparse in time and frequency domains, respectively, the proposed NBI mitigation method exploits distinct characteristics of UWB signals and NBI, and does not require a nonlinear operator such as a limiter or a blanker. Improved performance of the proposed coherent receiver has been validated in both AWGN and multipath fading channels in the presence of NBI.

Further, to reduce the sampling rate, to have precise synchronization, and for low power requirement, UWB systems are implemented using compressive or sub-Nyquist rate measured samples by exploiting sparsity of the UWB signal. A (partially) deterministic UWB waveform-matched measurement matrix is proposed. The proposed measurement matrix has circulant structure and is sparse in nature. The proposed matrix is easy to implement in hardware and is operationally time efficient as needed in a practical system. Improved BER performance with reduced implementation complexity is observed with the use of the proposed measurement matrix as compared to the existing measurement matrices.

Finally, UWB-based WSN using MAAs at fusion center for distributed detection is proposed and analyzed. Both the coherent and energy based fusion rules are considered for the proposed WSN over multiple access channels. The trade-off between the performance and the implementation complexity of the coherent and energy based fusion is studied. Further, it is shown that MAAs at fusion center and various levels of channel knowledge can enhance the performance of the energy-based detector in UWB sensor network with simple system design. Impact of various design parameters such as the number of sensors, receiver antennas, sensor quality, and integration interval on the WSN system's performance are also examined.

6.2 Future work

Sparsity-based signal processing is an emerging research area in the wireless communications. In line with this, all the algorithms and systems developed in this thesis work are novel approaches to improve the throughput of UWB link. The high-frequency communication schemes such as mmWave and terahertz (THz) channels are time sparse. Thus, the work covered in this thesis, based on channel sparsity, can be helpful for high-frequency communication schemes to reduce the receiver complexity and to enhance system performance for next-generation communication networks. The work of this thesis can be extended for THz communication, since

both the UWB and THz are pulse-based communications and are suitable for short range.

Further, the co-channel interference, pulse distortion during transmission and imperfect channels estimation can also be considered in the system model to investigate their effects on the UWB system's performance. Furthermore, detection performance of non-coherent UWB receiver discussed in this thesis can be analyzed in the presence of NBI and IN environments and to propose new methods for further improvements

The impact of finite resolution-based ADC on the discussed UWB coherent and non-coherent receivers can be analyzed. Since finite resolution (e.g.1-bit) ADC have low power consumption and high sampling rate, this would result in simple hardware system implementation.

Lastly, UWB is a potential technology for wearable and implantable biomedical devices due to low power and wideband width. Thus, the proposed methods in this thesis can be analyzed for the WBAN using IEEE 802.15.6 standard.

References

- [1] A. Nordrum, “Popular internet of things forecast of 50 billion devices by 2020 is outdated,” *IEEE Spectrum*, vol. 18, 2016.
- [2] A. Yassin, Y. Nasser, M. Awad, A. Al-Dubai, R. Liu, C. Yuen, R. Raulefs, and E. Aboutanios, “Recent advances in indoor localization: A survey on theoretical approaches and applications,” *IEEE Communications Surveys and Tutorials*, vol. 19, no. 2, pp. 1327–1346, 2016.
- [3] Z. Yin, X. Jiang, Z. Yang, N. Zhao, and Y. Chen, “WUB-IP: A high-precision UWB positioning scheme for indoor multiuser applications,” *IEEE Systems Journal*, vol. PP, no. 99, pp. 1–10, 2017.
- [4] Z. Chen, Y. Liu, S. Li, and G. Wang, “Study on the multipath propagation characteristics of UWB signal for indoor lab environments,” in *IEEE International Conference on Ubiquitous Wireless Broadband (ICUWB)*, 2016, pp. 1–4.
- [5] J. Blumenstein, A. Prokes, A. Chandra, T. Mikulasek, R. Marsalek, T. Zemen, and C. Mecklenbräuker, “In-vehicle channel measurement, characterization, and spatial consistency comparison of 3-11 GHz and 55-65 GHz frequency bands,” *IEEE Transactions on Vehicular Technology*, vol. 66, no. 5, pp. 3526–3537, 2017.
- [6] A. F. Molisch, D. Cassioli, C.-C. Chong, S. Emami, A. Fort, B. Kannan, J. Karedal, J. Kunisch, H. G. Schantz, K. Siwiak *et al.*, “A comprehensive

- standardized model for ultrawideband propagation channels,” *IEEE Transactions on Antennas and Propagation*, vol. 54, no. 11, pp. 3151–3166, 2006.
- [7] C. Park and T. S. Rappaport, “Short-range wireless communications for next-generation networks: UWB, 60 GHz millimeter-wave WPAN, and ZigBee,” *IEEE Wireless Communications*, vol. 14, no. 4, 2007.
- [8] V. P. Yajnanarayana, “Ultra Wideband: Communication and Localization,” Ph.D. dissertation, KTH Royal Institute of Technology, 2017.
- [9] M. Cavallaro, T. Copani, and G. Palmisano, “A Gaussian pulse generator for millimeter-wave applications,” *IEEE Transactions on Circuits and Systems I: Regular Papers*, vol. 57, no. 6, pp. 1212–1220, 2010.
- [10] V. Savic, J. Ferrer-Coll, P. Ängskog, J. Chilo, P. Stenumgaard, and E. G. Larsson, “Measurement analysis and channel modeling for TOA-based ranging in tunnels,” *IEEE Transactions on Wireless Communications*, vol. 14, no. 1, pp. 456–467, 2015.
- [11] I. B. Mabrouk, L. Talbi, M. Nedil, and K. Hettak, “MIMO-UWB channel characterization within an underground mine gallery,” *IEEE Transactions on Antennas and Propagation*, vol. 60, no. 10, pp. 4866–4874, 2012.
- [12] V. Niemelä, J. Haapola, M. Hämäläinen, and J. Iinatti, “An ultra wideband survey: Global regulations and impulse radio research based on standards,” *IEEE Communications Surveys and Tutorials*, vol. 19, no. 2, pp. 874–890, 2017.
- [13] A. Schenk, “Coding, Modulation, and Detection for Impulse-Radio Ultra-Wideband Communications,” Ph.D. dissertation, University of Erlangen-Nuremberg, 2013.
- [14] A. F. Molisch, K. Balakrishnan, D. Cassioli, C.-C. Chong, S. Emami, A. Fort, J. Karedal, J. Kunisch, H. Schantz, U. Schuster *et al.*, “IEEE 802.15.4a channel model-final report,” *IEEE P802*, vol. 15, no. 04, pp. 1–40, 2004.

- [15] E. Karapistoli, F.-N. Pavlidou, I. Gragopoulos, and I. Tsetsinas, “An overview of the IEEE 802.15. 4a standard,” *IEEE Communications Magazine*, vol. 48, no. 1, 2010.
- [16] S. Nagaraj and F. G. Rassam, “Improved noncoherent UWB receiver for implantable biomedical devices,” *IEEE Transactions on Biomedical Engineering*, vol. 63, no. 10, pp. 2220–2225, 2016.
- [17] M. S. Mohammadi, E. Dutkiewicz, Q. Zhang, and X. Huang, “Optimal energy efficiency link adaptation in IEEE 802.15. 6 IR-UWB body area networks,” *IEEE Communications Letters*, vol. 18, no. 12, pp. 2193–2196, 2014.
- [18] E. Schires, P. Georgiou, and T. S. Lande, “Vital sign monitoring through the back using an UWB impulse radar with body coupled antennas,” *IEEE Transactions on Biomedical Circuits and Systems*, 2018.
- [19] M. Ghavami, L. B. Michael, and R. Kohno, *Ultra Wideband Signals and Systems in Communication Engineering*. John Wiley and Sons, West Sussex, 2004.
- [20] Z. Bai, J. Liu, and H.-H. Chen, “Design of ultra-wideband pulses based on spectrum shifted Gaussian waveforms,” *IET Communications*, vol. 7, no. 6, pp. 512–520, 2013.
- [21] J. A. Silva and M. L. De Campos, “Spectrally efficient UWB pulse shaping with application in orthogonal PSM,” *IEEE Transactions on Communications*, vol. 55, no. 2, pp. 313–322, 2007.
- [22] X. Wu, Z. Tian, T. N. Davidson, and G. B. Giannakis, “Optimal waveform design for UWB radios,” *IEEE Transactions on Signal Processing*, vol. 54, no. 6, pp. 2009–2021, 2006.
- [23] C. Yang, L. Xia, S. Fu, and D. Liu, “Reconfigurable UWB pulse generation based on multi-taps and a programmable filter,” *IEEE Photonics Technology Letters*, vol. 26, no. 14, pp. 1395–1398, 2014.

- [24] M. G. D. Benedetto and G. Giancola, *Understanding ultra wide band radio fundamentals*. Prentice Hall PTR, 2004.
- [25] N. C. Beaulieu and B. Hu, “On determining a best pulse shape for multiple access ultra-wideband communication systems,” *IEEE Transactions on Wireless Communications*, vol. 7, no. 9, pp. 3589–3596, 2008.
- [26] —, “A pulse design paradigm for ultra-wideband communication systems,” *IEEE Transactions on Wireless Communications*, vol. 5, no. 6, pp. 1274–1278, 2006.
- [27] H. Stark, Y. Yang, and Y. Yang, *Vector space projections: a numerical approach to signal and image processing, neural nets, and optics*. John Wiley and Sons, Inc., 1998.
- [28] S. Y. Lee, “Pulse shape design for ultra-wideband radios using projections onto convex sets,” *The Journal of Korean Institute of Communications and Information Sciences*, vol. 33, no. 3A, pp. 311–318, 2008.
- [29] A. Ranganathan and S. Capkun, “Are we really close? verifying proximity in wireless systems,” *IEEE Security and Privacy*, 2017.
- [30] S. Niranjayan and N. C. Beaulieu, “Novel adaptive nonlinear receivers for UWB multiple access communications,” *IEEE Transactions on Wireless Communications*, vol. 12, no. 5, pp. 2014–2023, 2013.
- [31] B. S. Kim, J. Bae, I. Song, S. Y. Kim, and H. Kwon, “A comparative analysis of optimum and suboptimum rake receivers in impulsive UWB environment,” *IEEE Transactions on Vehicular Technology*, vol. 55, no. 6, pp. 1797–1804, 2006.
- [32] N. Güneş, H. Deliç, and M. Koca, “Robust detection of ultra-wideband signals in non-Gaussian noise,” *IEEE Transactions on Microwave Theory and Techniques*, vol. 54, no. 4, pp. 1724–1730, Apr. 2006.

- [33] H. Ding, W. Liu, X. Huang, and L. Zheng, “First path detection using rank test in IR UWB ranging with energy detection receiver under harsh environments,” *IEEE Communications Letters*, vol. 17, no. 4, pp. 761–764, 2013.
- [34] M. Cheffena, “Propagation channel characteristics of industrial wireless sensor networks [wireless corner],” *IEEE Antennas and Propagation Magazine*, vol. 58, no. 1, pp. 66–73, 2016.
- [35] S. Liu, F. Yang, W. Ding, and J. Song, “Double kill: Compressive-sensing-based narrow-band interference and impulsive noise mitigation for vehicular communications,” *IEEE Transactions on Vehicular Technology*, vol. 65, no. 7, pp. 5099–5109, 2016.
- [36] I. W. Selesnick, “A new sparsity-enabled signal separation method based on signal resonance,” in *IEEE International Conference on Acoustics Speech and Signal Processing (ICASSP)*, 2010, pp. 4150–4153.
- [37] R. Barazideh, B. Natarajan, A. V. Nikitin, and R. L. Davidchack, “Performance of analog nonlinear filtering for impulsive noise mitigation in OFDM-based PLC systems,” in *IEEE Latin-American Conference on Communications (LATINCOM)*. IEEE, 2017, pp. 1–6.
- [38] A. M. Tonello, “Wideband impulse modulation and receiver algorithms for multiuser power line communications,” *EURASIP Journal on Advances in Signal Processing*, vol. 2007, no. 1, pp. 1–14, 2007.
- [39] K. Khalil, P. Corlay, F.-X. Coudoux, M. G. Gzalet, and M. Gharbi, “Analysis of the impact of impulsive noise parameters on BER performance of OFDM power-line communications,” *arXiv preprint arXiv:1502.06821*, 2015.
- [40] V. Bhatia, B. Mulgrew, and A. T. Georgiadis, “Stochastic gradient algorithms for equalisation in α -stable noise,” *Elsevier Signal Processing*, vol. 86, no. 4, pp. 835–845, 2006.

- [41] A. Yang, Z. Xu, H. Nie, and Z. Chen, "On the variance-based detection for impulse radio UWB systems," *IEEE Transactions on Wireless Communications*, vol. 15, no. 12, pp. 8249–8259, 2016.
- [42] B. Silva and G. P. Hancke, "IR-UWB-based non-line-of-sight identification in harsh environments: Principles and challenges," *IEEE Transactions on Industrial Informatics*, vol. 12, no. 3, pp. 1188–1195, 2016.
- [43] F. H. Juwono, Q. Guo, D. Huang, Y. Chen, L. Xu, and K. P. Wong, "On the performance of blanking nonlinearity in real-valued OFDM-based PLC," *IEEE Transactions on Smart Grid*, vol. PP, no. 99, pp. 1–9, 2016, DOI:10.1109/TSG.2016.2606643.
- [44] P. Banelli, "Bayesian estimation of a Gaussian source in Middleton's class-A impulsive noise," *IEEE Signal Processing Letters*, vol. 20, no. 10, pp. 956–959, 2013.
- [45] U. Epple and M. Schnell, "Advanced blanking nonlinearity for mitigating impulsive interference in OFDM systems," *IEEE Transactions on Vehicular Technology*, vol. 66, no. 1, pp. 146–158, 2017.
- [46] Z. Wang, G. R. Arce, B. M. Sadler, J. L. Paredes, S. Hoyos, and Z. Yu, "Compressed UWB signal detection with narrowband interference mitigation," in *IEEE International Conference on Ultra-Wideband (ICUWB)*, vol. 2, Sep. 2008, pp. 157–160.
- [47] B. Jin, S. Zhang, J. Pan, and X. Lin, "Sub-Nyquist sampling based narrowband interference mitigation in UWB impulse radio," *Electronics Letters*, vol. 48, no. 15, pp. 963–964, 2012.
- [48] Z. Xu, H. Nie, Z. Chen, H. Khani, W. Xiang, and L. Yu, "On the nonlinear Teager-Kaiser operator for energy detection based impulse radio UWB receivers," *IEEE Transactions on Wireless Communications*, vol. 13, no. 5, pp. 2955–2965, 2014.

- [49] X. Cheng and Y. L. Guan, "Narrow-band interference suppression in impulse-radio ultrawideband systems," *IEEE Transactions on Vehicular Technology*, vol. 63, no. 7, pp. 3440–3446, 2014.
- [50] S. M. Ekome, G. Baudoin, M. Villegas, and J. Schwoerer, "Narrowband interference mitigation in UWB communication with energy detector," in *IEEE International Conference on Ultra-Wideband (ICUWB)*, 2012, pp. 67–71.
- [51] O. Abedi and M. C. Yagoub, "Efficient narrowband interference cancellation in ultra-wide-band rake receivers," *IET Communications*, vol. 7, no. 1, pp. 57–64, 2013.
- [52] H. Xiong, W. Zhang, Z. Du, B. He, and D. Yuan, "Front-end narrowband interference mitigation for DS-UWB receiver," *IEEE Transactions on Wireless Communications*, vol. 12, no. 9, pp. 4328–4337, 2013.
- [53] S. A. Alawsh and A. H. Muqaibel, "Compressive sensing for blind NBI mitigation in UWB systems," in *IEEE International Conference on Signal and Image Processing Applications (ICSIPA)*, 2013, pp. 441–446.
- [54] N. Chen, S. Wu, Y. Li, and B. Cao, "Compressed sensing enabled narrowband interference mitigation for IR-UWB systems," in *IEEE International Conference on Wireless Communications and Signal Processing (WCSP)*, 2013, pp. 1–5.
- [55] M. E. Khedr, A. El-Helw, and M. H. Afifi, "Adaptive mitigation of narrowband interference in impulse radio UWB systems using time-hopping sequence design," *Journal of Communications and Networks*, vol. 17, no. 6, pp. 622–633, 2015.
- [56] Z. Bai, S. Gao, S. Peng, and P. Dong, "Modified chirp waveforms-based OCC-UWB system with multiple interferences suppression," *IEEE Systems Journal*, vol. 12, no. 1, pp. 814–822, 2018.

- [57] A. E.-C. Tan and K. Rambabu, "Modeling the effects of interference suppression filters on ultra-wideband pulses," *IEEE Transactions on Microwave Theory and Techniques*, vol. 59, no. 1, pp. 93–98, 2011.
- [58] S. Foucart and H. Rauhut, *A Mathematical Introduction to Compressive Sensing*. Springer, 2013.
- [59] I. W. Selesnick, "A new sparsity-enabled signal separation method based on signal resonance," in *IEEE International Conference on Acoustics, Speech and Signal Processing (ICASSP)*, 2010, pp. 4150–4153.
- [60] J. Meng, J. Ahmadi-Shokouh, H. Li, E. J. Charlson, Z. Han, S. Noghianian, and E. Hossain, "Sampling rate reduction for 60 GHz UWB communication using compressive sensing," in *IEEE Conference on Signals, Systems and Computers*, 2009, pp. 1125–1129.
- [61] Z. Wang, G. R. Arce, J. L. Paredes, and B. M. Sadler, "Compressed detection for ultra-wideband impulse radio," in *IEEE 8th Workshop on Signal Processing Advances in Wireless Communications (SPAWC)*, 2007, pp. 1–5.
- [62] S. Gishkori, V. Lottici, and G. Leus, "Compressive sampling-based multiple symbol differential detection for UWB communications," *IEEE Transactions on Wireless Communications*, vol. 13, no. 7, pp. 3778–3790, Jul. 2014.
- [63] P. Zhang, Z. Hu, R. C. Qiu, and B. M. Sadler, "A compressed sensing based ultra-wideband communication system," in *IEEE International Conference on Communications (ICC)*, Jun. 2009, pp. 1–5.
- [64] N. T. Son, S. Guo, and H. Chen, "Impact of channel models on compressed sensing recovery algorithms-based ultra-wideband channel estimation," *IET Communications*, vol. 7, no. 13, pp. 1322–1330, 2013.
- [65] O. U. Khan, S.-Y. Chen, D. D. Wentzloff, and W. E. Stark, "Impact of compressed sensing with quantization on UWB receivers with multipath channel

- estimation,” *IEEE Journal on Emerging and Selected Topics in Circuits and Systems*, vol. 2, no. 3, pp. 460–469, 2012.
- [66] A. Oka and L. Lampe, “A compressed sensing receiver for bursty communication with UWB impulse radio,” in *IEEE International Conference on Ultra-Wideband (ICUWB)*. IEEE, 2009, pp. 279–284.
- [67] K. M. Cohen, C. Attias, B. Farbman, I. Tselniker, and Y. C. Eldar, “Channel estimation in UWB channels using compressed sensing,” in *IEEE International Conference on Acoustics, Speech and Signal Processing (ICASSP)*. IEEE, 2014, pp. 1966–1970.
- [68] A. H. Muqaibel and M. T. Alkhodary, “Practical application of compressive sensing to ultra-wideband channels,” *IET Communications*, vol. 6, no. 16, pp. 2534–2542, 2012.
- [69] W. Weidong, Y. Jun-an, Y. Haibo, and W. Shehui, “Reconstruction method for pulse position modulation ultra wideband communication signal based on compressed sensing,” *IET Communications*, vol. 8, no. 5, pp. 707–713, 2014.
- [70] G. Wunder, H. Boche, T. Strohmer, and P. Jung, “Sparse signal processing concepts for efficient 5G system design,” *IEEE Access*, vol. 3, pp. 195–208, 2015.
- [71] J. L. Paredes, G. R. Arce, and Z. Wang, “Ultra-wideband compressed sensing: channel estimation,” *IEEE Journal of Selected Topics in Signal Processing*, vol. 1, no. 3, pp. 383–395, Oct. 2007.
- [72] M. A. Davenport, P. T. Boufounos, M. B. Wakin, and R. G. Baraniuk, “Signal processing with compressive measurements,” *IEEE Journal of Selected Topics in Signal Processing*, vol. 4, no. 2, pp. 445–460, 2010.
- [73] H. Rauhut, J. Romberg, and J. A. Tropp, “Restricted isometries for partial random circulant matrices,” *Applied and Computational Harmonic Analysis*, vol. 32, no. 2, pp. 242–254, 2012.

- [74] R. Berinde and P. Indyk, “Sparse recovery using sparse random matrices,” *preprint*, 2008.
- [75] S. Li and G. Ge, “Deterministic sensing matrices arising from near orthogonal systems,” *IEEE Transactions on Information Theory*, vol. 60, no. 4, pp. 2291–2302, 2014.
- [76] W. Yin, S. Morgan, J. Yang, and Y. Zhang, “Practical compressive sensing with Toeplitz and circulant matrices,” in *Visual Communications and Image Processing*. International Society for Optics and Photonics, 2010.
- [77] S. Haghghatshoar, E. Abbe, and E. Telatar, “Adaptive sensing using deterministic partial Hadamard matrices,” in *IEEE International Symposium on Information Theory Proceedings (ISIT)*. IEEE, 2012, pp. 1842–1846.
- [78] K. Ni, S. Datta, P. Mahanti, S. Roudenko, and D. Cochran, “Efficient deterministic compressed sensing for images with chirps and Reed-Muller codes,” *SIAM Journal on Imaging Sciences*, vol. 4, no. 3, pp. 931–953, 2011.
- [79] H. Rauhut, “Circulant and Toeplitz matrices in compressed sensing,” *arXiv preprint arXiv:0902.4394*, 2009.
- [80] A. Ravelomanantsoa, H. Rabah, and A. Rouane, “Compressed sensing: A simple deterministic measurement matrix and a fast recovery algorithm,” *IEEE Transactions on Instrumentation and Measurement*, vol. 64, no. 12, pp. 3405–3413, 2015.
- [81] L. Baldassarre, Y.-H. Li, J. Scarlett, B. Gözcü, I. Bogunovic, and V. Cevher, “Learning-based compressive subsampling,” *arXiv preprint arXiv:1510.06188*, 2015.
- [82] M. F. Duarte and Y. C. Eldar, “Structured compressed sensing: From theory to applications,” *IEEE Transactions on Signal Processing*, vol. 59, no. 9, pp. 4053–4085, 2011.

- [83] K. Yan, H.-C. Wu, H. Xiao, and X. Zhang, “Novel measurement matrix optimization for source localization based on compressive sensing,” in *IEEE Global Communications Conference (GLOBECOM)*. IEEE, 2014, pp. 341–345.
- [84] B. Bouchhima, R. Amara, and M. T.-H. Alouane, “Design of optimal matrices for compressive sensing: Application to environmental sounds,” in *23rd European Signal Processing Conference (EUSIPCO)*. IEEE, 2015, pp. 130–134.
- [85] R. Shoitan, Z. Nossair, I. Isamil, and A. Tobal, “Hybrid wavelet measurement matrices for improving compressive imaging,” *Signal, Image and Video Processing*, pp. 1–8, 2016.
- [86] O. Abari, F. Lim, F. Chen, and V. Stojanovic, “Why analog-to-information converters suffer in high-bandwidth sparse signal applications,” *IEEE Transactions on Circuits and Systems I*, vol. 60, no. 9, pp. 2273–2284, 2013.
- [87] S. L. Shishkin, “Fast and robust compressive sensing method using mixed Hadamard sensing matrix,” *IEEE Journal on Emerging and Selected Topics in Circuits and Systems*, vol. 2, no. 3, pp. 353–361, 2012.
- [88] Z. Zhang, Y. Xu, J. Yang, X. Li, and D. Zhang, “A survey of sparse representation: algorithms and applications,” *IEEE Access*, vol. 3, pp. 490–530, 2015.
- [89] J. G. Proakis, *Digital Communications*. McGraw-Hill Education, 2007.
- [90] A. Bastounis and A. C. Hansen, “On the absence of the RIP in real-world applications of compressed sensing and the RIP in levels,” *arXiv preprint arXiv:1411.4449*, 2014.
- [91] E. J. Candes and Y. Plan, “A probabilistic and RIPless theory of compressed sensing,” *IEEE Transactions on Information Theory*, vol. 57, no. 11, pp. 7235–7254, 2011.

- [92] B. Li, C. Zhao, H. Zhang, X. Sun, and Z. Zhou, "Characterization on clustered propagations of UWB sensors in vehicle cabin: measurement, modeling and evaluation," *IEEE Sensors Journal*, vol. 13, no. 4, pp. 1288–1300, 2013.
- [93] J. Zhang, P. V. Orlik, Z. Sahinoglu, A. F. Molisch, and P. Kinney, "UWB systems for wireless sensor networks," *IEEE Proceedings*, vol. 97, no. 2, pp. 313–331, 2009.
- [94] C. Botteron, D. Briand, B. Mishra, G. Tasselli, P. Janphuang, F.-J. Haug, A. Skrivervik, R. Lockhart, C. Robert, N. F. de Rooij *et al.*, "A low-cost UWB sensor node powered by a piezoelectric harvester or solar cells," *Elsevier Sensors and Actuators A: Physical*, vol. 239, pp. 127–136, 2016.
- [95] F. Guidi, A. Sibille, C. Roblin, V. Casadei, and D. Dardari, "Analysis of UWB tag backscattering and its impact on the detection coverage," *IEEE Transactions on Antennas and Propagation*, vol. 62, no. 8, pp. 4292–4303, 2014.
- [96] N. Decarli, F. Guidi, and D. Dardari, "Passive UWB RFID for tag localization: Architectures and design," *IEEE Sensors Journal*, vol. 16, no. 5, pp. 1385–1397, 2016.
- [97] R. Tomasi, F. Sottile, C. Pastrone, M. M. Mozumdar, A. Osello, and L. Lavagno, "Leveraging BIM interoperability for UWB-based WSN planning," *IEEE Sensors Journal*, vol. 15, no. 10, pp. 5988–5996, 2015.
- [98] M. Govoni, F. Guidi, E. M. Vitucci, V. Degli Esposti, G. Tartarini, and D. Dardari, "Ultra-wide bandwidth systems for the surveillance of railway crossing areas," *IEEE Communications Magazine*, vol. 53, no. 10, pp. 117–123, 2015.
- [99] U. Demir, C. U. Bas, and S. C. Ergen, "Engine compartment UWB channel model for intravehicular wireless sensor networks," *IEEE Transactions on Vehicular Technology*, vol. 63, no. 6, pp. 2497–2505, 2014.

- [100] R. Chávez-Santiago and I. Balasingham, “Ultrawideband signals in medicine [life sciences],” *IEEE Signal Processing Magazine*, vol. 31, no. 6, pp. 130–136, 2014.
- [101] M. S. Mohammadi, Q. Zhang, E. Dutkiewicz, and X. Huang, “Optimal frame length to maximize energy efficiency in IEEE 802.15.6 UWB body area networks,” *IEEE Wireless Communications Letters*, vol. 3, no. 4, pp. 397–400, 2014.
- [102] K. Witrissal, S. Hinteregger, J. Kulmer, E. Leitinger, and P. Meissner, “High-accuracy positioning for indoor applications: RFID, UWB, 5G, and beyond,” in *IEEE International Conference on RFID*, 2016, pp. 1–7.
- [103] J. J. Rodrigues, S. Misra, H. Wang, and Z. Zhu, “Ambient assisted living communications [guest editorial],” *IEEE Communications Magazine*, vol. 53, no. 1, pp. 24–25, 2015.
- [104] J. Mao, Q. Zhou, J. Chen, P. Wang, F. Jonsson, L. Xu, L. Zheng, Z. Zou *et al.*, “A hybrid reader transceiver design for industrial internet of things,” *Elsevier Journal of Industrial Information Integration*, vol. 2, pp. 19–29, 2016.
- [105] Z. Zou, D. S. Mendoza, P. Wang, Q. Zhou, J. Mao, F. Jonsson, H. Tenhunen, and L.-R. Zheng, “A low-power and flexible energy detection IR-UWB receiver for RFID and wireless sensor networks,” *IEEE Transactions on Circuits and Systems I: Regular Papers*, vol. 58, no. 7, pp. 1470–1482, 2011.
- [106] T. Y. Wang, “Adaptive UWB pulse allocation for distributed detection in sensor networks,” *IEEE Transactions on Communications*, vol. 59, no. 5, pp. 1357–1367, 2011.
- [107] A. Vizziello and P. Savazzi, “Efficient RFID tag identification exploiting hybrid UHF-UWB tags and compressive sensing,” *IEEE Sensors Journal*, vol. 16, no. 12, pp. 4932–4939, 2016.

- [108] F. Jiang, J. Chen, A. L. Swindlehurst, and J. A. López-Salcedo, “Massive MIMO for wireless sensing with a coherent multiple access channel,” *IEEE Transactions on Signal Processing*, vol. 63, no. 12, pp. 3005–3017, 2015.
- [109] D. Ciuonzo, G. Romano, and P. S. Rossi, “Channel-aware decision fusion in distributed MIMO wireless sensor networks: Decode-and-fuse vs. decode-then-fuse,” *IEEE Transactions on Wireless Communications*, vol. 11, no. 8, pp. 2976–2985, 2012.
- [110] Y. Sabucu and S. Erköçük, “Noncoherent ultra wideband wireless sensor networks for primary user detection,” in *IEEE International Conference on Ultra Modern Telecommunications and Control Systems and Workshops (ICUMT)*, 2016, pp. 75–79.
- [111] K. Bai and C. Tepedelenlioglu, “Distributed detection in UWB wireless sensor networks,” *IEEE Transactions on Signal Processing*, vol. 58, no. 2, pp. 804–813, 2010.
- [112] G. Shirazi and L. Lampe, “Lifetime maximization in UWB sensor networks for event detection,” *IEEE Transactions on Signal Processing*, vol. 59, no. 9, pp. 4411–4423, 2011.
- [113] M. Cheffena, “Propagation channel characteristics of industrial wireless sensor networks [wireless corner],” *IEEE Antennas and Propagation Magazine*, vol. 58, no. 1, pp. 66–73, 2016.
- [114] F. Guidi, A. Guerra, D. Dardari, A. Clemente, and R. D’Errico, “Joint energy detection and massive array design for localization and mapping,” *IEEE Transactions on Wireless Communications*, vol. 16, no. 3, pp. 1359–1371, 2017.

List of publications

Journals:

1. S. Sharma, A. Gupta and V. Bhatia, "Compressed Sensing based UWB Receiver using Signal-Matched Sparse Measurement Matrix," *IEEE Transactions on Vehicular Technology*, (accepted).
2. S. Sharma, V. Bhatia and A. Gupta, "Joint Symbol and ToA Estimation for Iterative Transmitted Reference Pulse Cluster UWB System," *IEEE Systems Journal*, (accepted).
3. S. Sharma, V. Bhatia and A. K. Mishra, "Effects of Impulsive RFI on Wireless Consumer Electronic Devices," *IEEE Consumer Electronics Magazine*, (accepted).
4. S. Sharma, A. Gupta and V. Bhatia, "IR-UWB Sensor Network using Massive MIMO Decision Fusion: Design and Performance Analysis," *IEEE Sensors Journal*, vol. 18, no.15, pp.6290-6302, 2018.
5. S. Sharma, A. Gupta and V. Bhatia, "Impulse Noise Mitigation in IR-UWB Communication using Signal Cluster Sparsity," *IEEE Communications Letters*, vol. 22, no. 3, pp. 558-561, 2017.
6. S. Sharma, V. Bhatia and A. Gupta, "Noncoherent IR-UWB Receiver using Massive Antenna Arrays for Wireless Sensor Networks," *IEEE Sensors Letters*, vol. 2, no. 1, pp. 1-4, 2018.
7. S. Sharma, V. Bhatia and A. Gupta, "Sparsity-based narrowband interference mitigation in ultra-wideband communication for 5G and beyond," *Elsevier Computers and Electrical Engineering*, vol. 64, pp. 83-95, 2017.

8. S. Sharma and V. Bhatia, "UWB pulse design using constraint convex sets method," *Wiley International Journal of Communication Systems*, vol. 30, no. 14 pp. 1-14, 2017.
9. S. Sharma, A. Gupta and V. Bhatia "A new sparse signal-matched measurement matrix for compressive sensing in UWB communication," *IEEE Access*, vol. 4, pp. 5327-5342, 2016.

Conferences:

1. S. Sharma, V. Bhatia and A. Gupta, "An Iterative Transmitted Reference UWB Receiver for Joint ToA and Data Symbols Estimation," in Proc. IEEE international Conference on Communications ICC, Kansas City, MO, USA, May 2018.
2. S. Sharma, A. Bishnu, A. Gupta and V. Bhatia "Improved Noncoherent Receiver for Joint Range and Symbol Estimation," in Proc. *IEEE International Conference on Signal Processing and Communications (SPCOM)*, Indian Institute of Science (IISc) Bangalore, Jul. 2018.
3. S. Sharma, A. Gupta and V. Bhatia, "Joint estimation of ToA and data symbols in UWB communication in presence of impulsive interference," in Proc. *IEEE Global Communications Conference (GLOBECOM)*, pp. 1-7, Singapore, Dec. 2017.
4. S. Sharma, A. Gupta and V. Bhatia, "A simple modified peak detection based UWB receiver for WSN and IoT applications," in Proc. *IEEE 85th Vehicular Technology Conference (VTC Spring)*, Sydney, Australia, Jun. 2017.
5. S. Sharma, V. Bhatia and A. Gupta, "A non-coherent UWB receiver using signal cluster sparsity," in Proc. *IEEE Twenty-third National Conference on Communications (NCC)*, pp. 1-6, IIT Madras, India, Mar. 2017.
6. S. Sharma and V. Bhatia, "Performance analysis of filtered PSM signal using non-matched receiver for UWB communication," in Proc. *IEEE International*

Conference on Advanced Networks and Telecommunications Systems (ANTS), pp. 1-6, IISc Bangalore, India, Nov. 2016.

7. S. Sharma, A. Gupta and V. Bhatia, "Sparsity based UWB receiver design in additive impulse noise channels," in *Proc. IEEE 17th International Workshop on Signal Processing Advances in Wireless Communications (SPAWC)*, pp. 1-5, Edinburgh, UK, Jul. 2016.

Publications apart from thesis

Journal papers:

1. N. Kumar, S. Sharma and V. Bhatia, "Performance analysis of OFDM-based nonlinear AF multiple-relay systems," *IEEE Wireless Communications Letters*, vol. 6. no. 1, pp. 122-125, 2016.

Conference papers:

1. S. Sharma, K. Deka, V. Bhatia and A. Gupta, "SCMA codebook based on optimization of mutual information and shaping gain," in *Proc. IEEE GLOBECOM*, Abu Dhabi, UAE, Dec. 2018 (accepted).
2. M. Thakur, S. Sharma and V. Bhatia, "Noncoherent detection for dynamic transmitter and receiver in molecular communication," in *Proc. IEEE International Conference on Advanced Networks and Telecommunications Systems (ANTS)*, IIT Indore, India, Dec. 2018 (accepted).